GALACTIC AND EXTRAGALACTIC ASTRONOMY IN THE AGE OF LARGE SKY SURVEYS

Xinlun Cheng

Beijing, China

Master of Science in Data Science, University of Virginia, 2022

A Dissertation submitted to the Graduate Faculty
of the University of Virginia in Candidacy for the Degree of
Doctor of Philosophy

Department of Astronomy

University of Virginia
May 2024

Steven R. Majewski, Chair
Mark Whittle
Phil Arras
David Nichols

Galactic and Extragalactic Astronomy in the Age of Large Sky Surveys

Xinlun Cheng

(ABSTRACT)

Large-scale sky surveys have been and are the backbone of many revolutionary discoveries in astronomy and astrophysics. With huge strides in computer science and statistics, sky surveys are generating ever increasing amounts of data, posing both opportunities and challenges to astronomers in terms of proposing new astrophysical models to explain observed phenomena and machine learning models for data analysis and data mining. In this thesis, I will cover several such areas of progress used in my research. I will first present a characterization of the Galactic warp using the phase space and chemical information contained within millions of stars provided by Gaia and APOGEE, and our physics modeling attempt is the first to discover precession of the warp through stellar kinematics. Next we examine previously adopted assumptions in describing the density and velocity dispersion profile of the Galactic disk against a database formed by combining Gaia and APOGEE database, and we conclude that the traditional analytical methods of interpreting and modeling the stellar kinematics within such data sets are no longer adequate. A similar chemodynamical exploration can be applied to nearby galaxies — including dwarf galaxies — and we do so in the case of the Large Magellanic Cloud (LMC). Here we discover the existence of a kinematically and chemically distinct population of stars at the southern edge of the LMC. The discovered population has patterns consistent with an origin deriving from an interaction between the LMC, the Small Magellanic Cloud,

and the Milky Way. Lastly, we present a novel deep learning technique, contrastive self-supervised learning, applied to mitigate the lack of annotated training set in many astrophysically interesting problems. The pre-trained deep learning model exhibits a strong zero-shot learning capability and has great accuracy after fine-tuning when applied to the problem of searching for white dwarf - main sequence binaries within a large survey database of optical stellar spectra. The research areas covered in this dissertation serve as demonstrations of recent progress gained by the application of new approaches applied to large-scale astronomical survey data.

Acknowledgments

XC acknowledges support from the Jefferson Scholars Foundation in the form of a Jefferson Fellowship, as well as in providing office space and in hosting the dissertation defense. XC also acknowledges the financial support from School of Data Science during the pursuit of the Master of Science in Data Science degree from 2021 to 2022. XC appreciates the internship opportunity at Trexquant Investment LP, which provided invaluable hands-on experience in the analysis of noisy real world data, an experience crucial to the completion of the last chapter of this thesis. XC, SRM and others appreciate the National Science Foundation (NSF) for funding research presented in this thesis and the associated published papers. XC appreciates the guidance from his advisor Professor Steven R. Majewski, the postdoctoral researcher in the research group Dr Borja Anguiano, other members of the thesis committee, and the Department of Astronomy generally, on astronomical research, proposal, publication and thesis writing, and on being a scientist. XC also thanks all collaborators in previous research for their contribution to the projects that are presented in this thesis.

Contents

List of Figures

List of Tables

List of Abbreviations

AI Artificial Intelligence

APOGEE Apache Point Observatory Galactic Evolution Experiment

BHM Black Hole Mapper

CNN Convolutional Neural Network

Gyr Gigayear (3.156×10^{16} s)

kpc kiloparsec (3.086×10^{19} m)

LMC The Large Magellanic Cloud

$M_\odot$ The mass of the Sun (1.989×10^{30} kg)

ML machine learning

MW The Milky Way Galaxy

MWM Milky Way Mapper

SDSS Sloan Digital Sky Survey

SMC The Small Magellanic Cloud

SSL self-supervised learning

Chapter 1

Introduction

1.1 Astronomy and Sky Surveys

Ever since the beginning of their field of study, astronomers have relied on large-scale sky surveys, targeting either a large number of a pre-selected type of celestial object of interest (e.g., stars, galaxies, etc.), or all objects down to a certain brightness level. In modern surveys, the observed results are then usually processed through a dedicated data processing pipeline and typically released publicly after a period of proprietary access. Because astronomers cannot run laboratory experiments under controlled conditions, a practice common in many fields of natural science, to probe many astrophysically interesting problems, an alternative approach must be adopted. One is to gather as much data as possible from the universe to maximize the coverage of parameter space related to a specific problem or class of target and then apply statistical and modeling techniques to ascertain the astrophysical processes behind the observed phenomenon.

With recent advances in computing power, data mining in sky surveys is getting more popular and much progress in astronomy wouldn't have been possible without extensive data mining of large databases from these sky surveys. For example, many supernovae were discovered through sky survey programs, such as the All Sky Automated Survey for SuperNovae (ASAS-SN, Kochanek et al. 2017), and the re-

sults of these programs have revolutionized our understanding of cosmology. Gravitational wave detection also relies heavily on continuous monitoring of the sky for signals and fast follow-up observations from other telescopes and observatories for multi-messenger astronomy. Exoplanet detection through transit searching also requires the monitoring of thousands of stars through programs such as was done by NASA's Kepler mission (Borucki et al. 2010), the Transiting Exoplanet Survey Satellite (TESS, Ricker et al. 2015) and the CoROT Mission (Auvergne et al. 2009). The various generations of the Sloan Digital Sky Survey (SDSS, York et al. 2000), each composed of multiple dedicated sky surveys, such as the Baryon Oscillation Spectroscopic Survey (BOSS, Dawson et al. 2013) and the Apache Point Observatory Galactic Evolution Experiment (APOGEE, Majewski et al. 2017), have enabled great strides in the understanding of stellar populations, galaxy formation and evolution, large scale structure, and our own Milky Way galaxy. The large amount of data available enables the proposing and testing of astrophysical models of increasing complexity with the elevated statistical power.

1.2 Bigger Data, Better Astronomy: The History, Present, and Future of Chemo-dynamical Studies in Galactic Astronomy

In Galactic astronomy, it has always been beneficial to combine stellar kinematical/dynamical properties with chemical abundance information to perform what is known as a chemo-dynamical study, with chemical abundances often serving as a proxy for stellar population ages. Reviews of the field (e.g., Majewski 1993; Freeman

and Bland-Hawthorn 2002) typically attribute the first attempt at a systematic and comprehensive (in terms of spanning multiple stellar populations) chemo-dynamical study to Eggen et al. (1962), who found correlations between stellar metallicity and derived kinematical properties such as orbital eccentricity and maximum distance a star attains from the Galactic plane in a sample of 221 stars; from these sweeping correlations Eggen et al. hypothesized that various stellar populations of the Galaxy (namely the halo followed by the disk) formed during the collapse and spin-up of a protogalactic cloud during which time star formation and chemical enrichment proceeded. It was later realized that the Eggen et al. catalogue was significantly affected by survey bias, as explained at length by Mihalas and Binney (1981). Subsequent chemo-dynamical studies of globular clusters (Searle and Zinn 1978) and field halo stars (e.g., Marquez and Schuster 1994) challenged this proposed model of formation. Instead an alternative "bottom up" model, where the Milky Way galaxy formed via hierarchical aggregation of smaller elements and dynamically coherent debris of such events can still be found in the stellar halo today as tidal streams, was proposed and is now accepted as the consensus as multiple stellar streams were discovered around both the Milky Way (e.g., Majewski et al. 2003) and other galaxies (e.g., Tyson et al. 1998; Calcáneo-Roldán et al. 2000).

Despite these advances in arriving at the modern, more accepted model of galaxy formation, parallaxes and proper motions of distant stars are difficult to measure accurately using the primitive technology that was available in the 1970s and 80s, which severely limited the amount of high quality stellar kinematical data available. On the other hand, the increased volume of sky imaging data available allowed for improved star count studies, which can be done solely with reasonable quality photometric data. For example, Gilmore and Reid (1983) confirmed the existence of the previ-

ously proposed but somewhat elusive "Intermediate Population II" by performing a star count study in a dataset of about 12,500 stars at the Southern Galactic Pole, and for this "thick disk" measured a vertical scale height of about 1350 pc. After the year 2000, with the improvement in CCD and multi-band photometry, the estimation of metallicities and parallaxes from photometry improved dramatically in quantity and quality (e.g., Ivezić et al. 2012). In an early CCD-based starcount study, Siegel et al. (2002), using a database of 130,000 stars, concluded that the thin disk has a scaleheight of 290-350 pc while the thick disk has a scaleheight of 700-1200 pc. Only 6 years later, Jurić et al. (2008), using almost 46 million stars from SDSS, pinpointed the thin disk scale height to 300 pc and that of the thick disk to 900 pc — consensus values still adopted in the Galactic astronomy community today.

Apart from improvements in photometry, huge improvments in astrometry and spectroscopy were also enabled by technological progress. High resolution stellar spectra gives Galactic astronomers access to accurate measurements of radial velocity. Combined with more accurate measurement of parallax and proper motion through space-based astrometry satellites — Hipparcos (Perryman et al. 1997) and much later Gaia (Gaia Collaboration et al. 2016a) — full 6-D phase space investigations of large parts of the Milky Way are finally a reality, enabling evermore detailed investigations of the dynamics of individual stellar populations. For example, investigations of the thin disk velocity dispersion profiles by Norris and Ryan (1989) and Edvardsson et al. (1993) yielded relatively low velocity dispersions consistent with theoretical predictions (Cuddeford and Amendt 1992) favored at the time. However, such attempts for the thick disk would not be accomplished with reasonable accuracy until Pasetto et al. (2012a) using RAdial Velocity Experiment (RAVE) data. The result revealed that the thick disk population can be adequately described by an isothermal popu-

lation, but similar investigations into the thin disk are very limited radially (Pasetto et al. 2012b; Piffl et al. 2014; Sanders and Binney 2015). Self-consistent dynamical modelling of the Galaxy with the Jeans and Poisson equations were attempted in Bienayme et al. (1987), but this attempt was very limited in survey volume, even though the result was not far from modern day consensus prescriptions. Meanwhile, Binney (2012a) argued that action-angle phase space would prove to be more useful in dynamical modelling than the position-velocity phase space. Many subsequent studies have followed this approach (e.g., Binney 2012b; Piffl et al. 2014), but with recent advancements in numerical simulations, many studies are also shifting to comparison with mock catalogues generated from galaxy or cosmological scale hydrodynamical simulations, such as the Auriga Gaia mock catalogue (Grand et al. 2018). As another example, the FIRE-2 catalogue has been used to investigate the evolution of stellar streams (Panithanpaisal and Sanderson 2023).

Progress in technology also allows for high resolution stellar spectra to be acquired *en masse*. While the existence of different stellar populations has been known for decades, spatial, metallicity, and kinematics overlap of stellar populations made it difficult to separate them using only one of thee criteria. Pioneering work that showed that one can use multi-elemental chemistry featuring α/Fe ratios to distinguish the thin and thick disk stars started to appear around the year 2000. Fuhrmann (1998) established difference patterns in [Mg/Fe]-[Fe/H] space for thin and thick disk stars with a total of around 50 stars having high resolution stellar spectra, while Bensby et al. (2003) pointed out a similar distinction in [O/Fe]-[Fe/H] space with around 70 stellar spectra. Reddy et al. (2006) analyzed 22 elements of around 130 stars with high resolution spectra and found that different elements might give completely different trends, with α-elements showing enhancement in thick disk stars while other

elements show enhancement in Fe or no enhancement at all. More recently, with APOGEE surveying hundreds of thousands of red giant stars, even more distinct chemical signatures of the thick disk have been discovered. Masseron and Gilmore (2015) revealed adding [C/N] onto the commonly used [α/Fe]-[Fe/H] chemical space gives better separation of the thin and thick disk, and Hawkins et al. (2015) argued for more elements to be included in the separation criteria for even better accuracy.

In recent years, chemical studies of the thin and thick disk have been extended beyond the confines of the solar neighborhood (e.g., Hayden et al. 2014; Hayden et al. 2015; Hayden et al. 2020). Spatial variations in the well-known metallicity-age relation were discovered in Feuillet et al. (2019), and various mono-abundance population studies (e.g., Lian et al. 2022; Eilers et al. 2022), where the sample is further refined into smaller sub-populations in chemical spaces, have started to explore sub-population density profiles and kinematics. The combination of datasets has also extended beyond the practice of simply joining large databases of kinematics and chemistry. For example, the APOKASC (Pinsonneault et al. 2014; Pinsonneault et al. 2018) and later APO-K2 catalogue (Schonhut-Stasik et al. 2024), assembled from the spectroscopic observations of APOGEE and the asteroseismology data from the *Kepler* and K2 missions, consist of highly accurate measurements of stellar kinematics, chemistry, mass, radius, and age.

1.3 Bigger Data, Better Mining: The Rise of Machine Learning in Astronomy and its Associated Challenges

The increased volume of data also facilitates the discovery of rare objects. Recent progress in machine learning and artificial intelligence has enabled the incorporation of such methods directly in data processing pipelines and the toolboxes of individual researchers. With the large amount of data available, astronomers have started to apply machine learning techniques to astronomical data mining, making the previously laborious tasks of searching for "needle in the hay stack" sources fully automated, achieving a speed and scope that cannot be matched by humans. Automated machine learning pipelines incorporated in data processing steps of sky surveys have been proven successful in the search for supernovae by quickly identifying potential candidates in near-real time (Masci et al. 2019), searching for strong and weak gravitational lensing by image analysis (Jacobs et al. 2017; Abbott et al. 2018), and helping provide constraints on galactic dynamics through the discovery of stellar streams (Shih et al. 2022). Neural networks are seeing increasing adoption and application in astronomy, given their versatility, the existence of well-established Python frameworks for coding them, and the proliferation of high performance computing hardware in recent years. For example, ESA's Gaia mission (Gaia Collaboration et al. 2016a) uses an artificial neural network to estimate stellar parameters and chemical abundances from the combined Radial Velocity Spectrometer (RVS) spectra, forming the backbone of the General Stellar Parametrizer from spectroscopy (GSP-spec, Recio-Blanco et al. 2023) pipeline.

Nevertheless, a few issues have been identified in the application of machine learning in astronomy. Physics models with analytical solutions are rare and often too simplified to deal with many statistically significant fine patterns and structures in the observed data. While complex machine learning systems are versatile, they are often brittle and display a lack of ability to generalize. Extrapolation outside the training set coverage and/or low signal-to-noise regime is sometimes more than enough to produce unusable results from a machine learning model even though high accuracy was observed within the testing set. The training of complex machine learning systems often requires a large annotated training set. While sky surveys can produce a lot of data, finding enough objects of interest to assemble a training set can still be a very hard task to accomplish, either requiring significant computing time or nearly impossible to automate at all. Citizen science programs, such as Galaxy Zoo 2 (Willett et al. 2013) and Gravity Spy (Zevin et al. 2017), have been employed in the past to mitigate this problem, but such programs require the development of dedicated graphical interfaces and back-end systems to present data and record responses, can result in biases if the participants are not properly trained, and often require collaboration with commercial companies (the most famous example being EVE Online Project Discovery, Sullivan et al. 2018) to guarantee a large enough audience to reduce individual biases and finish the task in a reasonable amount of time.

1.4 Summary of Dissertation

In this thesis, I will be presenting several discoveries enabled by the increased amount of data provided by the sky surveys Gaia and APOGEE in the context of Galactic and extra-galactic astronomy. In Chapter 2, I will present a characterization of the

Galactic warp using the phase space and chemical information of millions of stars provided by Gaia and APOGEE, and our physics modeling attempts that included previously ignored radial velocity terms. In Chapter 3, I will illustrate the failure of the traditional Jeans equation approaches to described the surface mass density of the Milky Way disk and argue for more complex modeling and comparison methods to understand the Milky Way Galaxy, especially for stellar populations and dark matter near the disk. In Chapter 4, I will present the discovery of a kinematically distinct population in the Large Magellanic Cloud and some insights gathered from the thousands of stars in the LMC/SMC region from Gaia. We proposed one likely cause of this particular kinematics pattern is warping of the LMC disk due to interaction with SMC and/or MW. Lastly in Chapter 5, I will present a novel approach to training complex deep learning systems without an extensive annotated training set, how to preserve generalization of the deep learning model to even extrapolate on never-before-seen data, and the application of this approach on the search for white dwarf-M dwarf binary systems with stellar spectra.

Chapter 2

Exploring the Galactic Warp Through Asymmetries in the Kinematics of the Galactic Disk

This chapter was originally published as Cheng et al. (2020).

2.1 Introduction

Disk warps are common features of spiral galaxies (Bosma 1978; Binney 1992), and the presence of a warp in the outer Milky Way disk has been long-established, as seen in its H I (e.g., Kerr 1957; Westerhout 1957; Weaver 1974; Levine et al. 2006; Voskes and Butler Burton 2006), dust (Freudenreich et al. 1994), star-forming regions (Wouterloot et al. 1990) and stellar disk components (e.g., Amôres et al. 2017, and references therein). The ubiquity of warps suggests that they are either repeatedly regenerated or long-lived phenomena in the lives of galaxy disks (Sellwood 2013).

While the origin of the Galactic warp still invites controversy, the fact that the stellar warp follows the same topology as the gaseous one is evidence that the warp is gravitationally induced (e.g., Miyamoto et al. 1988; Drimmel et al. 2000). Interactions

with massive satellite galaxies can also affect the outskirts of galaxy disks, where the most likely candidates to create a warped outer disk in the Milky Way are the Sagittarius (Sgr) dwarf spheroidal (dSph) galaxy (Ibata and Razoumov 1998; Laporte et al. 2019), and the Magellanic Clouds (Weinberg and Blitz 2006; Garavito-Camargo et al. 2019). External torques on galaxy disks have also been identified with the accretion of intergalactic matter (Ostriker and Binney 1989; Wang et al. 2020), intergalactic magnetic fields (Battaner et al. 1990; Guijarro et al. 2010) and mis-aligned dark halos (Sparke and Casertano 1988; Widrow et al. 2014; Amôres et al. 2017). Moreover, disk instability has also been attributed to the cause of the warp. For instance, Chen et al. (2019) probed line-of-node twisting of the Galactic warp with classical Cepheids and suggested that the warp originated from the torques from the massive inner Galactic disk.

While the origin of the Galactic warp understandably remains a complex puzzle, simply defining the geometry of the warp is a problem that is also far from resolved, with a variety of potential models posited for its shape (Romero-Gómez et al. 2019). Even something as seemingly straightforward as the radius of the onset of the Galactic warp is still under debate. For example, Drimmel and Spergel (2001) found the onset of the warp to lie ~ 1 kpc *inside* the solar circle using a three-dimensional model for the Milky Way fitted to the far-infrared (FIR) and near-infrared (NIR) data from the COBE/DIRBE instrument, a result supported by Huang et al. (2018) using stars from TGAS-LAMOST. Schönrich and Dehnen (2018), using *Tycho-Gaia* Astrometric Solutions (TGAS) data set, also claimed that the warp begins inside the solar circle. On the other hand, population synthesis models from Derriere and Robin (2001) and Reylé et al. (2009) placed the onset of the Galactic warp at or outside the solar circle (see also Romero-Gómez et al. 2019, discussed further below).

In addition, the precession rate of Galactic warp is also unsettled. Drimmel et al. (2000) claimed that the warp is precessing rapidly (about 25 km s^{-1} kpc^{-1}) in the direction of Galactic rotation, though the authors also acknowledge that the biased photometric distance caused the observed vertical motion to be smaller than their true values, mimicking the signal of precession. On the other hand, Bobylev (2010) analyzed the three-dimensional kinematics of about 82,000 Tycho-2 stars belonging to the red giant clump (RGC), and claimed that no significant precession of the warp is detected in the solar neighborhood. Most recently, Poggio et al. (2020) applied the precessing warp model from Drimmel et al. (2000) to Gaia DR2 data with warp starting radius, height and shape (R_w, h_w and α) fixed to values in previous studies, and report that the warp is precessing at 10.46 km s^{-1} kpc^{-1}, i.e., roughly half the rate found by Drimmel et al. Yet still more complicated are the definition of warp parameter dependencies as a function of stellar ages, which may bear on the evolution of the warp or on the relative responses of different stellar populations to perturbations. For example, Amôres et al. (2017), using 2-Micron All Sky Survey (2MASS; Skrutskie et al. 2006) data and the Besançon Galaxy Model (Czekaj et al. 2014), identified a clear dependence of the thin disc scale length as well as the warp and flare shapes with age. Meanwhile, the recent availability of enormous samples of Milky Way stars with precise 3-D kinematics coming from the second data release of *Gaia* (*Gaia* DR2; Gaia Collaboration et al. 2018a) has enabled much more comprehensive analyses of Galaxy dynamics over large ranges of Galactocentric radius, with the added means to estimate ages for field stars, and with much greater statistical robustness for both. For instance, Poggio et al. (2018) using a combined sample of *Gaia* DR2 and 2MASS photometry found the presence of a warp signal in two stellar samples having different typical ages, and suggested that this means the warp is a gravitationally induced phenomenon. Shortly thereafter, Romero-Gómez

et al. (2019) used two populations of different ages — young (OB-type) stars and intermediate-old age (red giant branch, RGB) stars — selected from *Gaia* DR2 and reported different onset radii for the Galactic warp for each, namely 12-13 kpc for the young sample versus 10-11 kpc for the older sample. These authors also report that the older sample reveals a slightly lopsided warp, i.e., the warp is not symmetric in shape about the plane, with a possibly twisted line of nodes.

One of the significant outcomes of this new capability in Galactic astronomy is the mapping of stellar motions — and asymmetries in those motions — across the Milky Way disk (e.g., Kawata et al. 2018; Poggio et al. 2018; López-Corredoira et al. 2020). Such kinematical asymmetries would be expected in the presence of a warp, but they can also explain smaller-scale features. For example, Bennett and Bovy (2019) and Carrillo et al. (2019) each reported a combination of bending and breathing modes using stellar kinematics derived from *Gaia* astrometry, and confirmed that the Galactic disk is undergoing a wave-like oscillation with a dynamically perturbed local vertical structure within the solar neighborhood.

Such oscillatory motions may also explain various low latitude substructures that reside in the *outer* Galactic disk, like the Monoceros ring (Newberg et al. 2002), Triangulum-Andromeda (TriAnd) (Rocha-Pinto et al. 2004; Majewski et al. 2004), A13 (Sharma et al. 2010; Li et al. 2017) and other ring-like overdensities (Peñarrubia et al. 2005), whose origins have long been debated. For example, Monoceros and TriAnd were originally thought to be low-latitude tidal debris from dwarf galaxies (Chou et al. 2010; Sollima et al. 2011; Sheffield et al. 2014). However, there is now mounting chemical and kinematical evidence that some of these overdensities belong to the disk of the Milky Way (Bergemann et al. 2018; Hayes et al. 2018; Sales Silva et al. 2019) and represent concentrations of stars at the crests or troughs of ripple-like

density waves in the Galactic disk or vertical oscillations of the Milky Way midplane at large Galactocentric radii that are excited by orbiting dwarf galaxies (e.g., Kazantzidis et al. 2008; Newberg and Xu 2017; Laporte et al. 2018; Bland-Hawthorn et al. 2019). If these overdensities are related with the local vertical structure of the Milky Way disk, they may therefore provide further constraining power on the source of these perturbations.

In this study we use *Gaia* DR2 and APOGEE together with the StarHorse distance solutions (Anders et al. 2019) to explore vertical and radial velocity patterns and structures in the kinematics of the Galactic disk and to use these features to characterize the onset radius and precession rate of the warp. In Section 2.2, we describe the sources of our data, the distances adopted and conversion to the Galactocentric reference frame. In Section 2.3, we present several detected kinematical signatures in vertical and radial velocity, and in Section 2.4 we apply a simple model, based on the Jeans Equation, to characterize these findings. In Section 2.5, we compare the responses to the galactic warp in four different age populations. In Section 2.6, we present the main conclusions from our analysis and outline prospects for building on the present work.

2.2 Data

The data in this paper come primarily from *Gaia* DR2 (Gaia Collaboration et al. 2016a; Gaia Collaboration et al. 2018a) and the Apache Point Observatory Galactic Evolution Experiment (APOGEE & APOGEE-2, Majewski et al. 2017), part of SDSS-III (Eisenstein et al. 2011) and SDSS-IV (Blanton et al. 2017). We use these two primary sources to generate two different data-sets for our analysis of the Galactic

warp.

The first data-set uses information for the 7,224,631 stars down to $G \simeq 13$ for which *Gaia* DR2 provides full *6-dimensional* phase space coordinates: positions (α, δ), parallaxes (ϖ), proper motions ($\mu^*_\alpha = \mu_\alpha \cos\delta$, μ_δ), and radial line-of-sight velocities ($v_{\rm los}$) (Cropper et al. 2018). From that catalog, stars with suspect photometry and stars where the $v_{\rm los}$ measurement is based on fewer than four *Gaia* transits are removed. In addition, we decontaminate our sample of stars from the Large Magellanic Cloud (LMC) and Small Magellanic Cloud (SMC) by removing any sources within 5 degrees of the center of these systems.

Our second data-set is smaller, combining the proper motion, parallax and photometric information from *Gaia* DR2 with the chemical and radial velocity information from the latest public release of data from the APOGEE-2 survey, as contained in Sloan Digital Sky Survey (SDSS) Data Release 16 (DR16 Ahumada et al. 2020). DR16 contains high resolution spectroscopic observations from both the Northern and Southern Hemispheres taken with the twin APOGEE instruments (Wilson et al. 2019) on the Sloan 2.5-m (Gunn et al. 2006) and the du Pont 2.5-m (Bowen and Vaughan 1973) telescopes, respectively. Individual stellar atmospheric parameters and chemical abundances are derived from the APOGEE Stellar Parameter and Chemical Abundance Pipeline (ASPCAP, García Pérez et al. 2016). For SDSS DR16, ASPCAP has been updated to use a grid of MARCS stellar atmospheres and a *H*-band line list (Jönsson et al. 2020; Smith et al. 2021), all of which are are used to generate a grid of synthetic spectra against which are compared the target spectra to find the best match (e.g., Zamora et al. 2015). From the full APOGEE sample we require all sources to have the APOGEE `TARFLAG and \verb ACAPFLAG` set to "0" and to have an effective temperature between 3700K and 5500K. A further restriction

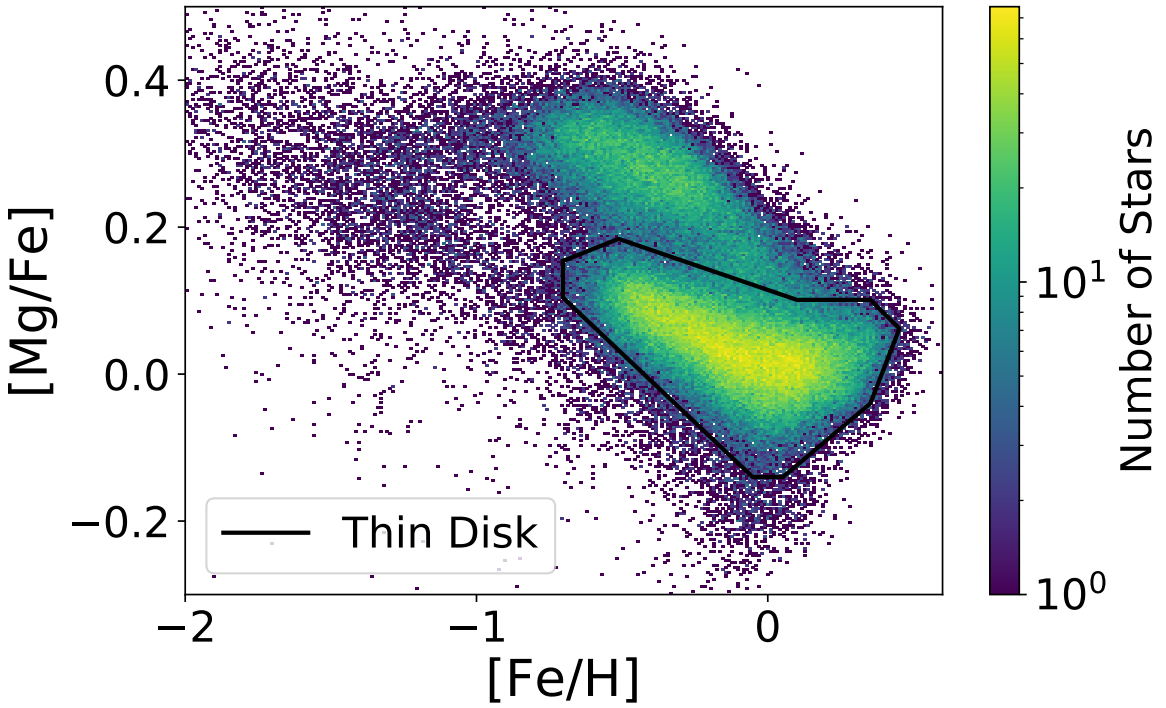

Figure 2.1: The [Mg/Fe]-[Fe/H] chemical plane from APOGEE DR16, from which we define our thin disk selection for our analysis. The colorbar represents the number of stars in each chemical bin (with yellow representing the highest density) and is on a logarithmic scale. Our thin disk selection is defined very conservatively by the solid line.

in [Fe/H] and [Mg/Fe] was made to only keep stars having chemistry characteristic of stars in the thin disk (see e.g. Bensby et al. 2014; Hayes et al. 2018), as illustrated and defined in Figure 2.1. The adopted thin disk selection criterion is defined very conservatively, to limit contamination by non-thin-disk stars.

In this study we use distances derived through Bayesian inference using the StarHorse code (Queiroz et al. 2018). StarHorse combines precise parallaxes and optical photometry delivered by *Gaia* DR2 with the photometric catalogues of Pan-STARRS1 (Chambers et al. 2016), 2MASS (Skrutskie et al. 2006), and AllWISE (Wright et al. 2010), aided by the use of informative Galactic priors (Santiago et al. 2016; Queiroz et al. 2018). For the APOGEE data-set we use the StarHorse distances and extinc-

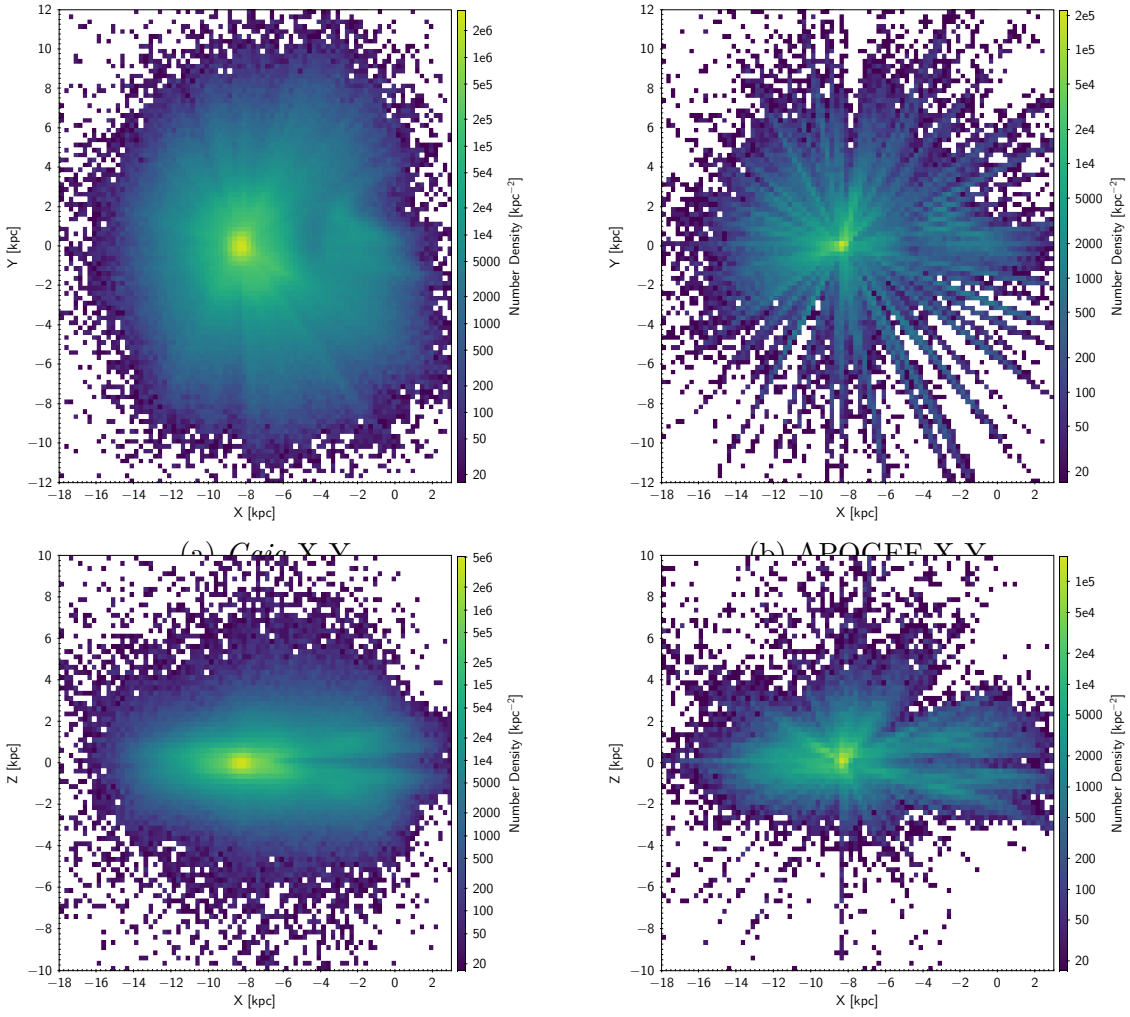

(c) *Gaia* X-Z (d) APOGEE X-Y

Figure 2.2: The spatial distributions of the *Gaia* (left) and *Gaia*-APOGEE (right) data-sets used in this paper, in Galactocentric coordinates. Each pixel represents 0.25×0.25 kpc^2. The top panel shows the X_{GC}-Y_{GC} projection onto the Galactic plane, while the lower panels show projections onto the X_{GC}-Z_{GC} plane. Similar plots are seen in Anders et al. (2019) and Queiroz et al. (2020).

tions from the APOGEE-2 DR16 StarHorse Value Added Catalog (Queiroz et al. 2020). The latter combines high-resolution spectroscopic data from APOGEE DR16 with the broad-band photometric data from the above sources and the *Gaia* DR2 parallaxes. Following the recommendation in Queiroz et al. (2020), we adopt the combination of `SH_GAIAFLAG=="000"` and `SH_OUTFLAG=="00000"` to filter out stars that have a problematic *Gaia* photometric or astrometric solution or a troublesome StarHorse data reduction.

The mean distance uncertainties for stars in our *Gaia* /*Gaia*-APOGEE samples is 0.24/0.42 kpc, and the mean relative uncertainties of distance are $\sim$ 8/10%. The mean uncertainty for the proper motions are 0.06/0.06 mas yr^{-1} for each the right ascension (RA) and declination (Dec) directions. Meanwhile, the mean uncertainties for the radial velocities are 1.69 km s^{-1} for those coming from *Gaia* , and 0.21 km s^{-1} for those from APOGEE. The total number of stars in the *Gaia* and *Gaia*–APOGEE data-sets are 5,460,265 and 179,571, respectively.

The Galactocentric coordinate system adopted in this paper is right-handed, with the Sun at $(X, Y, Z) = (-8.12, 0, 0.02)$ kpc (Gravity Collaboration et al. 2018a; Bennett and Bovy 2019), a Local Standard of Rest (LSR) velocity $V_{LSR} = 233.4$ km s^{-1} (Reid and Brunthaler 2004; Gravity Collaboration et al. 2018a), and a solar velocity relative to the LSR of $V_{\odot} = (12.9, 12.24, 7.78)$ km s^{-1} (Drimmel and Poggio 2018). Note that in this adopted Galactocentric Cartesian coordinate system, Galactic rotation converts to a negative azimuthal velocity (v_{ϕ}) when expressed in cylindrical coordinates. For this reason, in many of the figures presented below, we adopt $-L_z$ for the abscissa.

Under this coordinate system, the spatial distribution of stars in our samples is shown in Figure 2.2. As may be seen, both of our samples have kinematical information

extending to ∼10 kpc from the Sun, although most of the stars are concentrated in the disk, within $Z = \pm 3$ kpc of the Galactic plane. The presence of the Galactic bar and bulge starts becoming evident at $X \lesssim -4$ kpc. The presence of the Galactic bar and bulge starts becoming evident at $X < -4$ kpc in our data, as already reported by Anders et al. (2019) and Queiroz et al. (2020) using the StarHorse distance solution. As expected, the all-sky *Gaia* sample is more smoothly and completely distributed, while the *Gaia*-APOGEE sample shows the pencil-beam spikes corresponding to the field-by-field coverage of the APOGEE and APOGEE-2 surveys, as well as the more limited coverage in the Southern Hemisphere, where APOGEE only began observing more recently in APOGEE-2.

2.3 Kinematical Structures and Patterns

2.3.1 The General Trend and Ripples in Vertical Velocity

The warp and its kinematical signature are expected to be more prominent towards the Galactic anticenter and evident by large-scale systemic stellar motions perpendicular to the plane (e.g., Binney 1992; Drimmel et al. 2000). Our *Gaia* and *Gaia*–APOGEE samples, in combination with the StarHorse distances, allow us to characterize the stellar vertical motion over a large range of Galactocentric radius, where we are able to explore to $R_{GC} \sim 18$ kpc. Here we study the kinematical signature of the Galactic warp in our two stellar samples, specifically by exploring the vertical velocity v_z in the disk as a function of angular momentum (L_z) and Galactocentric radius (R), as was done previously by Schönrich and Dehnen (2018) and Huang et al. (2018). In addition, we look for any azimuthal asymmetries in these trends.

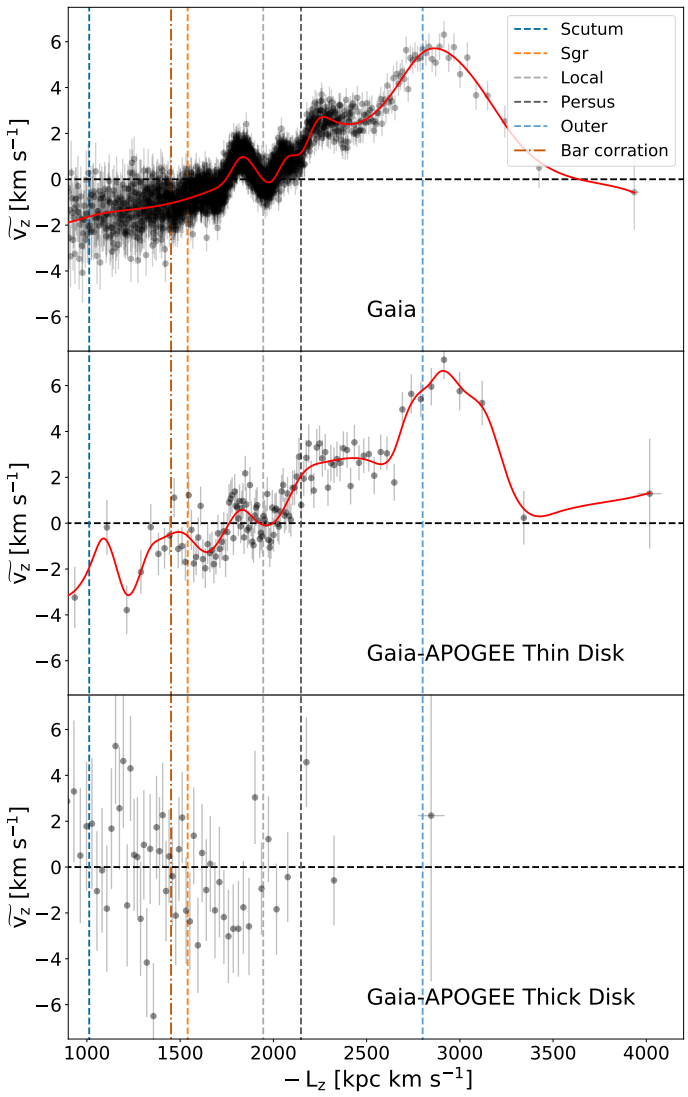

Figure 2.3: The vertical velocity ($\widetilde{V_z}$) versus angular momentum (L_z) for the *Gaia* (*top*) and *Gaia*-APOGEE thin disk (*middle*) and thick disk (*bottom*) samples. Stars are sequentially grouped into 2000-star bins for the *Gaia* sample, 1000-star bins for the *Gaia*-APOGEE thin disk sample, and 500-star bins for the *Gaia*-APOGEE thick disk sample (however, so that they would not be hindered by small sample size, the bins at largest L_z contain 2265 stars for the *Gaia* dataset, 1571 stars for the *Gaia*-APOGEE thin disk dataset and 526 stars for the thick disk dataset). Each data point represents the median angular momentum and median vertical velocity ($\widetilde{V_z}$) for stars in that bin. Error bars represent the uncertainty of the median values, estimated through bootstrapping (see text). The solid red lines are smoothed trends to help visualize the data better. The dashed vertical lines indicate the angular momentum of spiral arms — see discussion of the potential origin of the observed $\widetilde{V_z}$ ripples in Section 3.1.

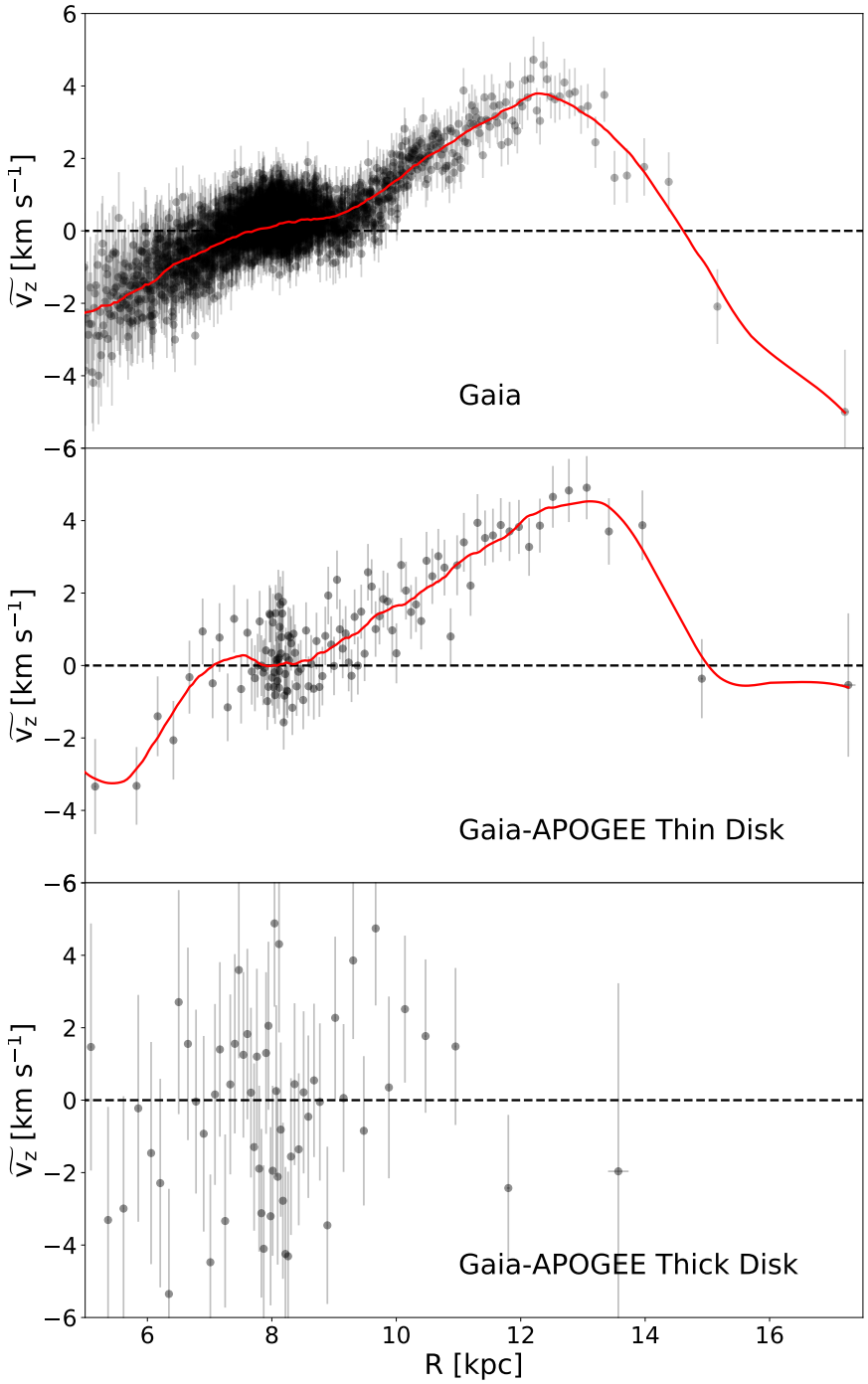

Figure 2.4: The same as in Figure 2.3, but now showing the vertical velocity (v_z) shown as a function of Galactocentric radius (R), with stars sorted and binned sequentially in R. As in Figure 2.3, the trend in the *Gaia* sample (*top panel*) is well-matched by the *Gaia*-APOGEE thin disk sample (*middle panel*), but not the thick disk sample (*bottom panel*).

Figure 2.3 shows the run of $\widetilde{v_z}$ with L_z, for the *Gaia* data-set (in the left panel), and the chemically selected thin disk stars from the *Gaia*–APOGEE sample (in the right panel). Stars in Figure 2.3 are sorted and binned by angular momentum, with each point representing 2000 stars for the former data-set, and because the parent sample is smaller, each point representing 1000 stars for the *Gaia*–APOGEE sample. The error bars represent the uncertainty of the median value, which have been estimated through bootstrapping: 1000 subsamples containing 80% of the stars in each bin were randomly drawn and the standard deviation of the median of these subsamples were taken as error of the median.

The trend of the *Gaia* sample (top panel of Figure 2.3) strongly resembles that of the *Gaia*-APOGEE sample (middle panel). Because the latter was deliberately chosen via chemistry (Figure 2.1) to select thin disk stars, we can conclude that the features shown in the larger *Gaia* sample are driven by thin disk stars. This conclusion is reinforced by the trend of the thick disk stars (bottom panel), which doesn't at all resemble the trend of the *Gaia* stars.

Figure 2.3 shows that over a large range of L_z the overall mean vertical velocity increases with L_z, starting at -2 km s^{-1} and peaking at around $+6$ km s^{-1}. This velocity increase is more pronounced for values larger than $L_z > 1800$ kpc km s^{-1} and continues until $L_z \sim 2800$ kpc km s^{-1}, after which $\widetilde{v_z}$ sharply declines. A general increasing trend of $\widetilde{v_z}$ with L_z was also noted by Schönrich and Dehnen (2018) and Huang et al. (2018). However, while these previous studies reported that the correlation between $\widetilde{v_z}$ and L_z can be approximated by a rising linear fit over their entire sample, our more extensive radial coverage of disk kinematics reveals that the increasing trend is limited to $L_z \lesssim 1800$ kpc km s^{-1}, beyond which $\widetilde{v_z}$ actually declines. *We believe that this entire global trend in $\widetilde{v_z}$ is the signature of the Galactic*

warp, and we further characterize it and model it as such in Section 2.4.

Figure 2.3 also reveals, superposed on top of this general trend, higher frequency, wave-like ripples in $\widetilde{v_z}$ as a function of L_z. The source of these $\widetilde{v_z}$ ripples is more elusive (and will be explored after examination of similar trends in radial velocity, discussed in Section 2.3.2). However, these ripples are less prominent in the vertical velocity versus Galactocentric radius plot (Figure 2.4): Although the general trend of vertical velocity first increasing and then decreasing as Galactocentric radius increases is still evident, the ripples, especially those at solar radius, are smeared out in this representation. We argue that the reason the ripples are present in Figure 2.3 but not Figure 2.4 is because angular momentum is conserved for stars but for a given present-day radius, you have a mix of stars at different phases in their orbits. Therefore, after stars have made a few revolutions around the Galactic center, any initial spatial patterns would smear out when binned in Galactocentric radius, even while L_z is preserved.

An asymmetry in the Galactic H I warp has been extensively studied (Burke 1957; Baldwin et al. 1980; Henderson et al. 1982; Richter and Sancisi 1994), but whether there is a similar effect on the stellar disk is less understood. Recently, Romero-Gómez et al. (2019) reported asymmetry in the mean vertical distance of the stars from the Galactic plane about the warp line of nodes at $\phi \approx 180°$, with the warp-down amplitude (at $\phi \gtrsim 180°$) being larger than the warp-up amplitude (at $\phi \lesssim 180°$), i.e., that the warp is lop-sided. Such differences in the amplitude of the spatial distribution may correlate to an asymmetry in the azimuthal variation of vertical velocity between the up and down sides of the warp. Furthermore, previous research also probed the possibility that the peak maximum vertical velocity is not in the anti-center direction (Yusifov 2004; Skowron et al. 2019; Li et al. 2020).

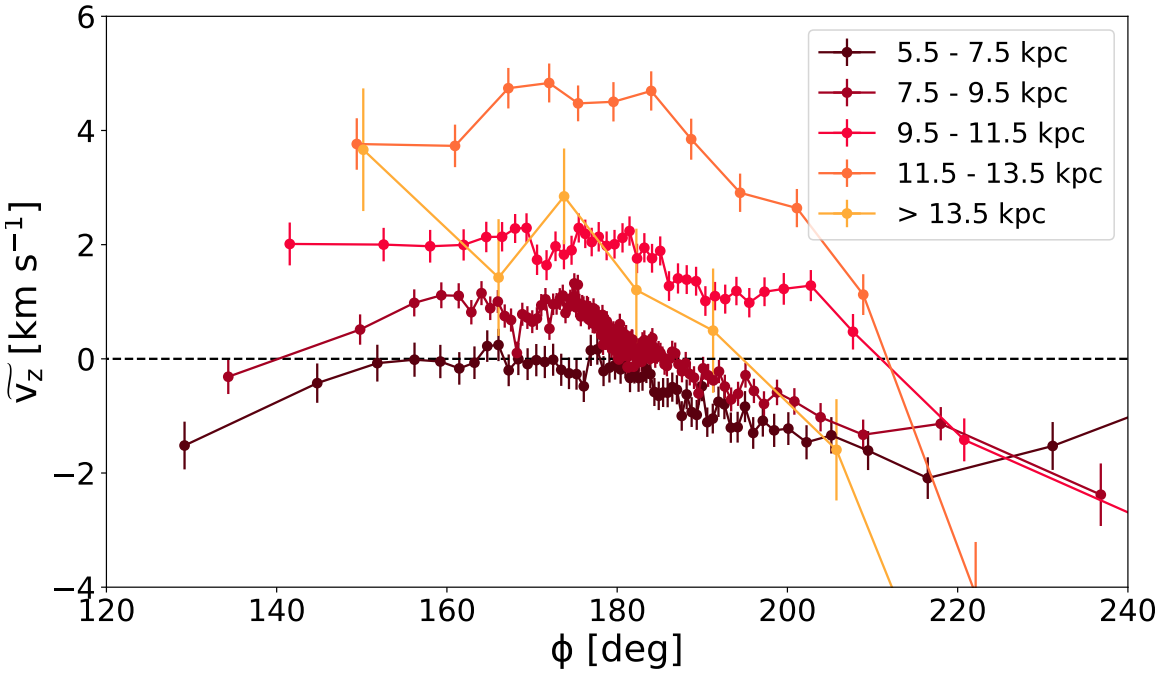

Figure 2.5: The vertical velocity versus Galactocentric azimuthal angle for the *Gaia* sample. The binning size is different for each radial bin: 20 000 stars/bin, 20 000 stars/bin, 10 000 stars/bin , 6000 stars/bin and 1500 stars/bin. The character of the trends for different radial annuli do not track one another; in particular, the rates of increase and decrease of $\widetilde{v_z}$ and the ϕ of maximum $\widetilde{v_z}$. These variations suggest that the warp may be lopsided.

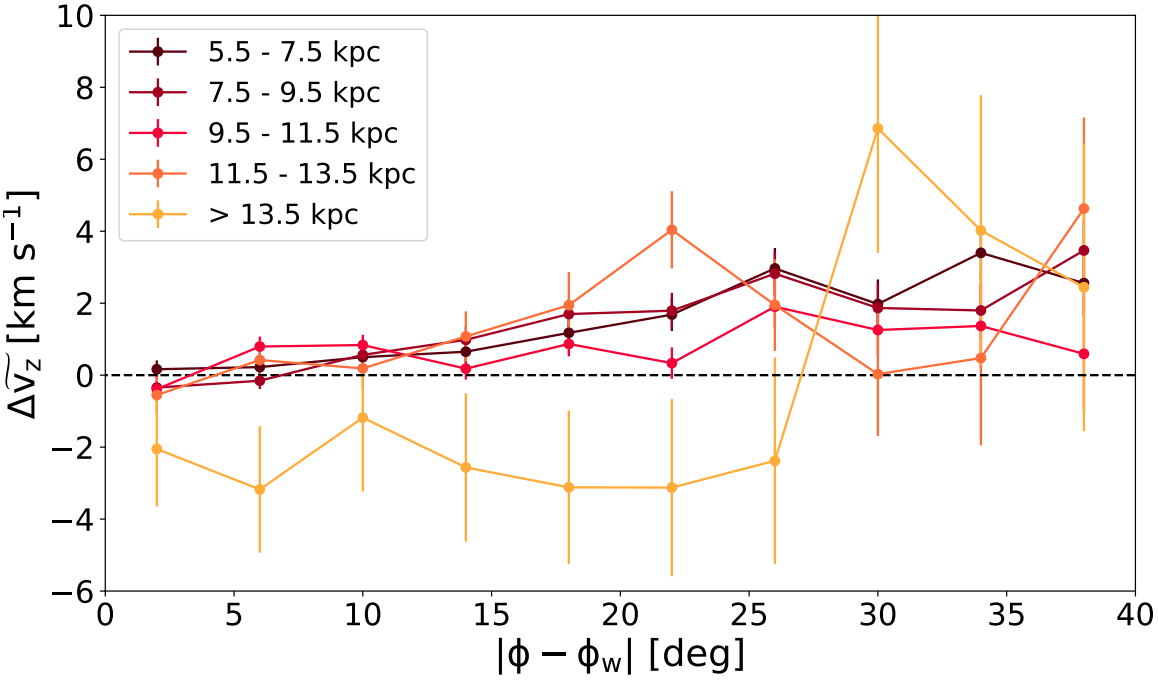

Figure 2.6: The vertical velocity differences between stars at $\phi < \phi_{peak}$ and $\phi > \phi_{peak}$ versus Galactocentric azimuthal angular separation from ϕ_{peak} for the *Gaia* sample. Stars are binned in 5° bins. ϕ_{peak} is determined through binning the stars with 10° bins and finding the bin with maximum vertical velocity.

To verify these presumptions, we plot the median vertical velocity as a function of Galactocentric azimuth angle, ϕ, for different radial annuli in Figure 2.5. At Galactocentric radii around the solar neighborhood, we see that the vertical velocity is relatively constant as a function of azimuthal angle; but at larger radii, we begin to see substantial differences in the vertical velocities at different azimuths. In particular, the vertical velocity first increases as ϕ increases, reaches a maximum vertical velocity peak or plateau around $\phi \approx 170°$, and then decreases with increasing ϕ. Furthermore, the increasing and decreasing slopes of the vertical velocity with ϕ appear to be asymmetric about this peak or plateau, with a steeper decline in vertical velocity at $\phi > 170°$ than the increase at $\phi < 170°$. For a warp with an equal warp-up and warp-down amplitude, the vertical velocity should be symmetric about the longitude of peak vertical velocity; that this is not seen further indicates that the warp is lop-sided, as previous studies have identified using the altitude with respect to the Galactic plane at a given Galactocentric radius (e.g., Marshall et al. 2006; Romero-Gómez et al. 2019).

To illustrate further the kinematical lopsidedness of the Galactic warp, we directly measure the velocity asymmetry by subtracting the median vertical velocity of stars on one side of ϕ_{peak} from its complement on the other side at the same azimuthal separation for each radial annulus (Figure 2.6), and ϕ_{peak} is estimated within each radial annulus by using a wider bin (10°) between $160 < \phi < 200°$.

2.3.2 Ripples in Radial Velocity and their Potential Origin

Figure 2.7 and Figure 2.8 show the complementary stellar radial motions with respect to L_z and R, respectively. Here, again, a pattern of ripples is seen, and they are even

more dramatic, reaching more extreme velocity amplitudes. As was observed with the v_z trends (i.e., Figure 2.3 and Figure 2.4) (a) the trends of the *Gaia* sample are best matched by the *Gaia*-APOGEE thin disk sample rather than the thick disk sample, and (b) the v_R ripples seen when plotted as a function of L_z are smeared out when plotted as a function of Galactocentric radius. Such a kinematical pattern for v_R was also reported for very young OB stars alone when viewed with respect to Galactocentric radius (Cheng et al. 2019).

Two possible mechanisms have previously been proposed to lead to such observed ripples. One explanation for these localized features is that they may be related to spiral arm perturbations, where the mass enhancements associated with spiral density waves can gravitationally scatter stars (e.g., Jenkins and Binney 1990). To illustrate the potential connection of these oscillations to spiral arms, in Figure 2.3 we indicate the angular momentum values of the known Milky Way spiral arms, calculated as follows: First we take the parameters that characterize these spiral arms from Reid et al. (2014). Then, a number of equally-spaced points were generated within the Galactocentric radius and azimuthal angle range of each spiral arm. The standard rotation curve from Bovy (2015) is assumed and used to calculate the azimuthal velocity. The angular momentum for each point is then computed and a variety of statistics (median, standard deviation, min/max values) generated to describe each spiral arm (see Table 2.1). We also show the L_z position corresponding to the Galactic bar, where we assume a pattern speed of $\Omega = 39.0$ km s^{-1} kpc^{-1} (Portail et al. 2017).

After performing this simple exercise, we find (Figure 2.3) that even though the nominal Perseus and Outer arms correspond to local maximum of the vertical ripples, the Scutum, Sgr and Local arms do not. In terms of radial motion (Figure 2.7), there are many v_R features that appear to be matched to corresponding v_z features at the

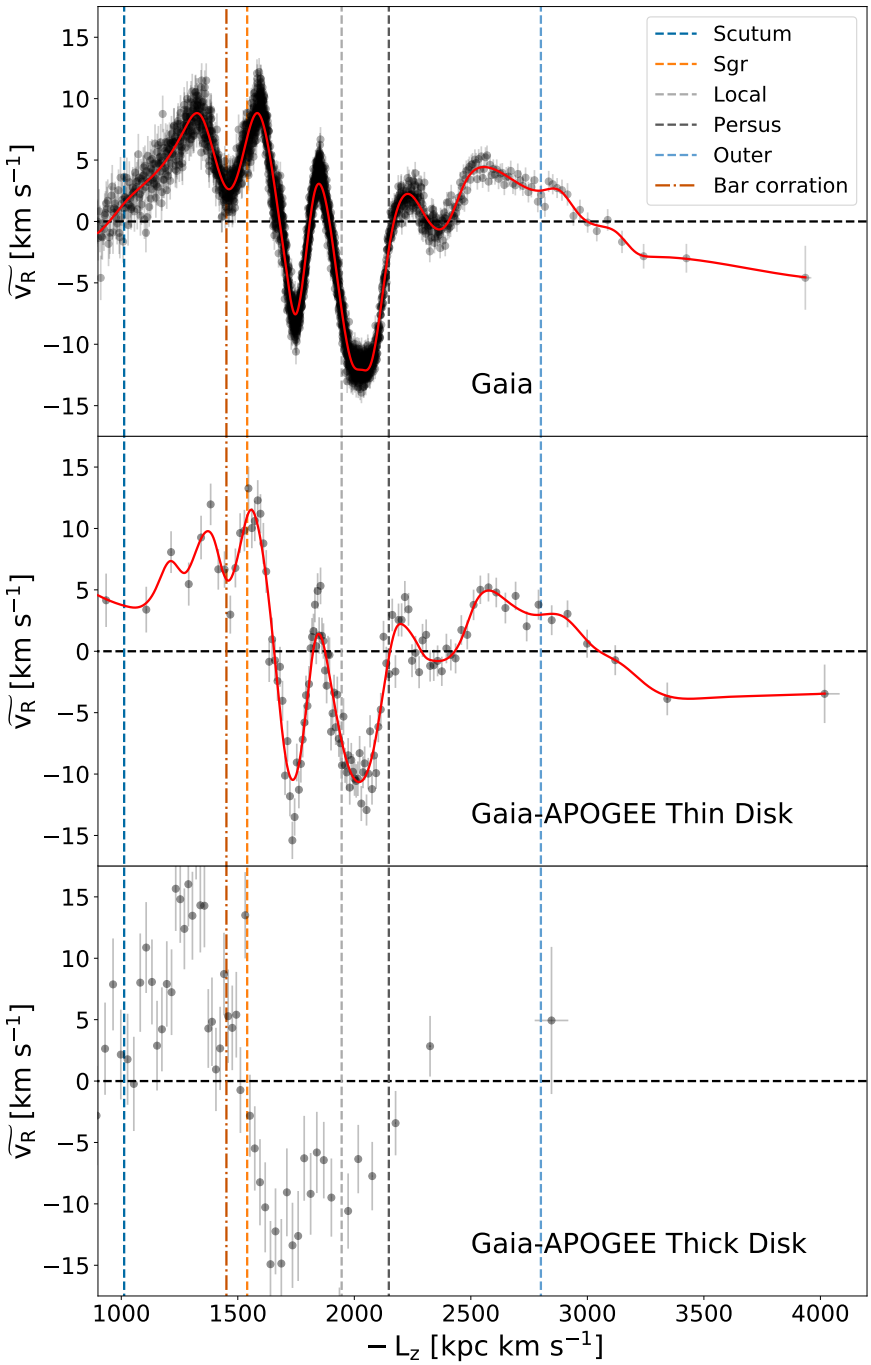

Figure 2.7: The same as in Figure 2.3, but now showing the radial velocity (v_R) versus angular momentum (L_z) for the *Gaia* (*top*), *Gaia*-APOGEE thin disk (*middle*), and *Gaia*-APOGEE thick disk (*bottom*) samples.

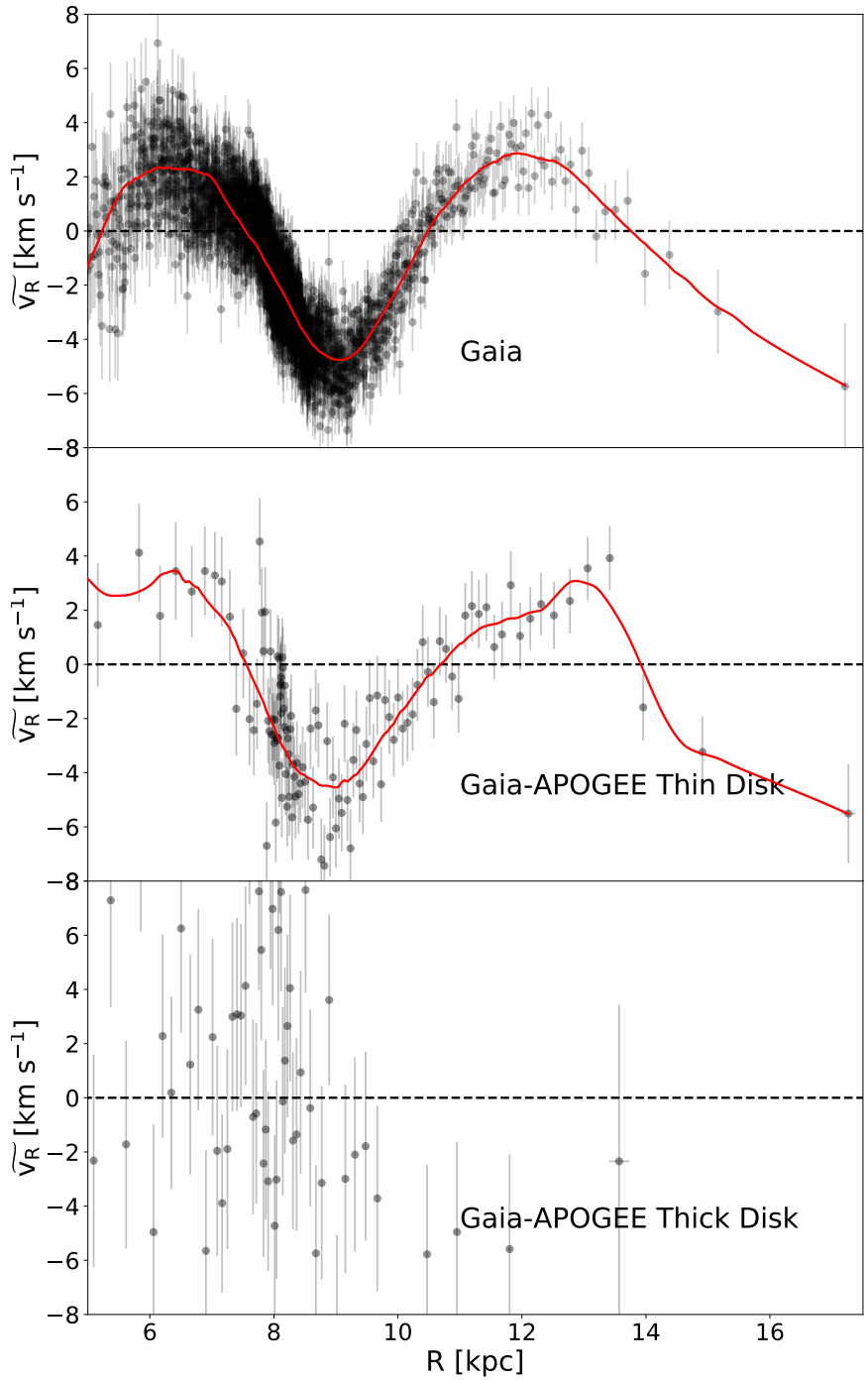

Figure 2.8: The same as in Figure 2.4, but now showing the radial velocity (v_R) versus Galactocentric radius (R).

Table 2.1: Summary of the vertical angular momentum properties for different known Milky Way spiral arms, calculated as described in Section 2.3.1. The second and third columns are the median angular momentum and corresponding standard deviation for each spiral arm.

Spiral arm	$\widetilde{L_z}$ (kpc km s^{-1})	σ_{L_z} (kpc km s^{-1})
Scutum	1012	202
Sagittarius	1540	85
Local	1945	98
Perseus	2148	191
Outer	2800	225

same L_z, and some correlations between the L_z positions of some ripples and those characteristic of spiral arms can be seen — in particular, once again, between the $L_z \sim 1950$ kpc km s^{-1} valley and the Local Spiral Arm and the peak at $L_z \sim 2150$ kpc km s^{-1} with the Perseus Spiral Arm, but in this case no correlation between the Outer Spiral Arm and a v_R feature is seen. We expect spiral arms to couple more tightly with the *radial* motions of stars, making the radial velocity dispersion significantly greater than the velocity dispersion perpendicular to the plane (e.g., Jenkins and Binney 1990; Aumer et al. 2016). However, while most spiral arms correspond to maximum positive velocity, the local arm is at the point of maximum negative velocity. It is also apparent that some ripples visible in these figures *do not* correlate with known spiral arm patterns, while some spiral arms (in particular, those at smaller L_z) *do not* match observed ripples. While these discrepancies might suggest that the ripples are not (or not entirely) generated by spiral arms, such lack of one-to-one correlation may also reflect shortcomings of the above illustrative exercise and the many uncertainties and simple assumptions used to generate it.

Another mechanism to produces the ripples that has been proposed is perturbations of the disk caused by satellite galaxies. It has been suggested that the Galactic disk oscillates vertically due to radially propagating waves — i.e., bending waves caused

by the passing of orbiting Milky Way satellites (Hunter and Toomre 1969), such as the Sagittarius dSph (Ibata and Razoumov 1998; Laporte et al. 2018; Darling and Widrow 2019). Some success in modeling these features in the stellar disk (but for more limited empirical mappings of Milky Way features than presented here) has been shown by Widrow et al. (2014) and Laporte et al. (2019), who invoke a semi-analytical prescription and N-body simulation of the Sagittarius dwarf galaxy interacting with the Galactic disk to explain the oscillatory disk star patterns. In both cases, regardless of the mass of the impactor, changes in vertical velocity on the scale of 5 km s^{-1} within $R < 20$ kpc in the anti-center direction are observed, especially in Laporte et al. (2019), where their model L2 exhibits a strikingly similar overall trend to that of the observations, with vertical velocity increasing with Galactocentric radius over $5 < R < 10$ kpc to a maximum value ~ 5 km s^{-1}, and then decreasing with Galacocentric radius over radii $13 < R < 20$ kpc.

Meanwhile, in N-body simulations of passages of massive satellite galaxies around a Milky Way-like disk galaxy, D'Onghia et al. (2016) find an increasing vertical velocity over $5 < R < 10$ kpc and decreasing vertical velocity for $13 < R < 20$ kpc, as well as some smaller ripples within $7 < R < 10$ kpc. Ripples in the radial dimension as large as 20 km s^{-1} have been detected in the D'Onghia et al. (2016) simulations that are attributable to the Galactic warp itself.

At present, we offer no definitive explanation for the fine structure seen in the kinematical trends in Figures 2.3 and 2.7. Like Schönrich and Dehnen (2018), Huang et al. (2018) and Friske and Schönrich (2019), we point out these high frequency kinematical features but do not offer a physical model to explain them. On the other hand, we find that either (or both) the spiral arm and satellite perturbation scenarios seem viable. For the remainder of the analysis here, we focus on attempting to describe the

more global trends visible in Figures 2.3-2.8) — in particular, the large scale trends one might expect to be produced by a large disk warp.

2.4 Modeling the Global Properties of the Observed Vertical Disk Motions

We can treat stars as a collisionless fluid and apply the first Jeans equation to link the kinematics of Galactic stars to their number density through the Collisionless Boltzmann Equation (CBE hereafter) (Jeans 1915; Henon 1982). A simple analytical model for the Galactic warp can be derived using the CBE (e.g., Equation 11 in Drimmel et al. 2000), after adopting several simplifying assumptions. Here we follow the Drimmel et al. (2000) approach, but without making as many simplifications. For example, Drimmel et al. assume there are no net radial motions, i.e., $v_R = 0$. However, our datasets binned in vertical angular momentum, L_z, and Galactocentric radius, R (see Figure 2.7 and Figure 2.8, respectively), show an even larger velocity range in the radial direction (from -5 to 7 km s^{-1}) than in the vertical direction (from -4 to 4 km s^{-1}) at $R > 6$ kpc. Therefore, we build a similar model to that of Drimmel et al. (2000), but one that accounts for a non-zero radial motion, v_R. While our model attempts to take another step in degree of sophistication, it is still very simple and does not capture all of the possible physics. In particular, it does not include warp lopsidedness.

The essence of the model is to treat the Galactic warp as a perturbation in the Milky Way disk. For an unperturbed (non-warped) disk, one can assume perfect axisymmetry for simplicity, eliminating the dependence of the unperturbed parameters on

Galactocentric azimuthal angle, ϕ. Moreover, one can assume that the unperturbed number density is a separable function with respect to Galactocentric radius R and distance from the Galactic plane z:

$$n(R, z) = f(R)g(z) \tag{2.1}$$

In this circumstance, the addition of a Galactic warp perturbation would only have an effect on the vertical direction. Namely, stars that reside at a given position (R, ϕ, z) are deviated by $z_0(R, \phi, t)$. Therefore, the perturbed number density of stars can be written as

$$n'(R, \phi, z) = n(R, z - z_0) = f(R)g(z - z_0) \tag{2.2}$$

Accounting for the warp, according to Drimmel et al. (2000), one could write z_0 as

$$z_0 = h(R)\sin(\phi - \phi_w + \omega_p t) \tag{2.3}$$

where $h(R)$ is the deviation from the Galactic mid-plane at a given Galactocentric radius R, ϕ is the Galactocentric azimuthal angle, ϕ_w is the line of nodes at present day ($t = 0$) — i.e., where there is no vertical displacement ($z_0 = 0$) — and ω_p is the precession rate of the warp.

An analytical form of $h(R)$ is given in Drimmel et al. (2000), but Romero-Gómez et al. (2019) pointed out that a model with an ending radius of the Galactic warp and flexible exponents in $h(R)$ would reproduce observed kinematical patterns better. Thus, we adopt a new analytical form of $h(R)$ by merging the models from these two

above-mentioned sources:

$$h(R) = \begin{cases} 0 & R \leq R_1 \\ \frac{R_w}{R_2 - R_1}(R - R_1)^\alpha & R_1 < R \leq R_2 \\ h(R_2) + \frac{dh}{dR}|_{R=R_2}(R - R_2) & R > R_2 \end{cases} \tag{2.4}$$

where R_1 is the starting radius of the warp, R_2 is the ending radius of the warp, R_w is a scale factor for the warp height, and the exponent α characterizes the shape of the warp. We can write the first Jeans Equation in cylindrical coordinates as

$$\frac{\partial n'}{\partial t} + \frac{\partial (n' \overline{v_R})}{\partial R} + \frac{1}{R}\frac{\partial (n' \overline{v_\phi})}{\partial \phi} + \frac{\partial (n' \overline{v_z})}{\partial z} = 0. \tag{2.5}$$

However, because v_ϕ is not perturbed by the warp, one can still apply the axisymmetric condition, so that $\frac{\partial \overline{v_\phi}}{\partial \phi} = 0$. We also adopted the assumption $\frac{\partial \overline{v_z}}{\partial z} = 0$ made by Drimmel et al. (2000) for simplicity. After using the product rule of derivatives and applying the above assumptions, one finds

$$\begin{aligned} [\overline{v_z} - (\frac{\overline{v_\phi}}{R} + \omega_p) h(R) \cos(\phi - \phi_w + \omega_p t) - \\ \overline{v_R} \frac{dh}{dR} \sin(\phi - \phi_w + \omega_p t)] f(R) \frac{dg}{dz} \\ + \overline{v_R} \frac{df}{dR} g(z - h(R) \sin(\phi - \phi_w + \omega_p t)) + \\ \frac{\partial \overline{v_R}}{\partial R} n' = 0 \end{aligned} \tag{2.6}$$

Unlike the more simplified treatment in Drimmel et al. (2000), here the factors n', $f(R)$ and $g(z)$ do not cancel out. We assume the initial mass function (IMF) is a constant across the entire galaxy, so that the number density of stars is directly proportional to the mass density of the stellar disk. From the similarity in behavior

displayed between the *Gaia* versus *Gaia*-APOGEE samples in Figure 2.3 we conclude that the outer disk, where the warp happens and which is the focus of our interest, is dominated by thin disk stars; thus we can safely assume the mass density follows a double exponential potential like that followed by thin disk stars. Thus, we assume

$$n(R,z) = n_0 \exp(-\frac{|z|}{z_h} - \frac{R}{R_h}) \tag{2.7}$$

where R_h is the scale length and z_h is the scale height of the thin disk.

Adopting this as the density and the assumption that $\phi_w = 180°$, one then obtains a final equation that links together the different components of velocity:

$$\frac{\partial \overline{v_R}}{\partial R} = \frac{\overline{v_R}}{R_h} + \frac{sign[z-z_0]}{z_h}\left[\overline{v_z} - \left(\frac{\overline{v_\phi}}{R} + \omega_p\right) h(R)\cos\theta \right. \\ \left. -\overline{v_R}\frac{dh}{dR}\sin\theta\right] \tag{2.8}$$

where $\theta = \phi - \phi_w + \omega_p t$. Since we assume the distribution of the stellar population is symmetric about z_0, the final observed vertical velocity is the average of those with $z > z_0$ (where $sign[z-z_0] = 1$) and $z < z_0$ (where $sign[z-z_0] = -1$), yielding

$$\overline{v_z} = \left(\frac{\overline{v_\phi}}{R} + \omega_p\right) h(R)\cos\theta + \overline{v_R}\frac{dh}{dR}\sin\theta \tag{2.9}$$

The free parameters in our model arethe Galactocentric radius where the warp starts and ends (R_1 and R_2, respectively), the scale height of the warp (R_h), and the precession speed of the warp (ω_p). This is in contrast to those of Poggio et al. (2020), where the only allowed free parameter is the precession rate of the warp. One finds the best fit to the trend of vertical velocity with Galactocentric radius, as derived via

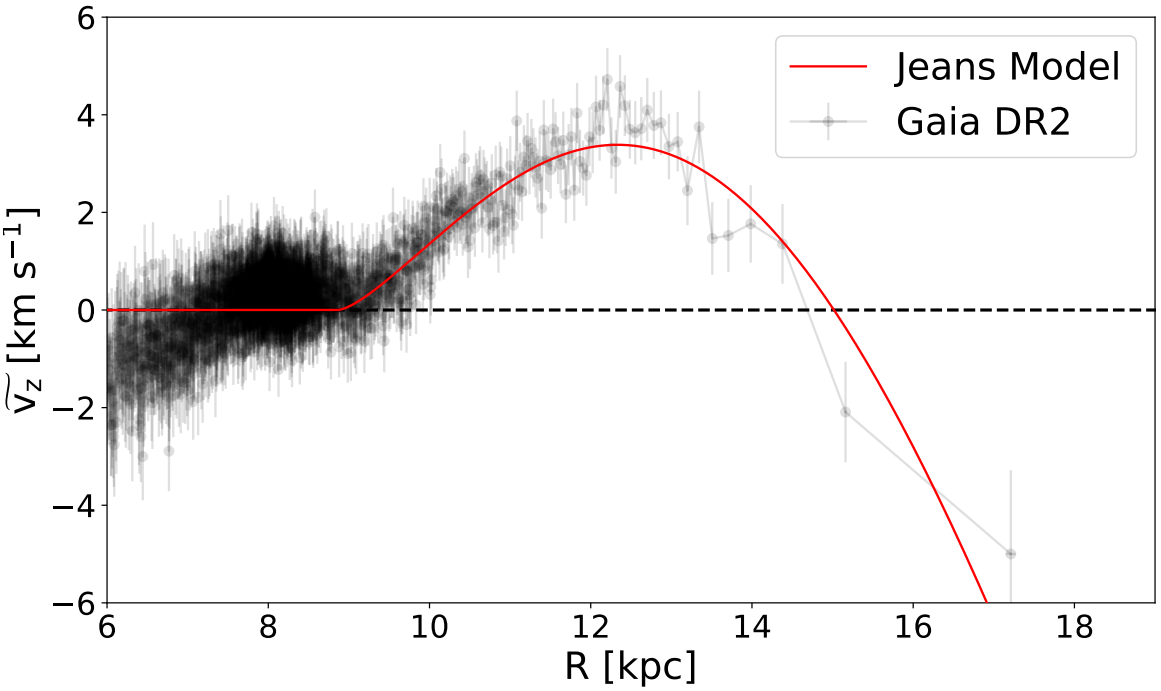

Figure 2.9: Best fit of our model (red line), inspired by that of Drimmel et al. (2000), to the *Gaia* DR2 data. The model does not work well inside the solar circle because the model is designed for, and constrained by, the outer disk. While we are only fitting $R > 8$ kpc, the radial range $6 < R < 8$ is shown because there are claims that the warp starting radius is inside $R = 8$ kpc.

a Markov chain Monte Carlo method (MCMC), is described by:

$$\begin{cases} \omega_p = -13.57^{+0.20}_{-0.18} \text{ km s}^{-1} \text{ kpc}^{-1} \\ R_1 = 8.87^{+0.08}_{-0.09} \text{ kpc} \\ R_2 = 17.78^{+1.56}_{-1.86} \text{ kpc} \\ R_w = 1.20^{+0.28}_{-0.26} \text{ kpc}^{2-\alpha} \\ \alpha = 1.53^{+0.10}_{-0.09} \end{cases}$$

The best fit is shown in Figure 2.9 in red, and the corner plot for MCMC fitting is

shown in Figure 2.10. Notice that the model does not match well in the inner part of the Galaxy. This is expected for several reasons: First, we are only fitting our model for R $>$ 8 kpc. Moreover, the Galactic warp would have very limited effect in the inner (more massive) part of the Galaxy, rendering our model inappropriate there. Figure 2.10 also shows that the model is not sensitive to the ending radius of the warp R_2. We attribute that insensitivity to the low number of stars beyond $R > 16$ kpc.

Our result for ω_p is consistent with that of Poggio et al. (2020) (again, for them, ω_p is the only free parameter and we adopt an opposite sign convention for the direction of the precession term). While our model is very crude in construction, it illustrates the possibility of explaining the decline in vertical velocity as due to a warp precessing in the direction of Galactic rotation.

Even though such a decline was also observed by Drimmel et al. (2000), they attributed it to the extremely large uncertainty in distance for stars beyond the solar neighborhood. However, that does not appear to be the case here as the number of stars within each of our binned data points is significantly higher, which greatly reduces the uncertainty of the mean value.

Our result for the Galactocentric radius where the warp begins agrees well with previously reported values. A comparison of existing models, with trends in z with R shown at the maximum vertical distance from the Galactic midplane for each, is provided in Figure 2.11. However, while the latter figure shows that there is good agreement on R_1, there is also a large spread in the amplitude of the warp among the various models. Moreover, our model agrees better with those exhibiting a stronger warp. It is worth noting that the set of models by Amôres et al. (2017), to which we show the most agreement, have included more physics (e.g., flaring, disk

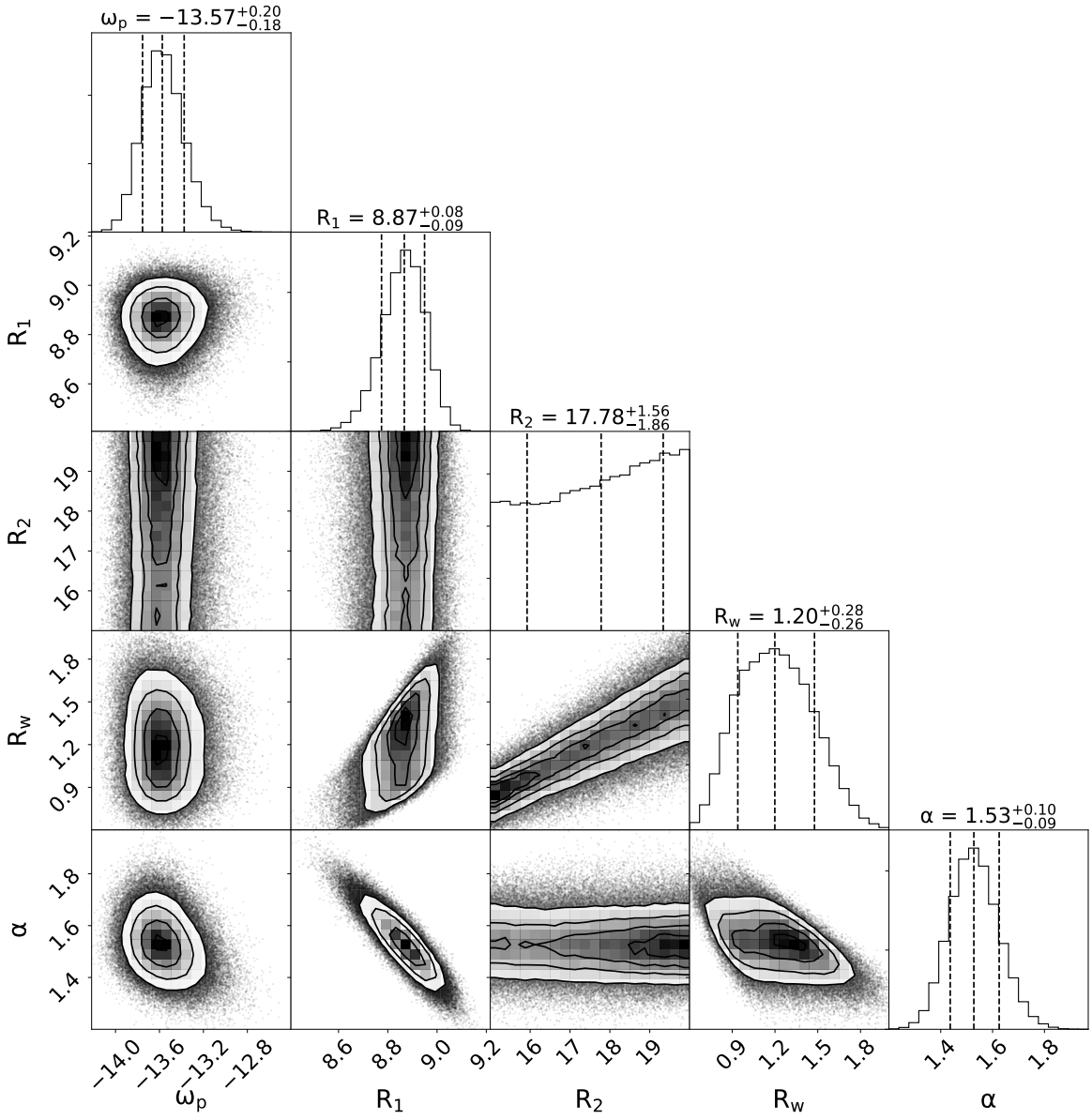

Figure 2.10: Corner plot of the MCMC fitting of the model. The fact that R_2 is not well constrained can be explained by the low number of stars beyond $R > 16$ kpc.

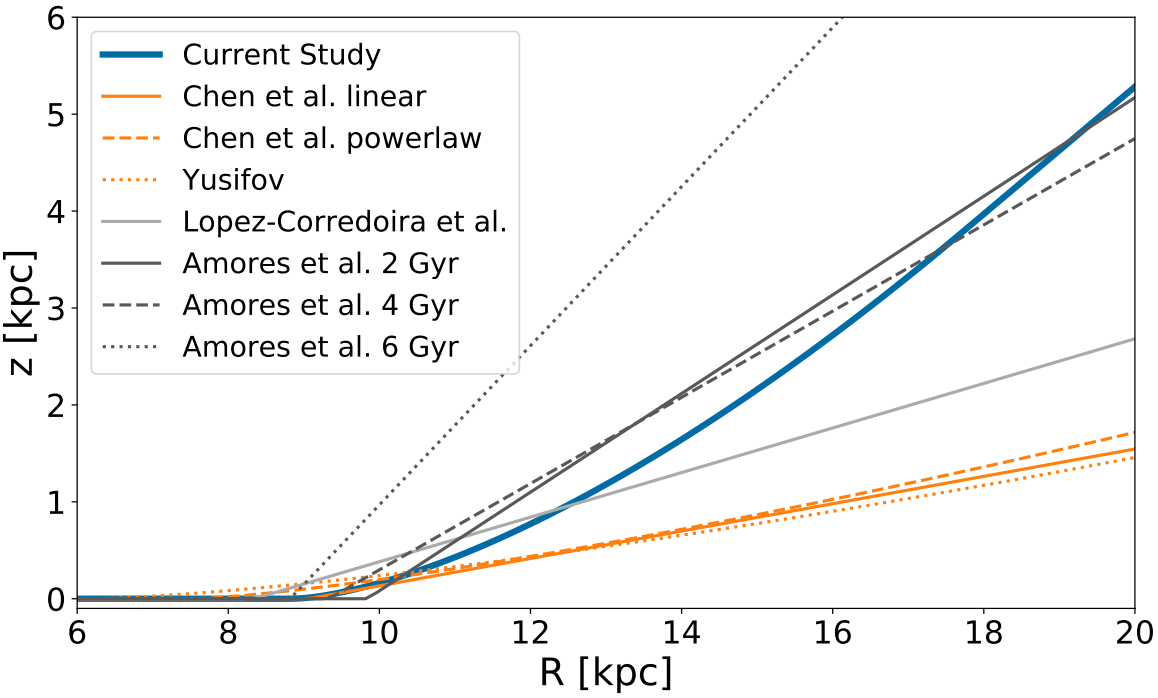

Figure 2.11: Comparison of existing Galactic warp models by Chen et al. (2019, their linear and power law models), Yusifov (2004), López-Corredoira et al. (2014), and Amôres et al. (2017, for three different ages). The comparison illustrates that there is large spread in the amplitude of the warp in existing models.

truncation, star formation history, etc.) than the other models, including ours, which is a reassuring check on our model.

2.5 Age Variations in the Character of the Galactic Warp

In the past few years there have been several lines of evidence suggesting that the parameters of the warp in the Milky Way disk change with the average age of the tracing stellar population (e.g., Drimmel et al. 2000; Amôres et al. 2017; Romero-Gómez et al. 2019; Poggio et al. 2020). In this section we use the stellar age catalog

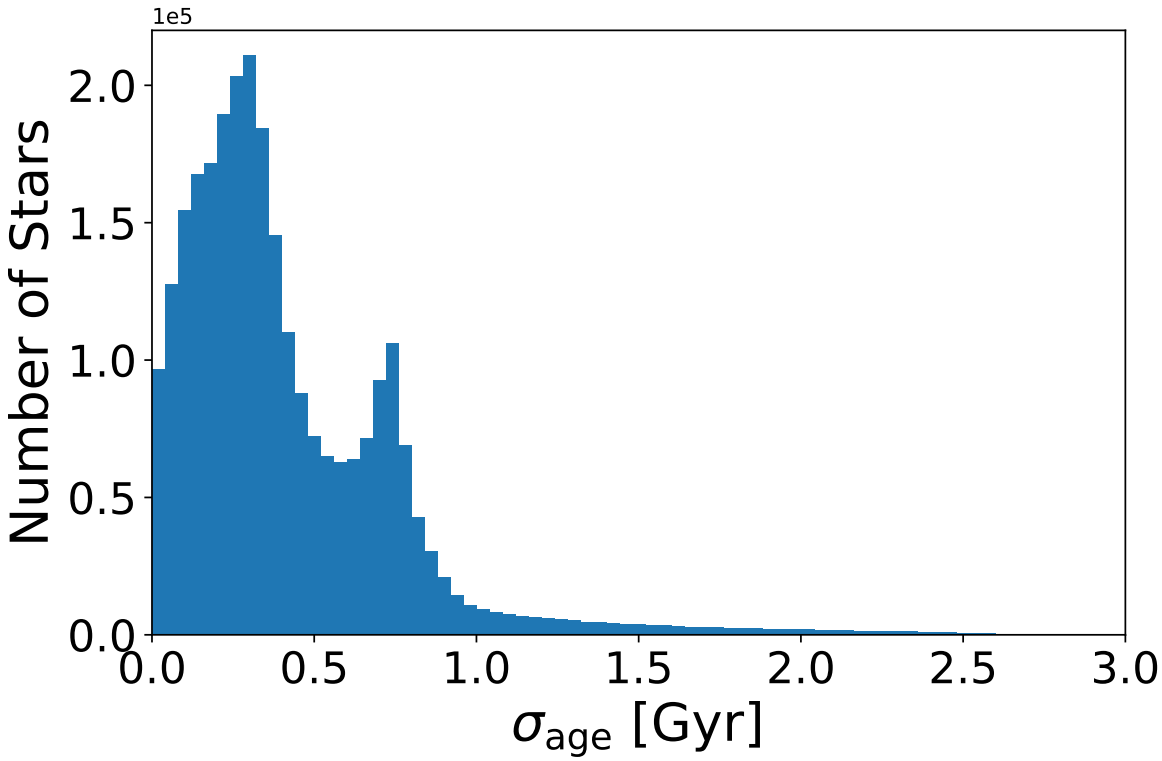

Figure 2.12: Distribution of error in ages of individual stars in Sanders and Das (2018) catalog.

provided by Sanders and Das (2018) to explore how different aged populations are warped differently. This catalog contains the ages of ∼3 million *Gaia* stars, derived using a Bayesian framework to characterise the probability density functions of age for giant stars with combined photometric, spectroscopic, and astrometric information, supplemented with spectroscopic masses, where available. We only include stars for which Sanders & Das set "flag = 0"; according to these authors, stars were assigned non-zero flags when (a) the isochrone fitting failed completely, (b) the isochrone overlapped with the data at only one point, (c) the spectroscopic or photometric input data are problematic, or (d) for which the derived ages are unreasonably small (< 100 Myr).

We acknowledge one caveat is that these ages were derived from extrapolating the

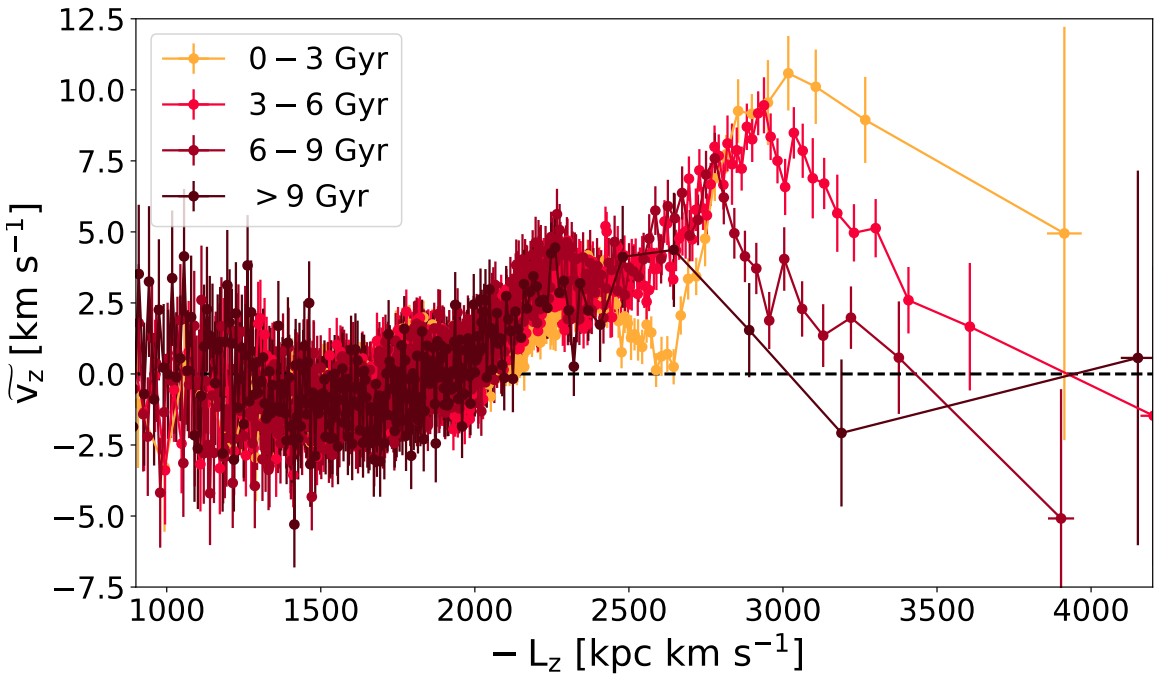

Figure 2.13: Changes in median v_z as a function of angular momentum with respect to stellar populations of different ages. Note that the young population displays a much larger vertical velocity than the old population, and all of the populations display a downward trend when the angular momentum is large enough.

relation C/N with age at the solar vicinity. Although individual stars in the Sanders and Das (2018) catalog may have a large uncertainty in their estimated age (see Figure 2.12), these estimates are of sufficient quality to sort stars broadly by age and serve as a general indicator of the average age of a population when averaging over a significant number of stars. We selected stars in four age bins: those stars with ages $0-3$ Gyr as a "young population", those with $3-6$ Gyr ages as an "intermediate age population", those $6-9$ Gyr in age as an "old population", and finally, those dated at >9 Gyr as an "ancient population".

The mean vertical velocity versus angular momentum for each of these age groups is shown in Figure 2.13. It is clear that there are major differences in this particular kinematical trend between different age populations. The young population (orange

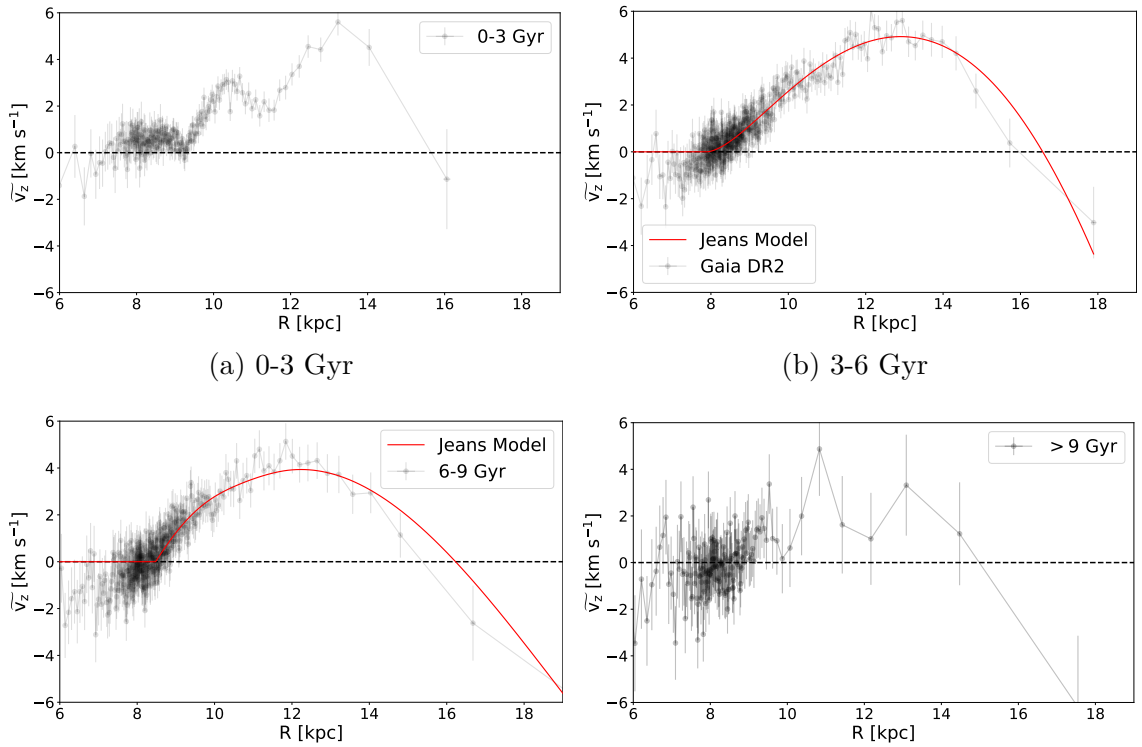

(a) 0-3 Gyr

(b) 3-6 Gyr

(c) 6-9 Gyr

(d) > 9 Gyr

Figure 2.14: Our simple model fitted to the four different age populations. For the population with stellar ages between 0 and 3 Gyr, a number of ripples between 8 to 14 kpc are detected and the drop-off in velocity is not prominent when compared to the ripples. Our simple model is not complex enough to account for these features. For the population with > 9 Gyr, due to the large error bars, it is not possible to detect any warp signature, but, on the other hand, the presence of the signature cannot be excluded. We examined the azimuthal velocity of the population and found out that it drops to < 150 km s^{-1}, which indicates a large fraction of stars are from the halo and renders our model inapplicable. Therefore, no fitting is done for the > 9 Gyr population.

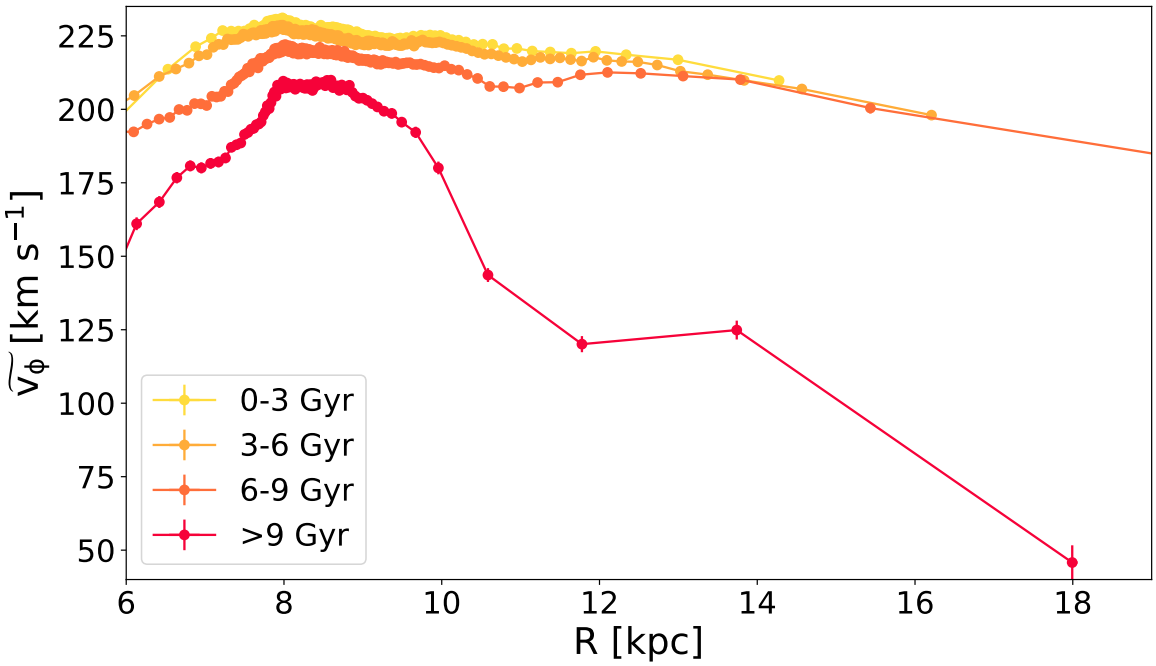

Figure 2.15: Median azimuthal velocity versus Galactocentric radius for all four populations. The rotation curve is no longer flat in the outer part of the Galaxy for the ancient population, which indicates that this population is likely dominated by halo stars in the outer part.

points in Figure 2.13) shows the largest increase in vertical velocity, and the maximum median v_z declines with increasing population age through the intermediate and old aged populations. The abrupt decline in median v_z is evident in all three populations with age <9 Gyr, albeit with slightly differing starting L_z for the beginning of the drop-off. For the ancient stars (brown points in Figure 2.13) the effect of the warp is less evident; this is likely due to the large number of halo stars within the ancient population. This conclusion is based on the character of the rotation curve exhibited by this population, which, unlike the younger star groups, shows a rapid decline beyond the solar circle Figure 2.15.

We applied our simple analytical model to fit and track the changes of parameters of the warp with stellar age in Figure 2.14. However, because our model is limited in its complexity, it cannot account for ripples not associated with the Galactic warp or non-thin-disk stellar kinematics. As a result, fitting results are not reported for the youngest population, for which prominent substructures not related to the Galactic warp are attributable to the higher frequency ripples. Nor do we report a fit for the ancient population, where, as we have shown Figure 2.15, a substantial fraction of the sample is contaminated by halo stars.

On the other hand, for the 3-6 Gyr population, our fit yields a precession rate of $-11.59^{+0.30}_{-0.25}$ km s^{-1} kpc^{-1} while for the 6-9 Gyr population we obtain $-12.19^{+0.49}_{-0.39}$ km s^{-1} kpc^{-1}. The lack of any significant difference between these two populations suggests that the response to the warp in at least these two populations is similar. However, from Figure 2.13, a clear difference in the size of the vertical velocity is present between different age populations, with the older population being slower. This difference in amplitude could be consistent with the warp being a recent event (that is, within the past 3 Gyr), but where different aged populations respond

differently in bulk: Presumably the older population, which is also the kinematically hotter population, would have a weaker response to dynamical perturbations.

Apart from differences in the amplitude of the warp in different populations, we also find that the peaks of vertical velocity are at different Galactocentric radius for different age populations (Figure 2.14). The peak vertical velocity is moving closer to the Galactic Center as the population grows older. One explanation for this is suggested by Figure 2.15, where a decrease in azimuthal velocity correlates to older populations; according to the factor $(\frac{v_\phi}{R} + \omega_p)$ in Equation 9, when the precession rate is similar between two populations, the population with smaller azimuthal velocity will have a peak closer to the Galactic Center. However, we also notice, curiously, that the fractional decrease in azimuthal velocity (that is, from ∼220 km s^{-1} for the 3-6 Gyr population to ∼210 km s^{-1} for the 6-9 Gyr population) is about a factor of two smaller than the fractional decrease in where the peak vertical velocity is located (∼13 kpc for the 3-6 Gyr population, ∼12 kpc for the 6-9 Gyr population), when these decreases should be proportional.

With no age-variable signatures in the precession of the warp but some differences in the velocity amplitude, it is worth testing whether there may be age-variable signatures in the *lopsidedness* of the warp that we previously found across the entire sample (Section 2.3.1). Figure 2.16 shows the azimuthal distribution of median vertical velocity in different age populations for different radial annuli. The lopsidedness is prominent in all age groups for radii beyond $R > 7.5$ kpc. Moreover, the lopsidedness remains similar, with the vertical velocity increasing when $\phi < 180$ deg and decreasing when $\phi > 180$ deg. The slope of increase and decrease is also similar across the different age populations. This further supports that the different age population has similar response to the Galactic warp, thus suggesting a possible gravitational

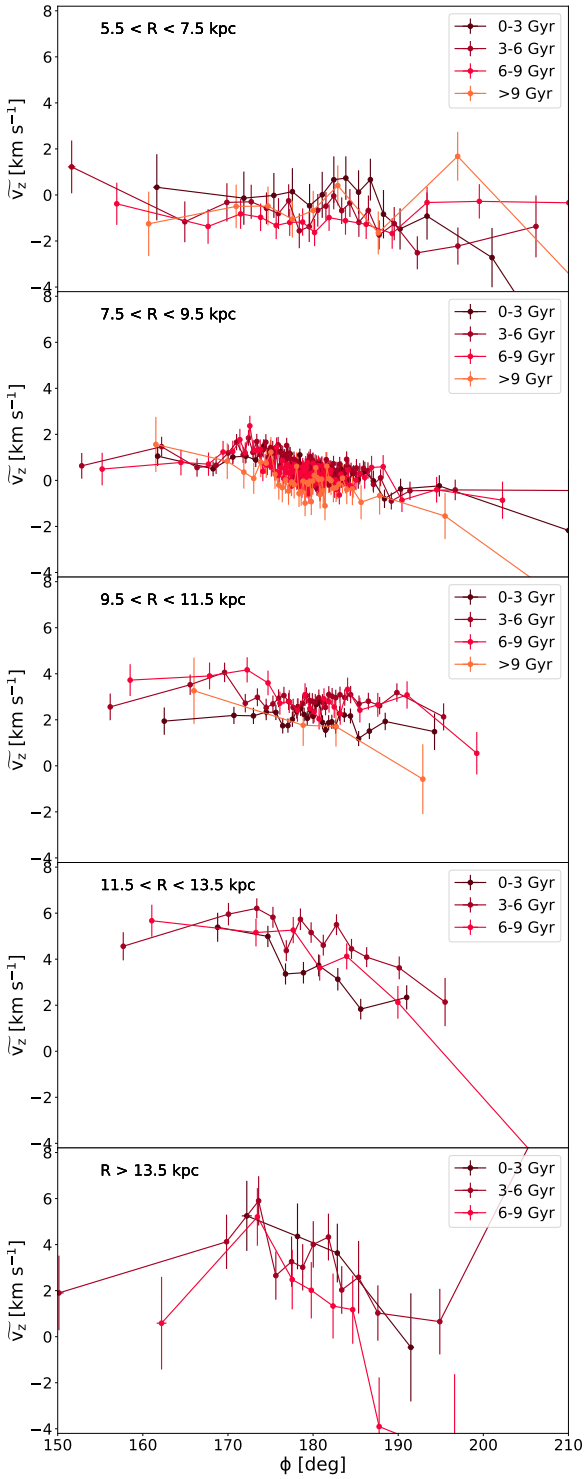

Figure 2.16: Vertical velocity as a function of Galactocentric azimuthal angle for different age bins. Stars with age > 9 Gyr and Galactocentric radius $R > 11.5$ kpc are not included due to the population being dominated by halo stars.

origin.

In the end, our consideration of potential age differences in the characteristics of the warp reveals them to be consistent with a model whereby the intermediate and older populations are both responding to a single gravitational perturbation happening less than 3 Gyr ago.

2.6 Conclusions

In this study we combine the precise stellar abundances from the APOGEE survey with the astrometry from *Gaia* DR2 and the StarHorse distance computed by Queiroz et al. (2020) to study the vertical and radial velocity components of stars with respect to the Galactocentric radius and angular momentum. We take advantage of the detailed and accurate chemical abundances available in the smaller APOGEE-*Gaia* sample (Figure 2.1) as a guide to interpretation of the much larger *Gaia*-only sample. Our analysis probes disk kinematics to a greater Galactocentric radius ($R \sim 18$ kpc) than has been explored previously (Figure 2.2). From these combined data we find evidence for the Galactic warp and characterize its onset radius and precession rate. Interestingly, a number of high spatial frequency kinematical features are also found, as has been reported by previous authors at smaller Galactocentric radii (Figure 2.3 and Figure 2.7).

We find that over a large range of L_z the overall median stellar vertical velocity $\widetilde{v_z}$ increases with L_z. Moreover, the increase of the mean vertical velocity is more pronounced for $L_z > 1800$ kpc km s^{-1} and continues until $L_z \sim 2800$ kpc km s^{-1} or $R = 13$ kpc, after which the vertical velocity sharply declines (Figure 2.3 and Figure 2.4). This abrupt decrease in $\widetilde{v_z}$ is reported for the first time. We associate

this entire global trend in $\widetilde{v_z}$ as a signature of the Galactic warp. We also study the vertical velocity as a function of the Galactocentric azimuthal angle for the *Gaia* sample, and found differences in this parameter with respect to the Galactocentric azimuthal angle for $\phi < 180°$ and $\phi > 180°$, evidence consistent with a warp line-of-nodes toward this anticenter direction (Figure 2.5). However, the velocity trends with ϕ in our data appear to be asymmetric about $\phi \sim 180°$ (Figure 2.6), which is evidence suggesting that the Galactic warp may be lopsided.

An analytical model using the Jeans Equation with consideration of a non-zero radial motion is constructed to explain the observed phenomena, and shows that the declining trend in vertical velocity can be explained as a manifestation of the Galactic warp. We find that the warp has a starting radius of $8.87^{+0.08}_{-0.09}$kpc and a precession rate of $-13.57^{+0.20}_{-0.18}$ km s^{-1} kpc^{-1} (Figure 2.9 and Figure 2.10), a value slightly higher than the 10.86 km s^{-1} kpc^{-1} reported recently in Poggio et al. (2020) (accounting for the opposite sign convention we adopt for the direction of the precession term compared to Poggio et al. 2020). Note that the parameters related to the warp itself, namely the Galactocentric radius where the warp starts and ends ($R1$ and $R2$, respectively), the scale height of the warp (r_h), and the precession speed of the warp (ω_p) are free parameters in our fitting procedure, whereas Poggio et al. (2020) only allowed as a free parameter the precession rate of the warp. Furthermore, our model illustrates that the reported decline in vertical velocity can be explained due to a warp precessing in the direction of the Galactic rotation.

We compare the spatial amplitude of our model with those of other existing models, for which there is a large spread in values (Figure 2.11). Our model agrees better with others exhibiting a stronger warp, with best match to those by Amôres et al. (2017), for which markedly additional physics is considered (e.g., flaring, disk truncation, star

formation history, etc.) than is typical for other studies, including our own.

Using two stellar populations of different ages, young (OB-type) stars and intermediate-old age (red giant branch, RGB) stars, several authors have reported that the parameters of the warp in the Milky Way disk change with the average age of the tracing stellar population (e.g., Drimmel et al. 2000; Romero-Gómez et al. 2019; Poggio et al. 2020). Here we used the stellar age catalog provided by Sanders and Das (2018) to explore how different aged populations are warped differently. We find that different aged populations show similar warp characteristics, except for velocity amplitude. The young population (0-3 Gyr) shows the largest increase in vertical velocity, and the maximum median v_z declines with increasing population age through intermediate (3-6 Gyr) and old (6-9 Gyr) populations (Figure 2.13). We also find that the abrupt decline in median v_z is present in all three populations with age <9 Gyr, albeit with slightly differing starting L_z for the beginning of the drop-off. The effect of the warp for the ancient stars (>9 Gyr) is less evident; this is likely due to the large number of halo stars within the ancient population (Figure 2.15).

We also applied our simple analytical model to track the changes of other warp parameters with stellar age. For example, for the 3-6 Gyr population our model fit yields a precession rate of $-11.59^{+0.30}_{-0.25}$ km s^{-1} kpc^{-1}, while for the 6-9 Gyr population we obtain $-12.19^{+0.49}_{-0.39}$ km s^{-1} kpc^{-1} (Figure 2.14). Meanwhile, the vertical velocity as a function of Galactocentric azimuthal angle for different age populations and radial annuli shows that the lopsidedness remains similar for these two populations (Figure 2.16).

Taken together, our study of the warp characteristics with stellar age shows similarities (precession rate and lopsidedness) and differences (velocity amplitude) that are consistent with a scenario where the Galactic warp seen in 3-9 Gyr aged stars reflects

their response to a more recent (<3 Gyr) gravitational interaction, for example a perturbation in the disk incited by a satellite galaxy.

Chapter 3

The Surface Mass Density of the Milky Way

This chapter was originally published as Cheng et al. (2024).

3.1 Introduction

The use of the vertical kinematics of stars near the Sun to measure the local density of Galactic matter has a very long history dating back to the studies of Kapteyn (1922) and Oort (1932). With continued reassessments over the past century (e.g., Hill 1960; Kuijken and Gilmore 1989a; Flynn and Fuchs 1994; Creze et al. 1998; Zhang et al. 2013; Nitschai et al. 2021) it became increasingly evident that the measured total volume and surface mass density far exceeded the baryonic contribution, and estimating these quantities became critical for proving the existence and understanding the properties of Galactic dark matter, from constraining the shape of the Milky Way's dark matter halo (e.g., Law et al. 2009; Bovy et al. 2016; Posti and Helmi 2019) to direct dark matter detection experiments that rely on precise knowledge of how dark matter is distributed in the Galaxy (e.g., Bertone et al. 2005; Del Nobile 2021). Given that the nature of dark matter is still unknown, continued attention to this venerable, century-old experiment is as relevant as ever.

While the first attempts at determining the vertical force exerted by the Galaxy — the so-called "K_Z problem" — were remarkable in their ability to exploit the meager amounts of questionable data available at the time, the results were widely discrepant with each other (see summary by Hill 1960), and yielded results far from the consensus values of today. The existence of both the thick disk and dark matter were unknown to the early pioneers. Nor could they benefit from astrometric tools with the accuracy and precision needed to measure the tiny values of parallax and proper motion needed to work beyond the immediate solar neighborhood. Obviously, great strides in both observational capability as well as modeling (including computer modeling of ever growing and better databases) have been made, and by the 1990s (e.g., Kuijken and Gilmore 1989a; Flynn and Fuchs 1994; Creze et al. 1998) the results of the K_Z problem seemed to be converging, and this lent confidence that the method was both yielding a good estimation of the Galactic potential, and a trustworthy way to estimate the dark matter density at the solar circle.

Nevertheless, despite the improving context in which it was being applied, the overall approach to solving the K_z problem has generally remained the same; that is, after assuming time invariance and a flat Milky Way rotation curve, the combination of the Jeans Equation and Poisson Equation sets up the necessary theoretical framework for solving for K_z. Constraining this analytical model depends on measurement of the density and kinematics of a "clean" tracer population, and this was often accomplished by looking at disk stars beyond a spatial vertical height threshhold of $|Z| = 1$ kpc, a distance at which the density of thick disk stars dominates that of thin disk stars, and where one can therefore avoid the complications of mixing populations having different kinematics and densities. In addition, by working towards the Galactic poles, the vertical velocity dispersion could be measured reliably from only spectro-

scopic measures of radial velocities (one means to overcome the previously nettlesome challenge of requiring high quality astrometry). The vertical velocity dispersions were then measured and fitted with a simple trend, often a linear dependence on Z. With all necessary information assumed or measured directly from observation, one can plug the numbers into the theoretical framework and calculate the vertical force. Finally, this force law is fit with a mass model, often with the dark matter density and scale height as free parameters.

Pre-*Gaia* estimates of the local[1] dark matter density, ($\rho_{\rm dm}$), using stellar vertical motions are consistent with a value just below ~ 0.01 M$_\odot$ pc^{-3}, assuming a total baryonic surface mass density $\sum_{\rm baryon}$ of 55 M$_\odot$ pc^{-2} (see Read 2014 for a comprehensive review). McKee et al. (2015) reviewed the present day stellar mass function, and the vertical distributions of both gas and stars and found the volumetric dark matter density is $\rho_{\rm dm} \sim 0.013 \pm 0.003$ M$_\odot$ pc^{-3}. Using new data on the motions and positions of the stars from the *Gaia* mission, the results of most local analyses coincide within a range of $\rho_{\rm dm} \sim 0.011 \pm 0.016$ M$_\odot$ pc^{-3} (see de Salas and Widmark 2021 for a summary of recent local estimates). In terms of the total surface density, studies over the last few decades and up to about a decade ago have found general agreement at $\sum_{\rm tot} \approx 70 \pm 5$ M$_\odot$ pc^{-2} over the column $|Z| \leq 1.1$ kpc (e.g., Piffl et al. 2014, and references therein).

However, the advent of massive new databases of astrometry and spectroscopy for Milky Way stars means that these quantities can now be refined with both increased precision in measured stellar parameters and recently gained knowledge of second order effects and the properties of stars beyond the solar neighborhood. Surprisingly, Nitschai et al. (2021) recently estimated a total surface density of only $\sum_{\rm tot} \approx 55 \pm$

[1] "Local" has traditionally been relegated to averaging over a small volume centered on the Sun and spanning a Galactic radial width $\sim$ 0.2 - 1 kpc and height $\sim$ 0.2 - 3 kpc.

1.7_{syst} $M_\odot$ pc^{-2} for $|Z| \leq 1.1$ kpc and a non-NFW dark matter density profile, using a dynamical model of the Milky Way disk from a data set that combines astrometry from *Gaia* Early Data Release 3 (EDR3) and radial velocities from the Apache Point Observatory Galactic Evolution Experiment (APOGEE; Majewski et al. 2017). This example simply points out that despite a sudden and dramatic increase in the amount of data that can be brought to bear on the problem, fundamentally the results are a strong function of systematic biases imposed by assumptions of both adopted parameters and technique. These span from differences in dealing with (or not) the presence of disequilibrium in the Galactic disk (e.g., Spicker and Feitzinger 1986; Sánchez-Salcedo et al. 2011; Widrow et al. 2012; Cheng et al. 2020), uncertainties in such basic quantities as the gas mass density contributing to $\sum_{\rm baryon}$ (e.g., Holmberg and Flynn 2000; McKee et al. 2015), and the existence of clearly distinct stellar populations like the thin and thick Galactic disk and assumptions made regarding their distributions (e.g., Moni Bidin et al. 2012; Bovy and Tremaine 2012; Hagen and Helmi 2018).

Here we explore this somewhat chaotic situation by attempting to apply the traditional methods of surface density measurement to new stellar databases that give access to large stellar samples with 6-D phase space information spanning a broad range of Galactocentric radius and vertical height, and compare it to the widely accepted Standard Halo Model (SHM) as a reference. A goal of this exercise is to investigate the validity of previously used assumptions and methodologies and their effect on the measured surface density in the solar neighborhood.

More specifically, we take advantage of the precision spectroscopic chemical abundances and radial velocities provided by the high resolution APOGEE survey combined with astrometry from *Gaia* Data Release 3 ("DR3"; Gaia Collaboration et al.

2016b; Gaia Collaboration et al. 2023) to address three areas in the mass density measurement enterprise that have received little prior attention heretofore, but that we believe present important challenges that future efforts need to reconcile:

(1) Using now well-established (e.g., Hawkins et al. 2015; Hayes et al. 2018; Duong et al. 2018) multi-element chemical criteria to discriminate the chemically distinct thin, thick disks and halo, we show that the three-dimensional velocity dispersion profiles with height above the Galactic plane for each of these two populations not only show vastly different character belying a very different dynamical history, but each set of gradients shows deviations from the simple gradients typically assumed.

(2) While the total surface mass density has been extensively studied in the past, it has been poorly explored for clean thin and thick Galactic disk samples. Almost all previous studies of the vertical mass profile have attempted to isolate presumably "pure" stellar populations using specific height ranges from the Galactic mid-plane or assumed metallicity criteria, whereas it is well known that the thin and thick disk populations (as well as the halo) show significant amounts of overlap in their spatial, kinematical and metallicity distributions (e.g., Bensby et al. 2014; Hayden et al. 2015; Anguiano et al. 2020, and references therein). For example, Moni Bidin et al. (2012), Bovy and Tremaine (2012), and Moni Bidin et al. (2015) each analyzed the kinematics of hundreds of presumed thick disk stars at 1-4 kpc from the Galactic mid-plane, while Hagen and Helmi (2018) applied a metallicity selection to attempt to discriminate thin disk red clump stars (assumed to have [Fe/H] > -0.25) from those of the thick disk (assumed to have $-1.0 <$ [Fe/H] < -0.5). Meanwhile, Guo et al. (2020) estimated the local dark matter density using stars with [Fe/H] > -0.4 and $|Z| < 1.3$ kpc.

However, a spatial vertical height selection is not a good way of achieving a clean thin

and thick separation, and, because of the different thin and thick disk scalelengths, needs to have variable tuning for different Galactocentric radii. Here we use the individual vertical velocity dispersion profiles of the much better discriminated thin and thick disk populations based on multielement chemistry to estimate the total surface density (baryons + dark matter) from each population separately. We show that vastly different results for the surface mass density of the Milky Way disk are obtained when the standard Jeans equation methodology is applied to these two populations. This shows that the traditional method breaks down when applied to the thin disk population, We discuss here potential reasons for this failure, including the adopted density law or velocity dispersion profiles being too simplistic, or because of inherent non-equilibrium in the thin disk population.

(3) The combination of APOGEE and *Gaia* allows us, for the first time, to explore the total surface density not only outside of the solar neighborhood, but across a large range of Galactocentric radius ($4 < R_{GC} < 12$ kpc) and vertical height ($-4 < Z < 4$ kpc). The results of this analysis shows that the thin and thick disk measurement values are more consistent with each other at larger Galactocentric radius, while performing the same analysis in the inner disk will result in non-negligible discrepancies.

After exploring these various avenues, we arrive at the overriding conclusion that the growing detail in hand on the chemodynamical distributions of Milky Way stars can no longer be treated with the simple, traditional analytical treatments of the K_Z problem.

The layout of the paper is as follows: §3.2 provides an overview of the data used in the study, while §3.3 describes the kinematical properties of the stellar populations and the anisotropies in the velocity field. In §3.4 we present surface mass density calculation process and results, and in §3.5 we discuss our results and findings. Fi-

nally in §3.6, we present conclusions drawn from our study, including a discussion of potential explanations for the curious results obtained in our analysis of the surface mass density.

3.2 Data

Two samples are selected for this study.

The first sample purely consists of data from the third data release of the *Gaia* mission (Gaia Collaboration et al. 2016b; Gaia Collaboration et al. 2023). This catalog provides full 6-dimensional space coordinates for 33,812,183 stars: positions (α, δ), parallaxes (ϖ), proper motions (μ_α^*, μ_δ), and $v_{\rm los}$ down to $G_{\rm RVS} = 14$. This release contains $v_{\rm los}$ for stars with effective temperatures in approximately the 3,100-14,500 K range (Katz et al. 2023). We require all astrometry parameters to be solved (`astrometric_params_solved = 31`) with no excessive noise (`astrometric_excess_noise = 0`), and stars for this study must have reported $G_{\rm BP}$ and $G_{\rm RP}$ magnitudes. In addition, we require more than five visits of *Gaia* radial velocity measurement (`rv_nb_transits > 5`) and an expected signal-to-noise ratio greater than or equal to 5 (`rv_expected_sig_to_noise >= 5`). We adopted the GSP-Phot distance for the *Gaia* sample, which was derived with the *Gaia* BP/RP spectra, G magnitudes, and parallaxes and released as part of *Gaia* DR3. We further require `ruwe < 1.4` (Lindegren et al. 2018), and remove radial velocity variable stars (i.e., potential binaries) from the *Gaia* sample (Katz et al. 2023).

The second uses a combination of radial velocity from Apache Point Observatory Galactic Evolution Experiment (APOGEE, Majewski et al. 2017), part of the Sloan Digital Sky Survey (SDSS) in its SDSS-III (Eisenstein et al. 2011) and SDSS-IV

(Blanton et al. 2017) phases, and proper motion from Gaia DR3. APOGEE employs twin spectrographs (Wilson et al. 2019) on the the SDSS 2.5-meters at Apache Point Observatory (Gunn et al. 2006) in New Mexico and the du Pont 2.5-m telescope at Las Campanas Observatory in Chile to procure high-resolution, H-band spectra for a magnitude-limited sample of red stars, mainly giants, across the whole sky. The survey provides radial line-of-sight velocities ($v_{\rm los}$) accurate to the level of a few hundred m s^{-1} (Nidever et al. 2015) as well as stellar atmospheric parameters and individual abundances for up to fifteen chemical species for more than half a million stars in both hemispheres using the APOGEE Stellar Parameters and Chemical Abundance Pipeline (ASPCAP; Holtzman et al. 2018). These spectral results are derived using the Smith et al. (2021) H-band line list combined with MARCS stellar atmospheres (Gustafsson et al. 2008; Jönsson et al. 2020) to generate a grid of synthetic spectra (Zamora et al. 2015) by use of the Synspec code (Hubeny and Lanz 2011) and nLTE calculations for various elements, including Mg, from Osorio et al. (2020). These synthetic spectra are fit to the observed spectra to determine stellar parameters and chemical abundances for each source. In this study we use the final version of APOGEE results contained in SDSS Data Release 17 (DR17; Abdurro'uf et al. 2022) and use Starhorse distances (Queiroz et al. 2020), which are an estimation of distance using a combination of Gaia EDR3 parallax (as Starhorse distances with Gaia DR3 parallax is not available), magnitudes measured from multiple sky surveys, and APOGEE stellar spectra. This sample is then divided into three subsamples, thin disk, thick disk and halo sample, chemically as shown in Figure 3.1.[2]

In the end we have 9,192,032 stars in the *Gaia* sample and 220,371 stars in the

[2]Our division of the APOGEE sample on the basis of [Mg/Fe]-[Fe/H] is sinilar to, but not exactly the same as other studies making use of APOGEE data (e.g., Hayes et al. 2018; Mackereth et al. 2019).

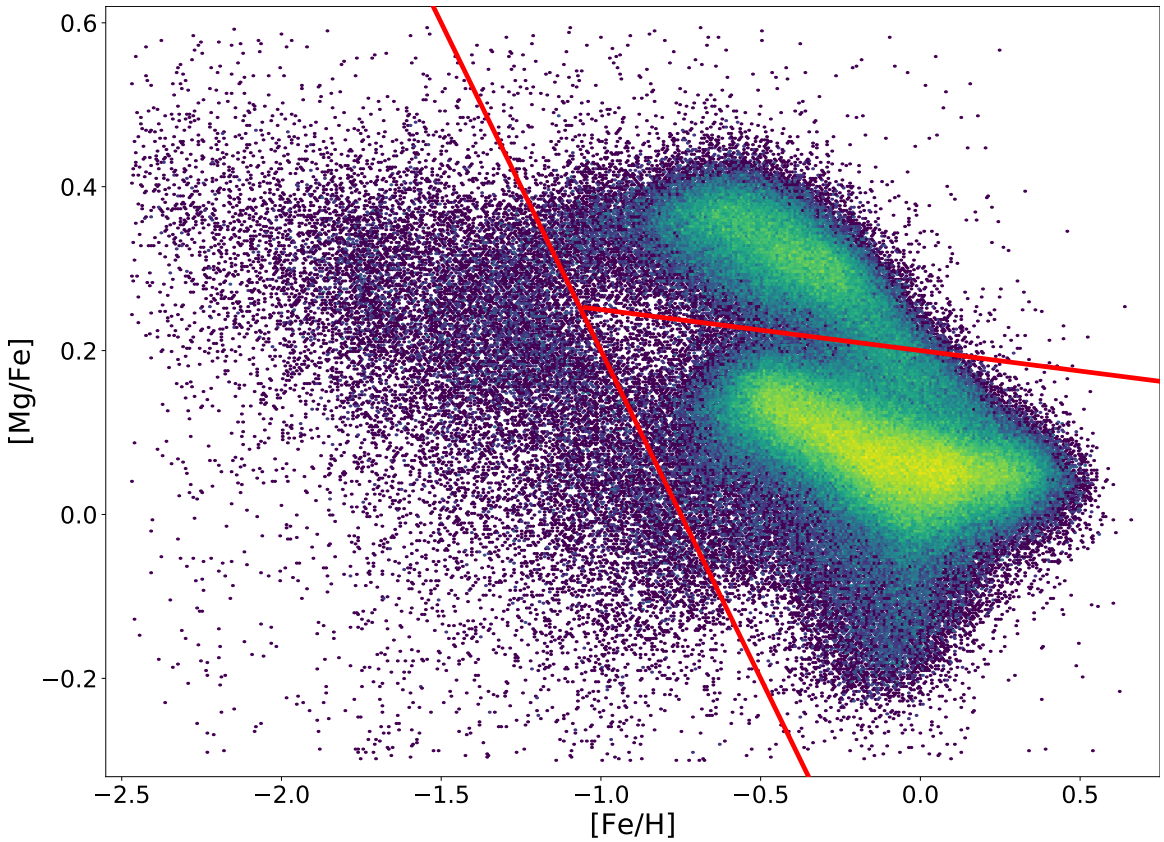

Figure 3.1: The [Mg/Fe] versus [Fe/H] for the APOGEE sample using DR17 data. We divided the sample into three subsamples as indicated by the red lines: halo stars (left), thick disk stars (top right) and thin disk stars (bottom right).

APOGEE sample. We transform the heliocentric Cartesian velocities to a Cylindrical Galactic system by assuming that the Sun is located at $(X_\odot, Y_\odot, Z_\odot)$ = (-8.122, 0, 0.0208) kpc (Gravity Collaboration et al. 2018b; Bennett and Bovy 2019) and the solar velocity is $v_\odot$ = (12.9, 245.6, 7.78) km s^{-1} (Reid and Brunthaler 2004; Gravity Collaboration et al. 2018b). We adopt a right-handed Galactic system, where $+X$ is pointing towards the Galactic center, $+Y$ in the direction of rotation, and $+Z$ towards the North Galactic Pole (NGP). We define $R = (X^2 + Y^2)^{1/2}$, as the distance from the Galactic center (GC), projected onto the Galactic plane.

3.3 Velocity Dispersion Profile

The velocity dispersion tensor as a function of vertical height Z for a range of Galactocentric radius R is needed to calculate the total surface mass density (§3.4). Stars in each the Gaia sample, thin disk subsample, and thick disk subsample are divided into 1 kpc wide bins by their Galactocentric radius R. The halo subsample, where the total number of stars is small compared to the other sub-samples (see Figure 3.1) and for which the spatial variation in kinematics is small at the position of the Sun, is not divided into radial bins. In each radial bin, stars are then sorted by vertical height Z and groups of 500 (thin disk subsample), 200 (thick disk subsample), or 2000 (*Gaia* sample) adjacent stars combined into subgroups to estimate velocity dispersions and their uncertainties via bootstrapping; the medians of the bootstrapping distributions are the velocity dispersions and their standard deviations are the uncertainties.

The velocity dispersion as a function of vertical height for different Galactocentric radius bins is shown in Figures 3.2-3.4. While the velocity dispersion with respect to Z has been generally fit with a simple linear regression (e.g., Sharma et al. 2021,

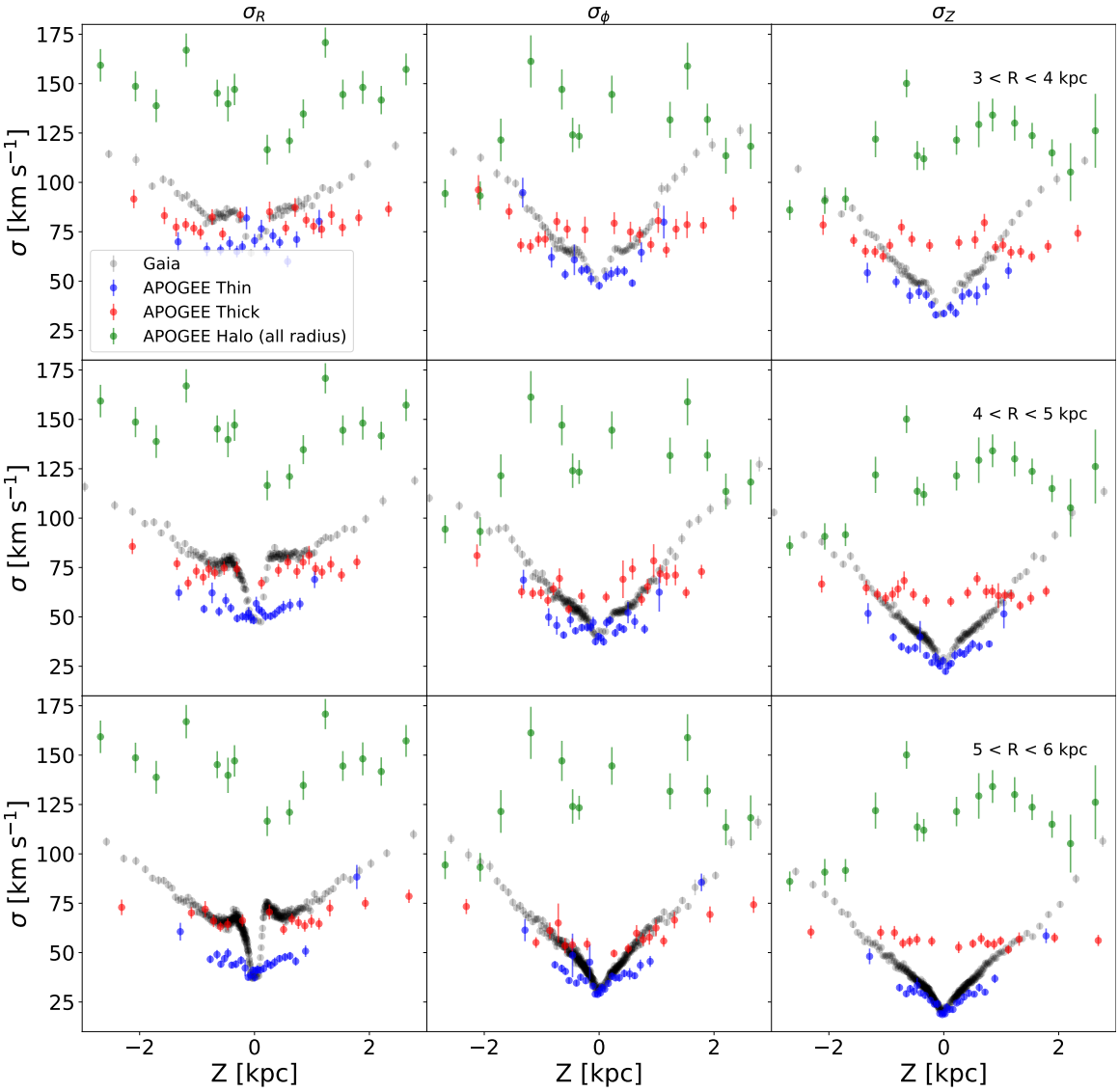

Figure 3.2: Velocity dispersion as a function of vertical height for the three velocity components, grouped by chemically selected components (thin disk, thick disk, and halo) and Galactocentric radius. Each radius bin is 1 kpc wide, and each data point consists of 2000, 500 and 200 stars for the Gaia, APOGEE thin disk, and APOGEE thick disk samples, respectively. Due to the low number of stars in the halo sample, and the halo not being the focus of this paper, each green data point represents 1000 halo stars across all Galactocentric radius. This figure includes stars with Galactocentric radius between 3 kpc and 6 kpc. The error bars are 1-σ uncertainties in the measurements.

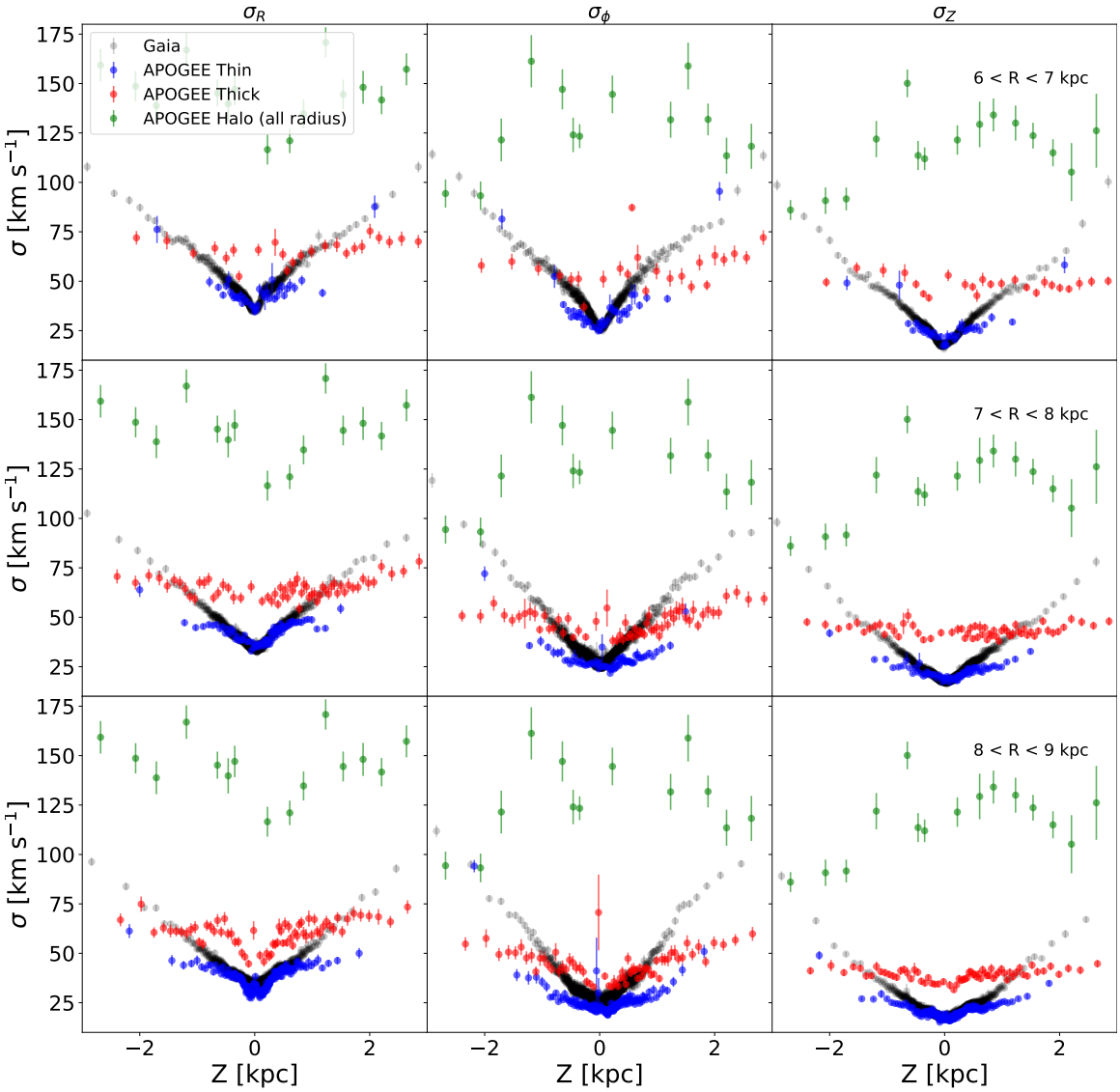

Figure 3.3: Same as Figure 3.2, bit for stars with Galactocentric radius between 6 kpc and 9 kpc.

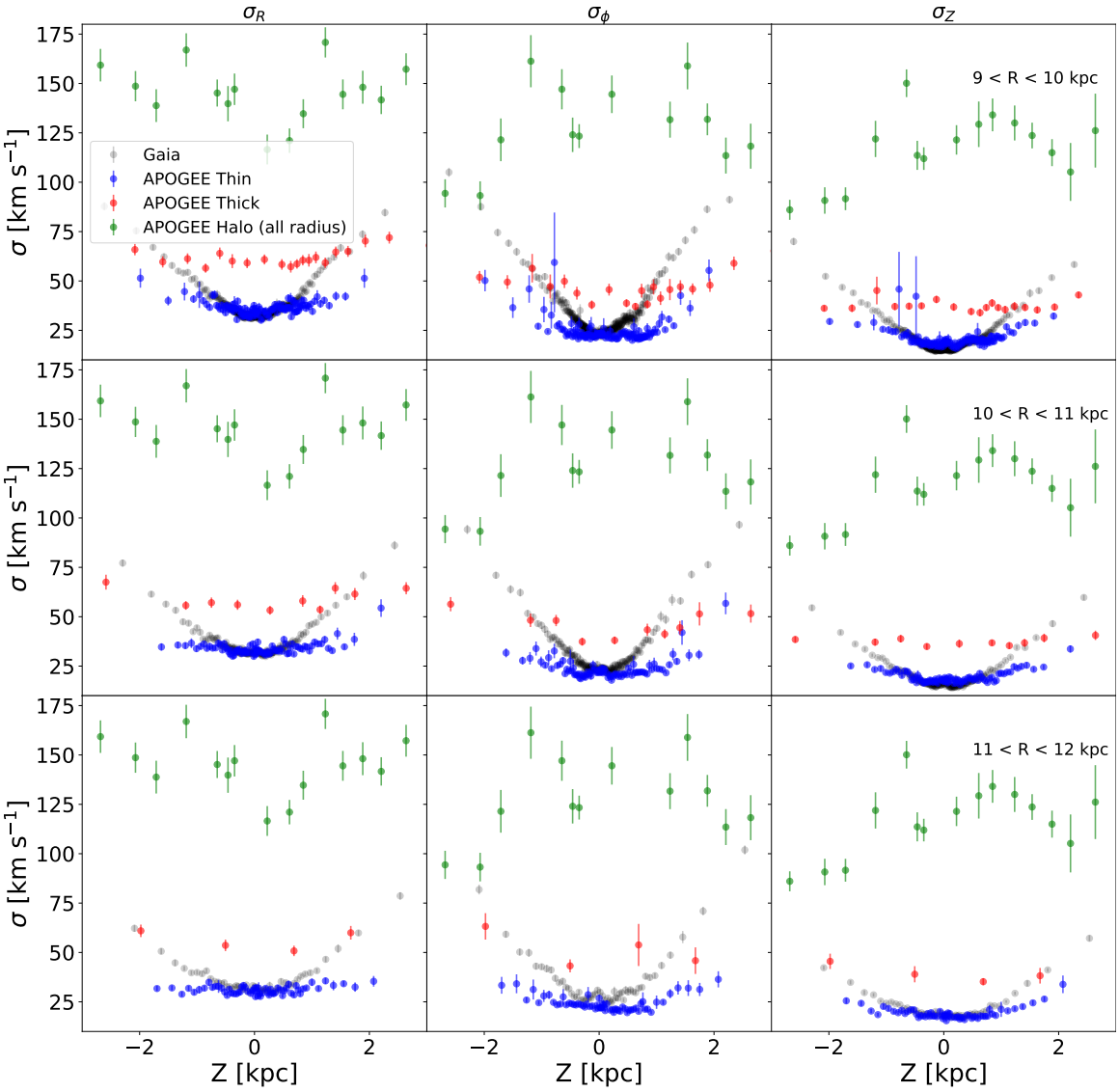

Figure 3.4: Same as Figure 3.3, but for stars with Galactocentric radius between 9 kpc and 12 kpc.

and references therein), the APOGEE and *Gaia* samples both reveal complex trends. Interestingly, the velocity dispersion variations are less pronounced for the thick disk population, a Galactic structure dominated by an intermediate-old stellar population (e.g., Norris 1987; Bensby et al. 2004; Mackereth et al. 2017). It is well established that the Milky Way disk is in disequilibrium (e.g., the '*Gaia* phase-spiral', Antoja et al. 2018; Li 2021; the 'Galactic Warp', Cheng et al. 2020; Poggio et al. 2020; and possibly the 'Triangulum–Andromeda overdensity' and other structures seen in/near the outer disk, Majewski et al. 2004; Hayes et al. 2018; Silva et al. 2020; Zhang et al. 2022). The disk is reacting to both internal non-axisymmetric perturbations, such as the bar and spiral arms (e.g., Eilers et al. 2020), and external perturbations, such as the on-going merger with Sagittarius dwarf spheroidal and the Magellanic Clouds (e.g., Kazantzidis et al. 2008; Laporte et al. 2018; Bennett et al. 2022). Indeed, internal and external non-axisymmetric perturbations like these are among the main drivers of the secular evolution of galaxies. While understanding these instabilities and their consequences on the chemo-dynamical evolution of galactic disks in general, and the Milky Way's disk in particular, is a currently a topic of great interest in galactic dynamics, exploring this is beyond the scope of this paper.

Figures 3.2-3.4 also show how the velocity dispersion as a function of Z changes with respect to Galactocentric radius R for both the APOGEE chemically distinguished populations as well as the full *Gaia* sample (see also the 2D maps in Gaia Collaboration et al. 2018a). For the inner regions ($R < 6$ kpc), there is an abrupt change in the velocity dispersion in the $0.0 < Z < 0.5$ kpc range, especially for the radial velocity component, σ_R. Bar instabilities are a dominant heating mechanism in the secular evolution of galactic disks. Recently, Walo-Martín et al. (2022) used high resolution simulations of Milky-Way mass haloes to study the effect of the bar in

the inner regions and found that σ_ϕ and σ_Z exhibit non-axisymmetric features, while σ_R velocity dispersion maps present more axisymmetric distributions. However, the abrupt changes in velocity dispersion observed in the radial component in Figure 3.2 could also be associated with the transition in the dominance of the the *Gaia* sample from thick to thin disk (see the blue/red APOGEE points in Figs. 3.2-3.4). Furthermore, Anguiano et al. (2020) showed using *Gaia* DR2 (Lindegren et al. 2018) and the APOGEE data in SDSS DR16 (Ahumada et al. 2020) that the fraction of stars that belong to the thick disk versus the thin disk quickly changes with Z for $R < 6$ kpc.

We include in Figures 3.2-3.4 the stellar halo values to highlight the fact that the chemical separation of populations helps is critical to avoiding the artificial inflation of velocity dispersions at large vertical height for thick disk population, where the halo population starts to dominate.

Figure 3.3 shows the velocity dispersion as a function of Z for the $6 < R < 9$ kpc range. We find that the thin disk population (blue dots) increases with vertical height, while the thick disk sample (red dots) remains nearly constant for a given Z. Interestingly, there is an increase and decrease in the radial velocity component around $Z \sim 0.0$ kpc for the solar circle, $8 < R < 9$ kpc, giving the σ_R distribution a tight, W-shape for the thin disk. This feature is marginally seen for the thick disks. It is possible these small scale features are artificial, as a similar increase was also seen in Gaia Collaboration et al. (2018b) and may be due to selection effects in the surveys, but it could also be associated with the wave-like pattern in the radial velocity component around $R \sim 8.5$ kpc reported in Friske and Schönrich (2019) and Cheng et al. (2020).

The dispersion for the three velocity components with respect to the Galactic vertical height for the outer regions, $9 < R < 12$ kpc, is presented in Figure 3.4. The increase in the dispersion with respect to Z for the thin disk is less pronounced for the outer

disk, getting nearly constant, particularly in σ_R, for $R = 11$-12 kpc. We also see how the number of stars in the thick disk drops quickly for Galactocentric radius larger than 10 kpc, reflecting the shorter scale length for the thick disk with respect to the thin disk (see Bland-Hawthorn and Gerhard 2016, for a review in this topic).

In the next section we use the results discussed here to estimate the total surface mass density for different Galactocentric radius.

3.4 Total surface mass

3.4.1 Methodology

Following long-followed convention, we estimate the total surface mass density of the Galactic disk from stellar kinematics using the Poisson and the Jeans Equations (e.g. Bahcall 1984; Holmberg and Flynn 2000; Moni Bidin et al. 2012; Bovy and Tremaine 2012; Hagen and Helmi 2018; Guo et al. 2020), but, for the first time, we do so for chemistry-based selections of both thin and thick disk sub-samples and using more than simply metallicity (see §3.2).

In our analysis we follow the approach developed in Bovy and Tremaine (2012), where

- the Galaxy is in a steady state condition, so that we can use the time independent vertical Jeans Equation;
- there is no bulk motion in either the radial or vertical direction (thus, $\sigma^2 = \overline{V^2}$);
- we adopt a circular rotation curve that is assumed to be flat at all vertical heights;

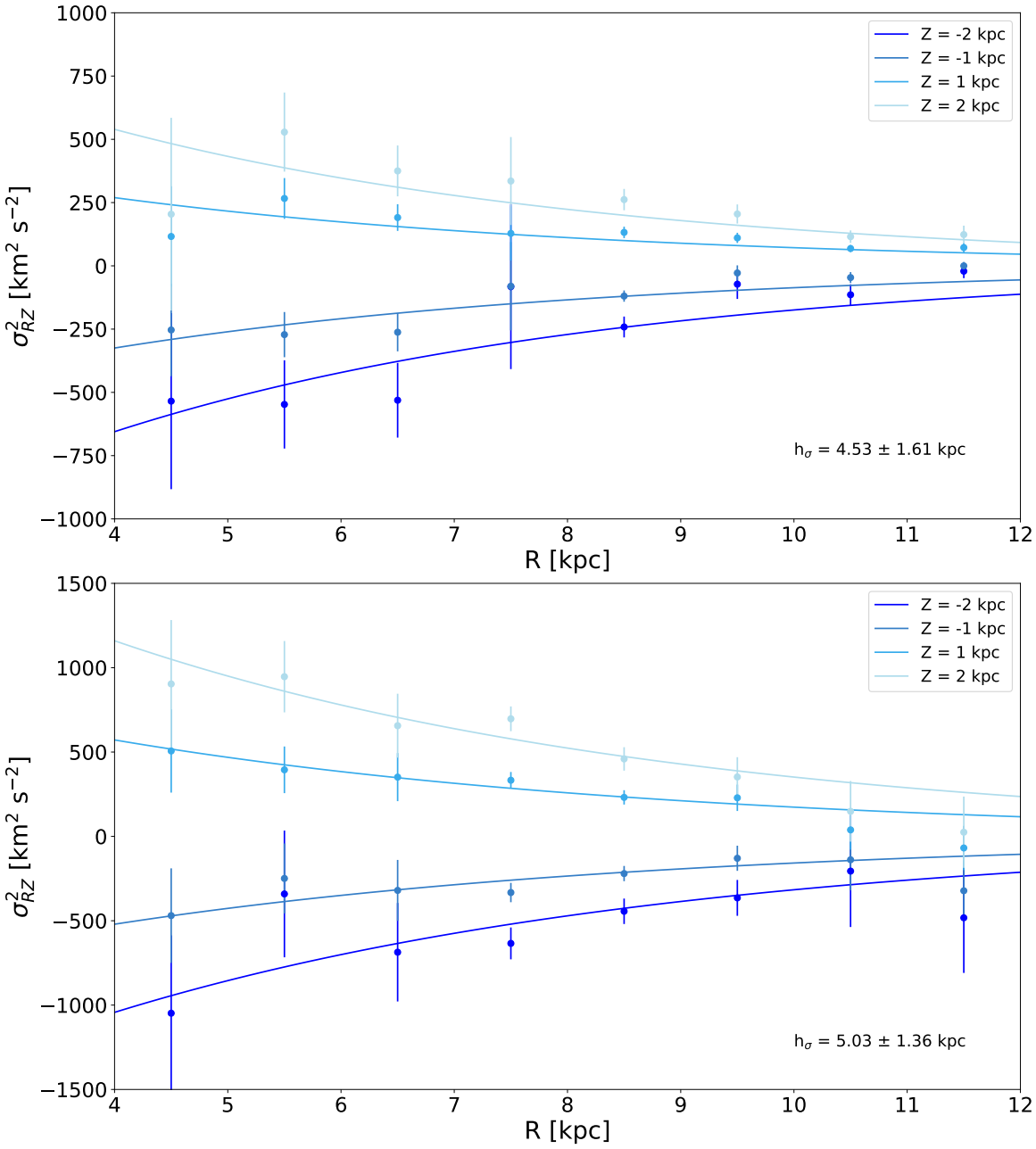

Figure 3.5: Top-panel: The measured values of σ^2_{RZ} as a function of Galacocentric radius, R, for four specific values of distance from the Galactic plane, $Z = \pm 1, \pm 2$. The curves represent best fit of an exponential function with the same scale length h_σ at different vertical heights. Bottom-panel: The same for the thick disk population.

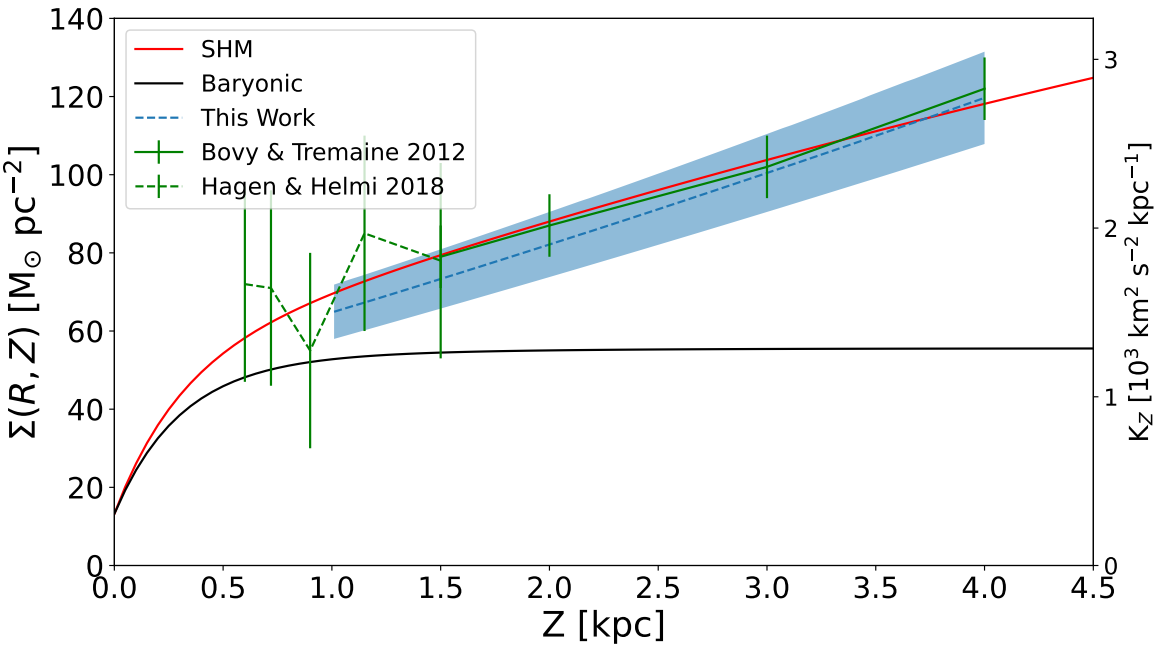

Figure 3.6: Surface mass density in the solar neighborhood from this work (using Gaia + APOGEE), Bovy and Tremaine (2012, using SEGUE) and Hagen and Helmi (2018, using TGAS + RAVE).

- the Galaxy is symmetric about its mid-plane, so that velocity dispersions, stellar number densities and the total/baryonic mass density are all symmetric about the midplane;
- the stellar number densities for the thin and thick disk follow an exponential decay with Galactocentric radius, R, and vertical distance from the midplane, $|Z|$;
- commonly accepted values for both the scale height and scale length are adopted, with an assumed 10% uncertainty: $h_Z = 0.3$ kpc and $h_R = 2.6$ kpc for thin disk, and $h_Z = 0.9$ kpc and $h_R = 2.0$ kpc for thick disk (Bland-Hawthorn and Gerhard 2016);
- the vertical velocity dispersion, σ_Z, is linear with vertical distance to midplane $|Z|$; and

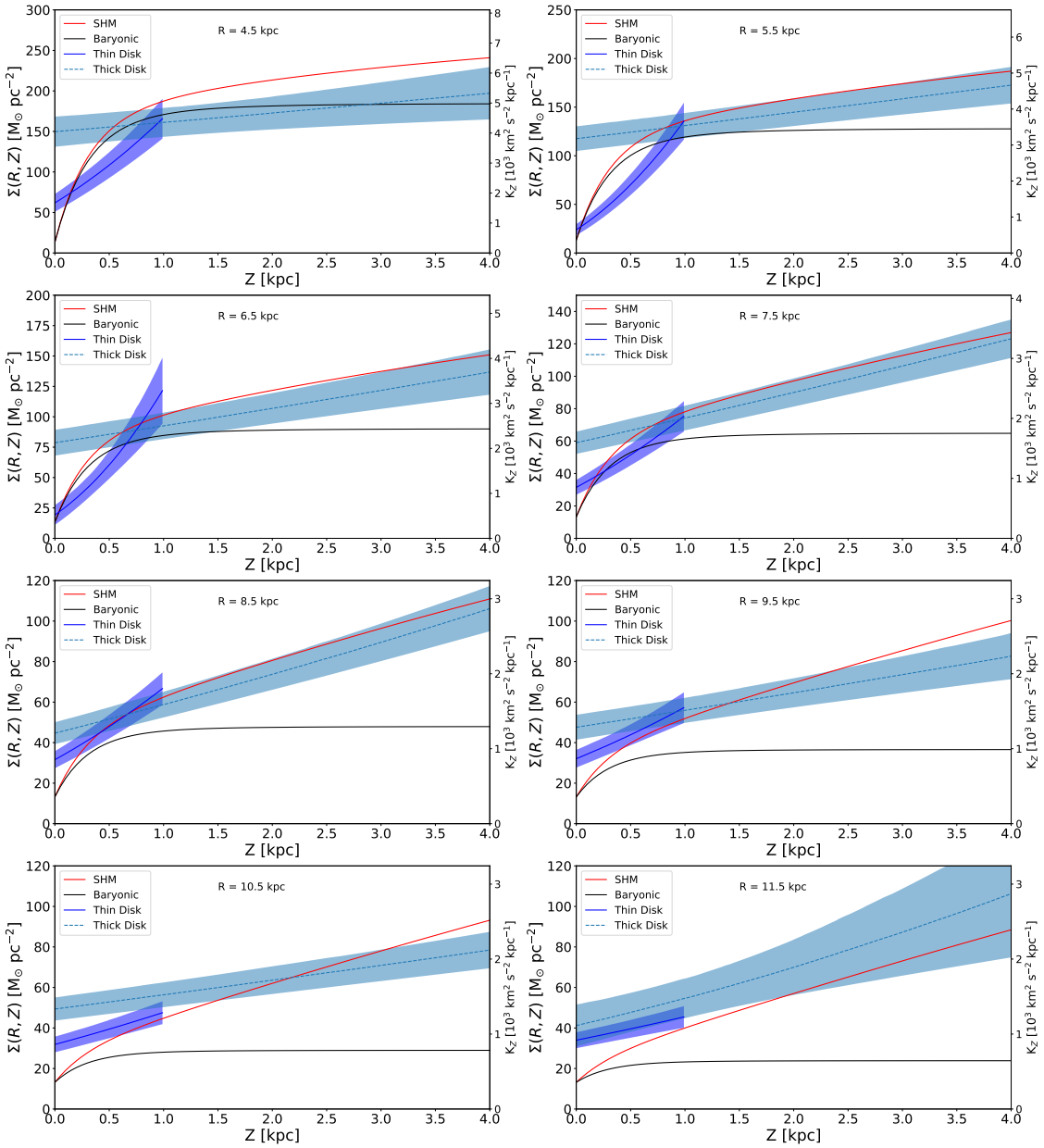

Figure 3.7: Total surface mass density (left ordinate axis) and vertical force (right ordinate axis) for different Galactocentric radii. The solid dark blue line and shaded areas representing its 1σ uncertainty represent the thin disk while the dotted blue line and blue shaded area repesent the thick disk. The Standard Halo Model (red curve, parameters from Weber and de Boer 2010) and the baryonic (black curve, parameters from Bland-Hawthorn and Gerhard 2016) distributions are also shown.

- σ^2_{RZ} is exponentially decaying with Galactocentric radius R, with its scale length h_σ a constant with Z within each population. We also assumed σ^2_{RZ} as an odd linear function of Z at each radius.

Due to the low number of stars to estimate velocity dispersion above $|Z| > 1$ kpc for the thin disk population, which is more than 3 times the scale height of the thin disk, a cut at $|Z| = 1$ kpc is applied in surface density calculation for the thin disk population.

Plugging all the above assumptions into the Poisson Equation and Jeans Equation, one finds the same equation as in Bovy and Tremaine (2012):

$$\begin{aligned}\Sigma(Z) &= -\frac{F_Z(Z)}{2\pi G} \\ &= -\frac{1}{2\pi G}\left[-\frac{\sigma^2_Z}{h_Z} + \frac{\partial\sigma^2_Z}{\partial Z} + \sigma^2_{RZ}\left(\frac{1}{R} - \frac{1}{h_R} - \frac{1}{h_\sigma}\right)\right]\end{aligned} \tag{3.1}$$

The linear fitting of the velocity dispersions is further described in Appendix A, where the uncertainties in the velocity dispersion are estimated using a bootstrapping test. Figure 3.5 shows the measured trends of σ^2_{RZ} for four representative separations from the disk midplane. The fitted curves in Figure 3.5 reflect our measured scale lengths for σ^2_{RZ}, which we determined to be $h_\sigma = 4.53 \pm 1.61$ kpc and 5.03 ± 1.36 kpc for the thin and thick disk, respectively. In previous studies, Moni Bidin et al. (2012) assumed $h_R = h_\sigma = 3.8$ kpc, while Bovy and Tremaine (2012) prefer a shorter scale length for the dispersion profile, $h_\sigma = 3.5$ kpc. Our derived values are larger but within the errors than the h_σ reported by these authors. No significant difference is found for the dispersion scale lengths of the chemically differentiated thin and thick disks (see Figure 3.5).

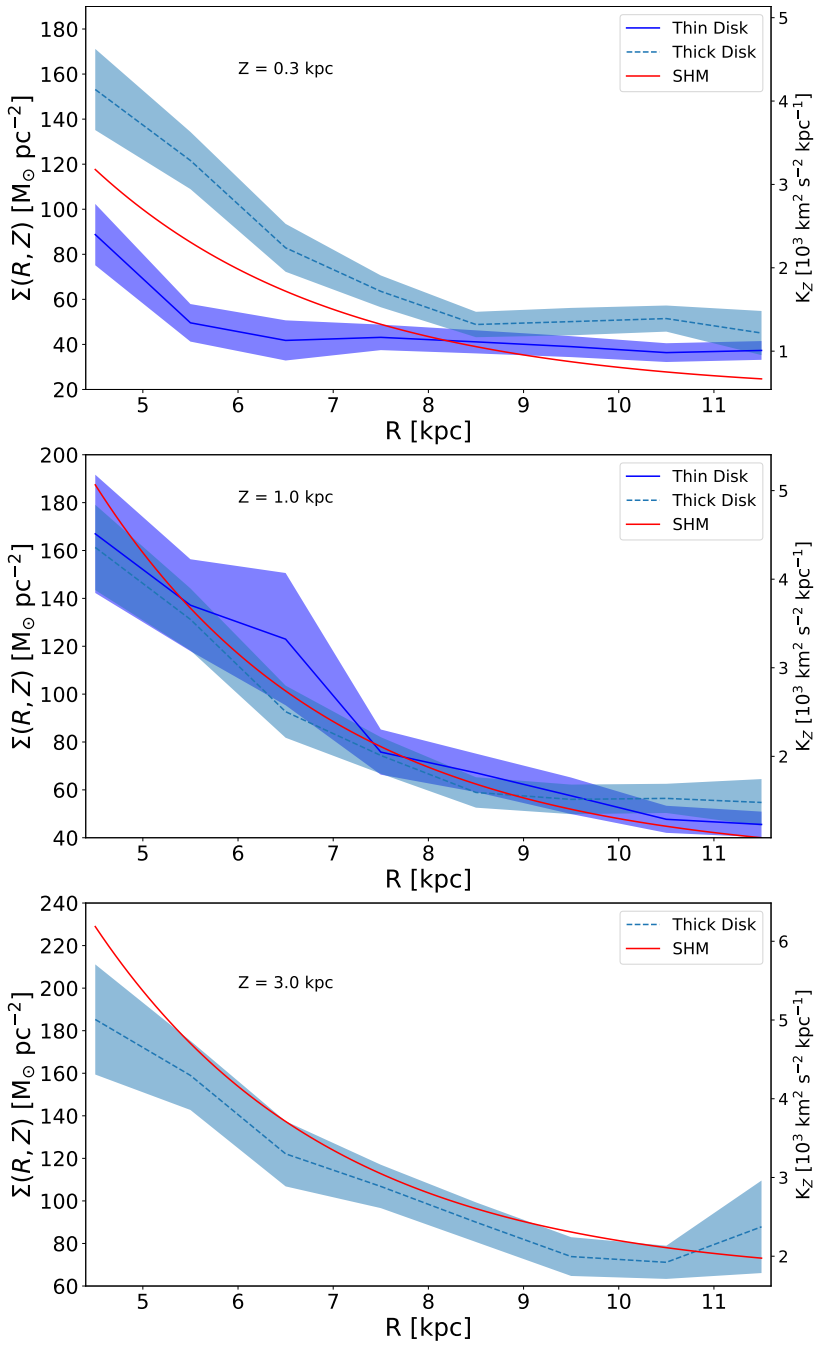

Figure 3.8: Total surface mass density (left ordinate axis) and vertical force (right ordinate axis) as a function of Galactocentric radius over the column $|Z| \leq 0.3$, 1.0, 3.0 kpc, respectively. The dark blue shaded area represents the thin disk while the light blue area is for the thick disk. The expectations for the Standard Halo Model are shown by the red curves.

3.4.2 Surface Density at the Solar Circle

With the required inputs in hand, the total mass density distribution and the vertical force were measured using Equation (3.1). To validate our approach, we first present our surface density measurement using thick disk stars at the solar circle ($R = 8$ kpc) in Figure 3.6. The figure compares our results to those of two other recent studies where a derived surface mass density at the solar circle is presented, namely (1) Bovy and Tremaine (2012), who base their measurement on SEGUE data for stars with $|Z| > 1$ and with no discrimination of thin disk, thick disk, and halo stars, and (2) Hagen and Helmi (2018), who base their result on the combination of TGAS and RAVE, and use an $-0.5 <$ [Fe/H] < -1 criterion as a means to select thick disk stars.

Despite the differences in the selection of the parent sample, we find a general agreement between our measurement based on multi-element discrimination of thick disk stars and those of these previous surveys over the range of $|Z|$ for which there is overlap. This agreement partly reflects the facts that we are using similar approaches, but also that the thick disk significantly dominates the stellar density by $|Z| = 1$. Moreover, the result appears to be robust to the definition of the thick disk, since, as may be seen by reference to Figure 3.1, the Hagen and Helmi (2018) metallicity selection is missing the significant fraction of thick disk stars with [Fe/H]> -0.5. In addition, Hagen and Helmi (2018) derive the thick disk scaleheight as a free parameter (and obtain $h_Z = 1.12$ kpc), whereas, like Bovy and Tremaine (2012), we assume $h_Z = 0.9$ kpc.

It is also worthwhile to compare our results against those of theoretical models. Here we compare the derived mass density distributions with the Standard Halo Model

(SHM) (e.g., Evans et al. 2019, and references therein). Figure 3.6 shows the baryonic contribution to the model, with the stellar matter following an exponential disk having parameters taken from Bland-Hawthorn and Gerhard (2016), with the addition of 13.2 $M_\odot$ pc^{-2} from a gas disk, as has been done in previous studies. The dark matter follows an NFW profile (Navarro et al. 1997),

$$\rho = \rho_c \frac{R_0}{r} \left(\frac{1 + R_0/R_c}{1 + r/R_c} \right)^2, \tag{3.2}$$

where $r = \sqrt{R^2 + Z^2}$, $R_c = 10.8$ kpc and $\rho_c = 0.0084\ M_\odot\ pc^{-3}$ (Weber and de Boer 2010).

The full model, including baryonic and dark matter, is represented as the red line in Figure 3.6. We find that the trend from all results shown agree with the predictions of the Standard Halo Model, although this is somewhat by definition in the case of Hagen and Helmi (2018), since their methodology is constrained to match the NFW profile. In the end, at the solar circle and for $Z \gtrsim 1$ kpc, the various standard methodologies used for calculating the surface mass density appear to converge. However, as we show below, this convergence breaks down for other R and lower Z.

3.4.3 Surface Density as a Function of Galactocentric Radius

The derived total surface mass density as a function of vertical height is shown for the thin disk (dotted blue line) and thick disk (solid purple line) in Figure 3.7. The panels are divided by different Galactocentric radii, ranging from $R = 4$ kpc to $R = 12$ kpc. The shaded areas indicate 1σ bootstrap uncertainties estimates.

Because the thin and thick disk tracer populations are responding to the same gravitational potential, one expects them to reveal the same surface mass density profile. However, it is immediately obvious from Figure 3.7 that the derived mass density distribution as function of height for the chemically distinguished thin and thick disk populations are remarkably different. While the surface mass density determinations coincide at $|Z| = 1$ kpc, regardless of Galactocentric radius, we observe that the agreement between the measured surface density trend using the thin and thick disk gets steadily worse as R decreases. Such a difference suggests that at least one of our assumptions regarding the methodology or the invoked parameters input into the machinery must be faulty. We explore these possibilities in §3.5.

As with Figure 3.6, we compare our results in Figure 3.7 against those of the SHM (red lines) for all Galactocentric radii. For the thick disk at large vertical heights, we find that the measured surface density agrees with the SHM in the Galactocentric radius range $5.5 < R < 8.5$ kpc. For the thick disk at small vertical height ($Z < 1$ kpc, while the measured values are still following the straight line trend, the SHM decreases more rapidly.[3] Thin disk measurements only agree with SHM when $R = 8.5$ or 9.5 kpc and $0.5 < Z < 1.0$ kpc. The rest of thin disk measurements do not agree with SHM and would often give smaller than baryonic values in the inner disk.

Figure 3.8 shows the total surface mass density over the columns $|Z| < 0.3$ (top), 1.0 (middle) and 3.0 kpc (bottom panel) as a function of Galactocentric radius. The figure also shows the vertical force (right ordinate axis) at each $|Z|$. As pointed out above, at $|Z| \sim 1$ kpc (middle panel) there is a overall good agreement between the surface mass density calculated using the thin/thick disk tracers and the SHM. However, at

[3]The SHM model does not reach 0 density at the mid-plane for the technical reason that the gas disk is not analytically modeled like the other components, but simply treated as an adjustment of a constant surface mass density of 13.2 $M_\odot$ pc^{-2} in an infinitely thin layer. The reason that our own calculated surface mass density does not reach 0 density at the mid-plane is discussed in Section 3.5.

higher vertical height ($|Z| = 3$ kpc, bottom panel), the thick disk population shows smaller values than than the predicted ones for the entire Galactocentric radius range. In addition, there are larger discrepancies between the thin disk, thick disk, and the model appear for the surface mass density values close to the midplane ($|Z| = 0.3$ kpc, top panel). We address possible reasons for these discrepancies in Section 3.5.

3.5 Discussion

In the previous section we demonstrated that while, on the one hand, our treatment of the K_Z problem yields similar results to previous studies when we focus on the thick disk population at the solar circle — perhaps not unexpectedly, since we are adopting the same methodology and nearly the same input parameters as these previous studies — on the other hand, these surface mass density results for the thick disk greatly differ from those given by the thin disk. Clearly the methodology is breaking down with at least one, and possibly multiple, assumptions that have been employed, in particular, for application to the thin disk. To try to understand the source of the discrepancy, in this section we revisit some of the assumptions made in standard treatments of the surface mass density measurement, such as we have followed here (e.g., an axisymmetric Galaxy, a steady state system, a simple linear fit to model the velocity dispersion with vertical height), and explore in more detail their effect on the computed surface mass density. However, we preface this discussion with the summary result that none of the following explorations seem to lead to a satisfactory explanation for the discrepancies we have observed, e.g., between the measurements provided by the two disk populations and between those measurements and the SHM. Implicit in the latter statement is that the SHM itself is a reliable prescription for the

mass profile of the Galaxy; however, we explore that assumption in Section 3.5.5.

3.5.1 Density Profile

One of the most important assumptions we have made is the nature of the density profiles. We assumed that for each the thick and thin disks, a single exponential profile could accurately describe the true distribution of the tracer population. As stated in §3.2, we assumed the most commonly assumed scale height of $h_Z = 0.3$ kpc for the thin disk and $h_Z = 0.9$ kpc for the thick disk, and we adopted an associated 10% uncertainty on these parameters.

While we are capable of reproducing results from previous studies, and achieve a reasonable agreement between the SHM and the surface density measurement from the thick disk population above 1 kpc at the solar radius, it is clear that the calculated values below 1 kpc for both the thin and thick disk populations do not follow the general trend of the SHM. While close to the mid-plane the surface density for the SHM curves downward from the near straight line surface density trend it has farther from the mid-plane, Figure 3.7 shows that the calculated surface density derived from the thick disk maintains a fairly unchanged straight line trend whereas the thin disk results show an even more peculiar behavior, with an opposite curvature in the inner galaxy, indicating an *increasing* volumetric density further from the mid-plane. The latter phenomenon is particularly surprising.

Moreover,as has long been appreciated, the exponential density law introduces a discontinuity in the density law at the mid-plane that is not physical. In the past, when this discontinuity has been a problem, a sech^2 density law has often been invoked. We tested the sech^2 density law, which is the natural form dictated by a self-gravitating

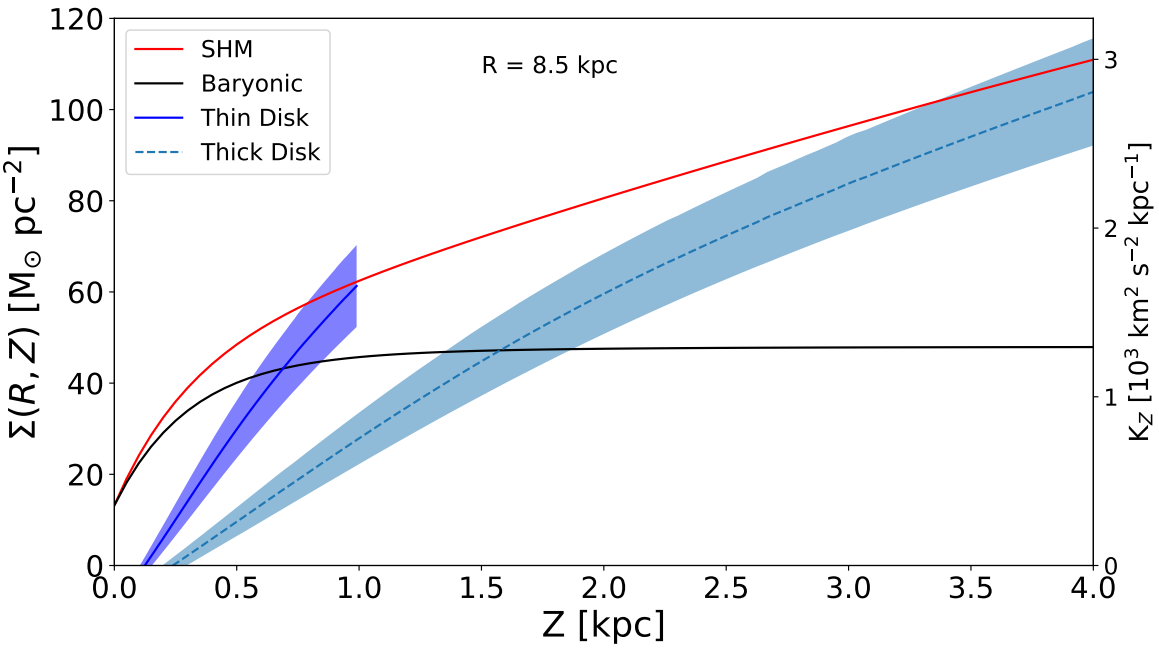

Figure 3.9: The calculated surface density when assuming a sech^2 density law in the solar neighborhood.

disk (Schulz et al. 2013); the result is shown in Figure 3.9. As may be seen, this density law removes the discontinuity at the mid-plane and also has the benefit of bending the calculated surface mass density trend downwards (in the same way as seen for the SHM); however, the calculated surface density still does not intercept the origin, and this time reaches a null surface density away from the mid-plane.

Yet another problem with the sech^2 density law is that it is simply a poor description of the true density laws near the mid-plane — where exponentials have been found to be adequate descriptors in starcount studies (Jurić et al. 2008, etc.) — and sech^2 only converges to an exponential well beyond $|Z| = 3h_Z$. So while sech^2 removes the discontinuity at $Z = 0$ and is physically motivated, the fact remains that the exponential is still found to be a better descriptor of the true (i.e., observed) density law at most Z-heights.

Another assumption we have made is that the disk is well-described by two popu-

lations with distinction density laws. This would seem to be well-motivated by the clear chemical discrimination evident in Figure 3.1. However, recent studies into stellar density distribution show that the thin and thick disk populations themselves can be subdivided further into mono-abundance populations that themselves show significantly different vertical scaleheight (Lian et al. 2022). Such a complex disk makes an analytical treatment of the problem much more challenging, requiring much finer division of empirical samples.

Beyond the solar circle things are even more problematical for standard treatments of the K_Z problem (Equation (3.1)). Apart from the problems mentioned above for inconsistencies near the mid-plane, in the inner disk ($R < 8$ kpc), we also find that the results from the thin disk are not only in clear contradiction with the prediction from the SHM, they even underestimate the baryonic model. This situation probably reflects the impact of the non-flat rotation curve in the inner Galaxy, a departure from our assumptions that invalidates Equation (3.1). Meanwhile, in the outer disk, the agreement between our measurements and the SHM are not as good as in the solar circle, with the slope in the calculated surface density being flatter than that for the SHM. In this case, evidence for flaring (e.g., Mackereth et al. 2017) and warping (e.g., Cheng et al. 2020) may one reason for the observed discrepancies.

3.5.2 Velocity Dispersion Profile

The observed velocity dispersions as a function of vertical height for a given Galactocentric radius, discussed in Section 3.3 and Appendix A, clearly reveals complex patterns. Nevertheless, for our simple treatment, we reduced the velocity dispersion variation to a simple linear trend with vertical height, as all previous similar studies

have done. Such linear trends ignore small-scale variations but capture the overall global trends of the velocity dispersions. However, this linear assumption, when combined with an exponential density law, will also lead to a discontinuity of surface density at the midplane.

Appreciating these shortcomings of the traditional method, we attempted to use a purely data-driven technique, with a spline-fit describing the complex variations in the trends. Unfortunately, this approach inevitably gives rise to sections in the $\Sigma(Z)$ profile with an unphysical, negative Z-slope. We also attempted to use other analytical forms to fit the velocity dispersion that are continuous at $Z = 0$. These results are discussed in Appendix B. In summary, when combined with a sech ^{2} density profile, while continuous at the midplane, the derived surface density also shows large deviations from previous measurements and the SHM at large vertical height as well as large discrepancies between the thin and thick disk measurements. The fitting figures and calculated surface densities are presented in Appendix B.

3.5.3 Integral Versus Differential Approach

While most recent studies (e.g., Bovy and Tremaine 2012) use the differential form of the Jeans and Poisson equations, Kuijken and Gilmore (1989b) employed the integral form of these equations. Here we provide a brief overview of this process. The principal equation is

$$\nu\sigma_Z^2 = -\exp(-S)\int_Z^\infty \nu K_Z \exp(S) dZ$$

(see Equation 50 of Kuijken and Gilmore 1989b), where ν is the density profile of the tracer population and $S(R, Z)$ represents the effect of the RZ velocity dispersion

(i.e., the tilt term). Kuijken and Gilmore (1989b) proposed that the way to solve this integral equation is by assuming a functional form of the Galactic potential, K_Z, and then fitting the vertical velocity dispersion. Here we applied the same proposed method and assumptions, including the tilt term, to each of our thin and thick disk datasets separately. The results are presented in Figure 3.10. Note that the assumed analytical form of Galactic potential in Kuijken and Gilmore (1989b), which consists of one disk and a constant volumetric dark matter density, produces a good fit to the observed velocity dispersions of both the thin and thick disk. However the best fit values of the dark matter density are vastly different, with the thick disk value only 1/10 that of the thin disk value, far from the "consensus" dark matter density at solar position of roughly 0.01 $M_\odot$ pc^{-3}. Whereas our attempts above at using the differential approach can only produce a dark matter density close to this canonical value using the thick disk population, the integral equation produces the opposite result — i.e., the thin disk data giving closer to consensus dark matter density.

We also tried this integral approach using a K_Z profile with *two* disk components (one having a 0.3 kpc scaleheight and one a 0.9 kpc scaleheight); however, this produces negative total disk densities, which is clearly not physical.

3.5.4 Non-Equilibrium and Time Dependence

In this study we assumed that the stellar populations are in dynamical equilibrium, so that we can neglect the partial time derivatives in our theoretical framework, as is commonly done in these types of analyses (e.g., Moni Bidin et al. 2012; Moni Bidin et al. 2015; Bovy and Tremaine 2012; Hagen and Helmi 2018). While the assumption of a steady state Galaxy could be valid for a kinematically hot population

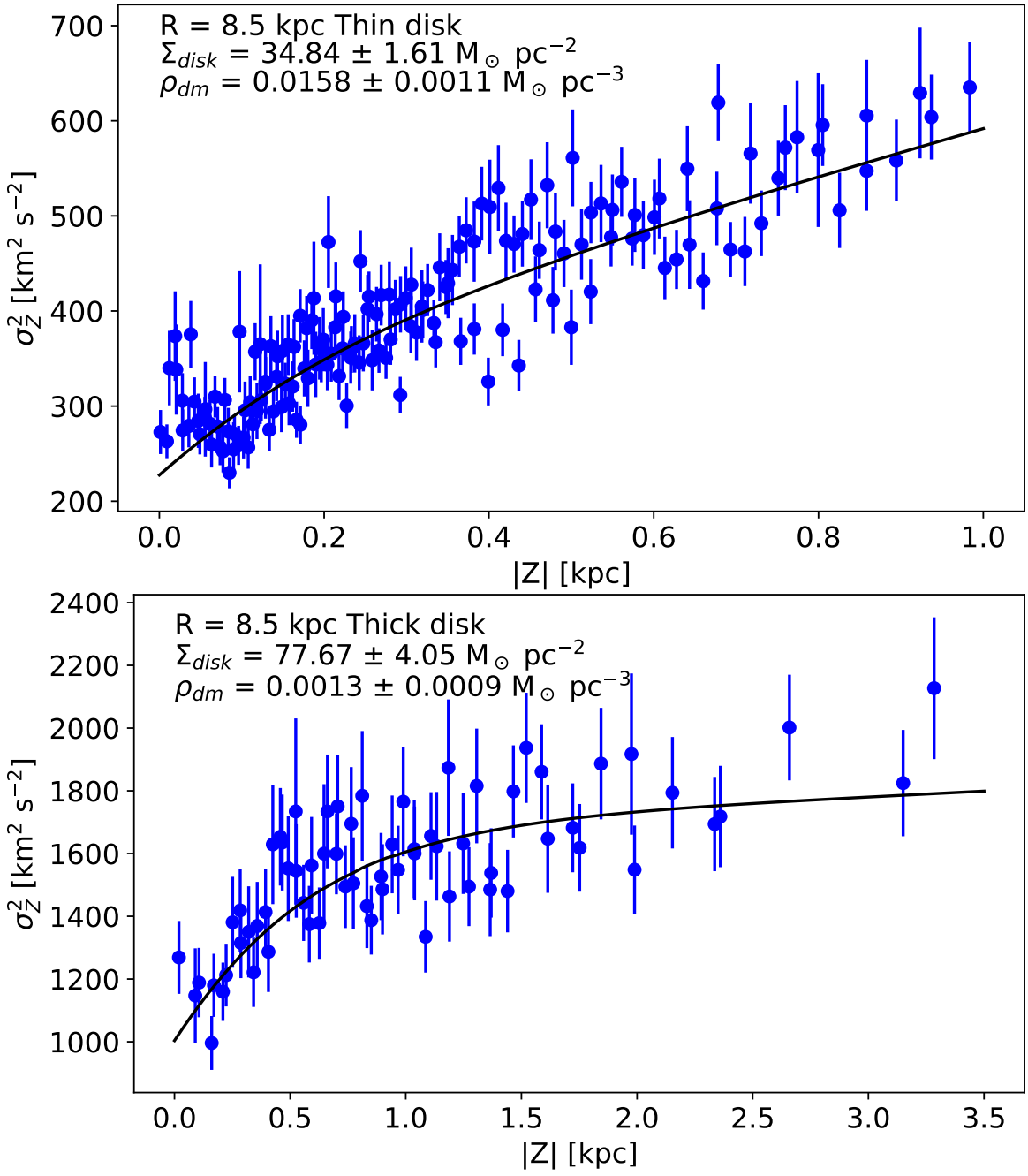

Figure 3.10: Calculated surface density using the integral equation approach proposed by Kuijken and Gilmore (1989b). While the assumed disk and dark matter model produce relatively good fits of the thin and thick disk velocity dispersions, the best fit dark matter density has an order of magnitude difference between thin and thick disk (see values in the legends), with the thin disk result coming closer to the canonical dark matter density near the Sun.

dominated like the thick disk, stars in the colder thin disk are more susceptible to both small and large dynamical perturbations, as is suggested by Shaviv et al. (2014). While application of the Jeans Equation may be entirely appropriate for a thick disk in dynamical equilibrium and more resilient to perturbations, the Jean Equation may well be responsible for spurious results to a thin disk responding to such things as spiral density waves (Siebert et al. 2012), a precessing warp (Cheng et al. 2020), satellite accretions, and bars. These factors may explain why at the same vertical height, the chemically separated thin and thick disks in the inner galaxy give very different surface density measurements, and why, regardless of radius, the two measured surface densities do not agree with each other until $Z \sim 1$ kpc (Fig. 3.7). The existence of the Galactic bar alone has significant impact on stellar kinematics and dynamics (De Propris et al. 2011; Aumer and Schönrich 2015; Palicio et al. 2018) and is obviously a time-dependent phenomenon, in direct contradiction to the steady state assumption. This effect is likely responsible for the increasing discrepancy between the thin and thick disk results towards the inner Galaxy (Fig. 3.7).

We have looked for evidence for disequilibrium in our own dataset. For example, we explored for variations in the trend for by looking for differences in surface density distribution for stars at different Galactic longitudes at solar radius. We found no significant differences within the uncertainties of the data. Nevertheless there have been discussions of such disequilibrium in the solar neighborhood: for example, as manifested in a phase spiral (Antoja et al. 2018), although it seems such features are short-lived (Tremaine et al. 2023).

3.5.5 Dark Disk

In the previous sections we have compared our measured results against predictions of the SHM. The SHM has withstood many tests and has generally proven to be viable in many contexts (Klypin et al. 2002; Weber and de Boer 2010; Bovy and Tremaine 2012; Okabe et al. 2013). However, it is worth considering whether the SHM itself may need modification to improve its ability to describe the Milky Way potential.

There have been several recent studies that suggest the NFW profile is not adequate in describing the Galactic dark matter density distribution (Law et al. 2009; Nitschai et al. 2021). For example, some N-body show massive satellite accretion onto early galactic disks can lead to the deposition of dark matter in disk-like configurations that co-rotate with the galaxy. Thick, thin and dark disks occur naturally within a ΛCDM cosmology (Lake 1989; Read et al. 2008; Purcell et al. 2009; Widmark et al. 2021). Read et al. (2008) found that low-inclination mergers give rise to a thick disk of dark matter that is co-rotating with the Milky Way stellar disk and morphologically resembles a stellar thick disk, but with longer scale length and height. Following this idea, Purcell et al. (2009) argued that within the context of the accreted dark disk scenario, it is likely that the dark disk of the MW contributes 10-20% to the total local dark matter density. Near the Sun, Purcell et al. (2009) concluded that the co-rotating dark matter fraction is enhanced by about 30% or less compared to the SHM. Our results in Figure 3.7 and Figure 3.8 show, if all assumptions built into that analysis hold, that the total surface mass density derived from the thick disk is clearly enhanced with respect to the SHM. This effect is more prominent close to the midplane ($Z < 0.3$ kpc) and in the inner Galaxy ($R < 8$ kpc). The total surface mass density estimated here is ∼1.3 times larger than that predicted from the model. We speculate that this discrepancy is a possible effect of the dark disk predicted in

cosmological simulations, but never previously inferred for the MW.

Unfortunately, for the thin disk population we find that the total mass density for the inner Galaxy and close to the midplane with a vertical height smaller than 0.3 kpc is systematically *smaller* than the SHM prediction (top panel Figure 3.8). Once again, the discrepancy between predictions from the thin and thick disk stars make it difficult to infer any strong conclusions regarding the dark mater distribution.

3.6 Conclusions

By leveraging high-resolution astrometry from Gaia DR3 and high-resolution stellar spectroscopic information from APOGEE, we present the most detailed measuring of surface density across a large range of Galactocentric radius and vertical height. We find that the measured surface mass density is highly dependent on the assumptions made in its calculation, and that while the most common combination of assumptions used in previous similar studies — i.e., a linear trend of velocity dispersion with vertical height and exponentially distributed disks — generally gives physically plausible and trustworthy results that match the SHM when applied to the thick disk population beyond 1 kpc in vertical height at the solar circle, the results obtained using (1) thin disk stars, (2) stars near the mid-plane from any population, and (3) stars in the inner and outer Galaxy give surface mass densities that depart, sometimes radically, from the SHM. In addition, we find statistically significant ripples in all three dimensions of velocity dispersion for both thin and thick disk stars across a wide range of Galactocentric radii and vertical height.

With larger datasets comes a need for more complex models. We fear that our new knowledge of the complexities of the stellar kinematics and spatial distributions of

stars in the Milky Way is at the point where it may no longer be defensible to apply simple analytical approaches — like those used in most previous dark matter density measurement studies as well as attempted in the present analysis — to the study of the mass density profile of the Milky Way. Instead, in the midst of exponentially increasing volumes of precision data that are the rewards of astronomical progress, the concurrent revolution in numerical simulation of Milky Way like galaxies needs to be brought to bear on this problem.

Chapter 4

Kinematical Analysis of Substructure in the Southern Periphery of the Large Magellanic Cloud

This chapter was originally published as Cheng et al. (2024).

4.1 Introduction

As the closest interacting pair of dwarf galaxies, the Large and Small Magellanic Clouds (LMC and SMC) are excellent laboratories for exploring dwarf galaxies and their interaction in detail. Consequently, the Clouds have been the targets of many dedicated observational campaigns. In particular, recent large and contiguous imaging surveys have accelerated discoveries of low surface brightness stellar substructures around the Magellanic periphery (e.g., Mackey et al. 2016; Pieres et al. 2017; Mackey et al. 2018; Belokurov and Erkal 2019; Martínez-Delgado et al. 2019; Gaia Collaboration et al. 2021a), made possible by virtue of, for example, Gaia (Gaia Collaboration et al. 2016a), the DECam/Blanco surveys (e.g., The Dark Energy Survey Collabora-

tion 2005; Nidever et al. 2017; Drlica-Wagner et al. 2021), and work with the VISTA facility (e.g., Cioni et al. 2011; El Youssoufi et al. 2021).

These outlying stellar substructures in the Magellanic periphery are sensitive probes for deciphering the tidal interaction histories between the LMC and SMC and between the Clouds and the Milky Way (MW) because the shallower potentials in galactic peripheries make stars there more easily disturbed. Thus, identifying low surface brightness stellar substructures in the LMC and SMC outskirts and measuring their key properties is essential for understanding their dynamics. While some studies of the morphology and stellar populations of these faint structures have been conducted (e.g., Mackey et al. 2018; Martínez-Delgado et al. 2019; El Youssoufi et al. 2021), the detailed 3D kinematics for those structures remain largely unexplored.

One of the prominent stellar substructures around the LMC is an arm-like feature in the northern periphery (Mackey et al. 2016). Cullinane et al. (2022) showed that the stellar metallicity and kinematics of this northern arm are consistent with those of the outer LMC disk and attributed the formation of the northern arm to the MW tide. Given that many of the stellar structures in the main body of the LMC are found to be asymmetric — for example, a one-armed spiral and an off-centered bar (de Vaucouleurs and Freeman 1972), as well as two stellar warps seen only in the southwest part of the disk (Olsen and Salyk 2002; Choi et al. 2018) — it is important to determine whether the northern arm is yet another asymmetric feature of the LMC or if it has a still-unidentified counterpart in the southern periphery. If a counterpart indeed exists, it would place constraints on formation mechanisms for these particular features, which, in turn, are a key to deciphering the LMC's interaction histories with the SMC and MW.

Recently, a candidate counterpart of the northern arm was discovered in the south-

ern periphery by Belokurov and Erkal (2019). Based on N-body simulations of the Magellanic Clouds that included the MW potential, they suggested that the southern structure is likely a spiral arm created by the most recent interaction with the SMC and consisting of pulled-out LMC disk stars. These authors further suggest that the stellar motions in the southern structure retain the kinematic signature of the outer LMC disk. Their assessment, however, was based on 2D proper motion measurements, not the full 3D velocity information that is essential to making confident conclusions regarding the origin of these stars.

Another prominent stellar substructure in the southern part of the LMC periphery are two large "hook"-like features, discovered by Mackey et al. (2018) and designated as "Substructure 1" and Substructure 2" in their paper. These "hook"-like features reside to the south of the LMC's main disk at $\sim$10° from the LMC center, with $\sim$40–45° separation in position angle between them (see Figure 4.1c). Based on a comparison of the relative color-magnitude diagram (CMD) positions of the red clump and main-sequence turnoff stars in these regions, Mackey et al. (2018) concluded that the distances to the "hook"-like features are not significantly different from those of the stars in both the northern and southern peripheries. Mackey et al. also suggest a physical association between "Substructure 2" and the RR Lyrae Bridge (Belokurov et al. 2017) connecting the LMC and SMC. However, no kinematical studies have been conducted on these substructures to date.

In this study, we explore the kinematics of stellar substructures around the LMC, with particular focus on the southern periphery, including "Substructure 1" and "Substructure 2" (i.e., two "hook"-like features). We make use of the improved uncertainties in proper motion measurements from *Gaia* Early Data Release 3 (EDR3; Gaia Collaboration et al. 2016a; Gaia Collaboration et al. 2021b) and new radial velocity

measurements from APOGEE spectra. We are guided in our interpretation of these features by a model of LMC rotation that we have developed, as well as various N-body simulations Besla et al. (2012) of the dynamical history and past interaction of the LMC and SMC, which produce a variety of perturbations and tidal debris from either or both of the Clouds, depending on starting assumptions. The APOGEE spectra also allow us to investigate the added dimension of the stellar metallicity distributions of these substructures, further clues to their origin. A companion exploration (Muñoz et al. 2023) with these same spectroscopic data will focus on the detailed chemical aspects of these substructures to further constrain the properties and origin of the stellar substructures in the southern periphery.

This paper is organized as follows: In Section 4.2, we describe the MC star samples used in this study. In Section 4.3, we present the 2D and 3D stellar motions for stars using only Gaia proper motions (PMs) and Gaia PMs plus APOGEE radial velocities, respectively. We particularly focus on a kinematically distinct group of stars that lie around, but are not limited to, the southern structures discovered by Belokurov and Erkal (2019). We then present comparisons with hydrodynamical simulations of an LMC-SMC analog pair of galaxies to explore plausible explanations for those kinematically distinct stars in the southern periphery. In Section 4.4, we discuss the possible origin of these newfound MC stellar substructures and summarize our conclusions.

4.2 Data

Our analysis relies on data from *Gaia* EDR3 (Gaia Collaboration et al. 2021b), from which we draw LMC stars via a selection procedure similar to that applied

by Belokurov and Erkal (2019), but with some slightly different criteria: Stars with $G < 17.5$ are selected within 30° of the origin of the Magellanic Stream ($\alpha = 80.8926°$, $\delta = -72.1859°$) coordinate system (Nidever et al. 2008). We adopted the extinction map from Schlafly and Finkbeiner (2011), and an extinction correction is performed with the equation and parameters from Gaia Collaboration et al. (2018c). Then we make a selection within the color-magnitude diagram to constrain our sample to stars primarily along the red giant branch (RGB) of the LMC (Figure 4.1a). To eliminate most of the foreground stars from the Milky Way, those with parallax $\varpi > 0.2$ mas or Galactic latitude $|b| < 5°$ are removed, while an additional selection for stars with similar proper motion to the LMC is applied (Figure 4.1b; in this figure, proper motions are shown in Magellanic Stream coordinate system, and the large and small "blobs" represent stars from the LMC and SMC, respectively.) The spatial distribution of our selected LMC star sample is shown in Figure 4.1c. In Mackey et al. (2018), two substructures to the south of LMC have been identified as regions of stellar overdensity; for ease of comparison, these substructures are labeled in Figure 4.1c and subsequent figures as Substructure 1 and Substructure 2. Similarly, structures identified by Belokurov and Erkal (2019) are labeled with black dotted line in all relevant figures. Furthermore, we excluded stars within 7 degrees from the center of SMC (red dotted line, SMC Exclusion Zone) from all analysis, but we decide to include these stars within our figures for easy comparison.

To investigate the kinematics of substructure at the southern periphery of the LMC further, we employed stars from APOGEE (Majewski et al. 2017; Wilson et al. 2019; García Pérez et al. 2016; Holtzman et al. 2015; Nidever et al. 2015; Zasowski et al. 2017) Data Release 17 (DR17), part of the Sloan Digital Sky Survey (SDSS-IV) (Gunn et al. 2006; Blanton et al. 2017), where precise line-of-sight velocities enable the

derivation of the three-dimensional motions of stars. We focus here on six APOGEE fields placed on and around previously known substructures: two to the North of LMC on the arm feature discovered by Belokurov and Erkal (2019) and four to the South of LMC on the hook features and their extensions discovered by Mackey et al. (2018); data on these fields were obtained through the Chilean National Telescope Allocation Committee (CNTAC) program CN2019A-30 (PI: A. Monachesi). These fields are shown in Figure 4.1c with circles of different colors that, in some following figures, will be used to identify the stars in each field. We applied the same parallax, color-magnitude diagram, and proper motion selections with our *Gaia* sample to the stars within the six APOGEE fields. Additional selection criteria in line-of-sight velocity ($100 < V_{helio} < 350$ km s^{-1}), effective temperature ($T_{eff} < 5400$ K) and surface gravity ($\log g < 4$) are applied to refine our LMC sample further. A total 88 stars across all 6 fields passed through all selection criteria.

4.3 Results

4.3.1 2D motion from Gaia EDR3

In Figure 4.2 we show the spatially averaged proper motion components in Magellanic Stream coordinates of the *Gaia* sample as observed (top panels), as well as the residuals of those proper motions after subtracting the predicted values from a fitted model (bottom panels), which we describe further below. The dipole pattern seen in the main LMC disk in the upper panels steems from the disk's rotation, while distinct kinematical signatures of previously discovered features, such as the arm-like substructure to the north of the LMC (Mackey et al. 2016) and the hook-like feature

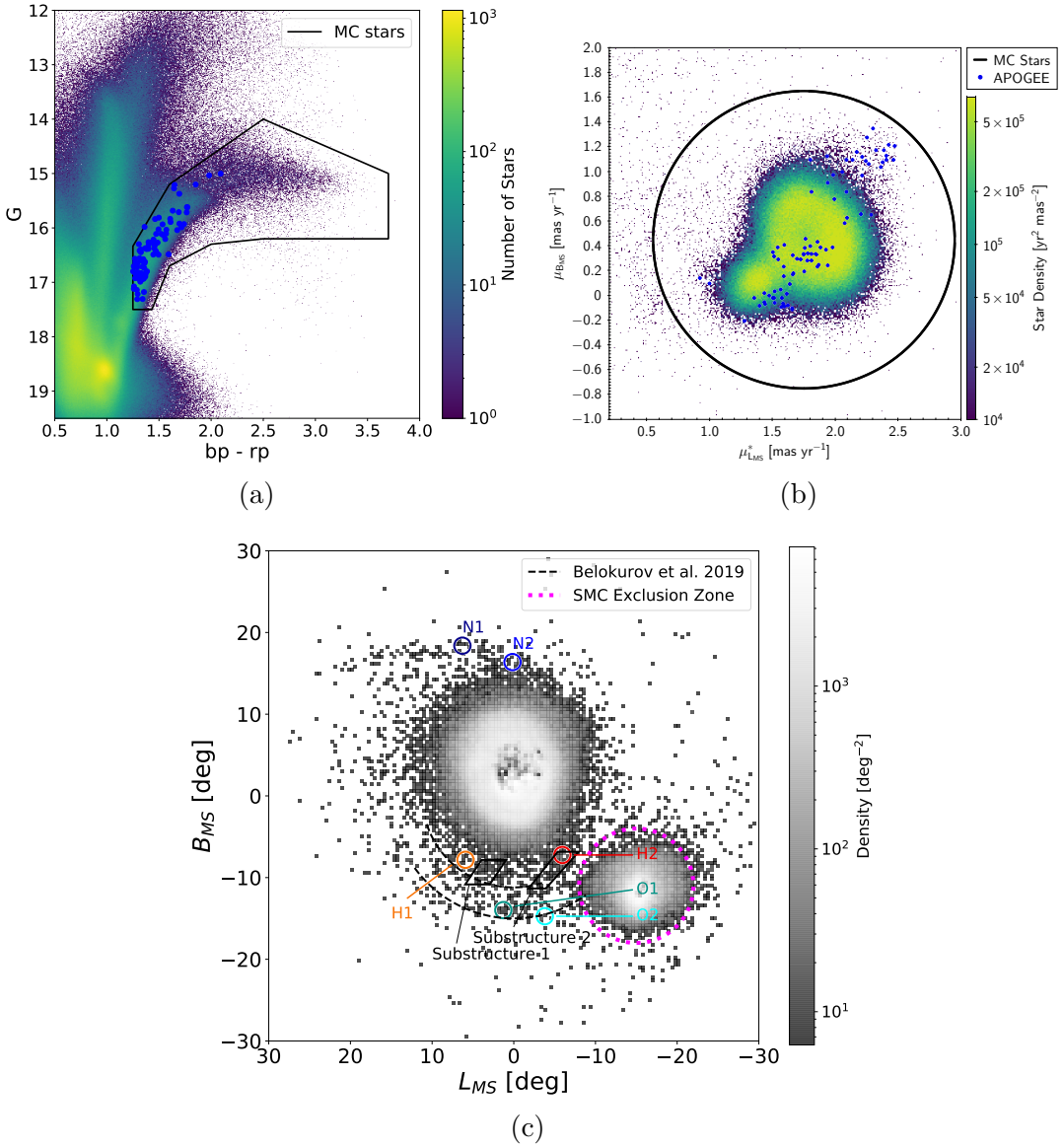

Figure 4.1: The steps to creating our survey sample. (a) The CMD of all *Gaia* stars within 30° of the origin of the Magellanic Stream coordinate system. The black lines indicate the CMD region showing our initial selection of LMC stars. APOGEE stars are indicated with blue dots. (b) Proper motions in Magellanic Stream coordinates and our proper motion selection criteria. The black lines indicate the regions within which we retain stars in our sample. (c) On-sky distribution of our selected LMC star sample in Magellanic Stream coordinates (L_{MS}, B_{MS}). The locations of APOGEE fields are indicated with circles of different colors. Substructures identified in Mackey et al. (2018) are identified and labelled within solid black lines, and substructures (arms) identified in Belokurov and Erkal (2019) are labelled with dotted black lines.

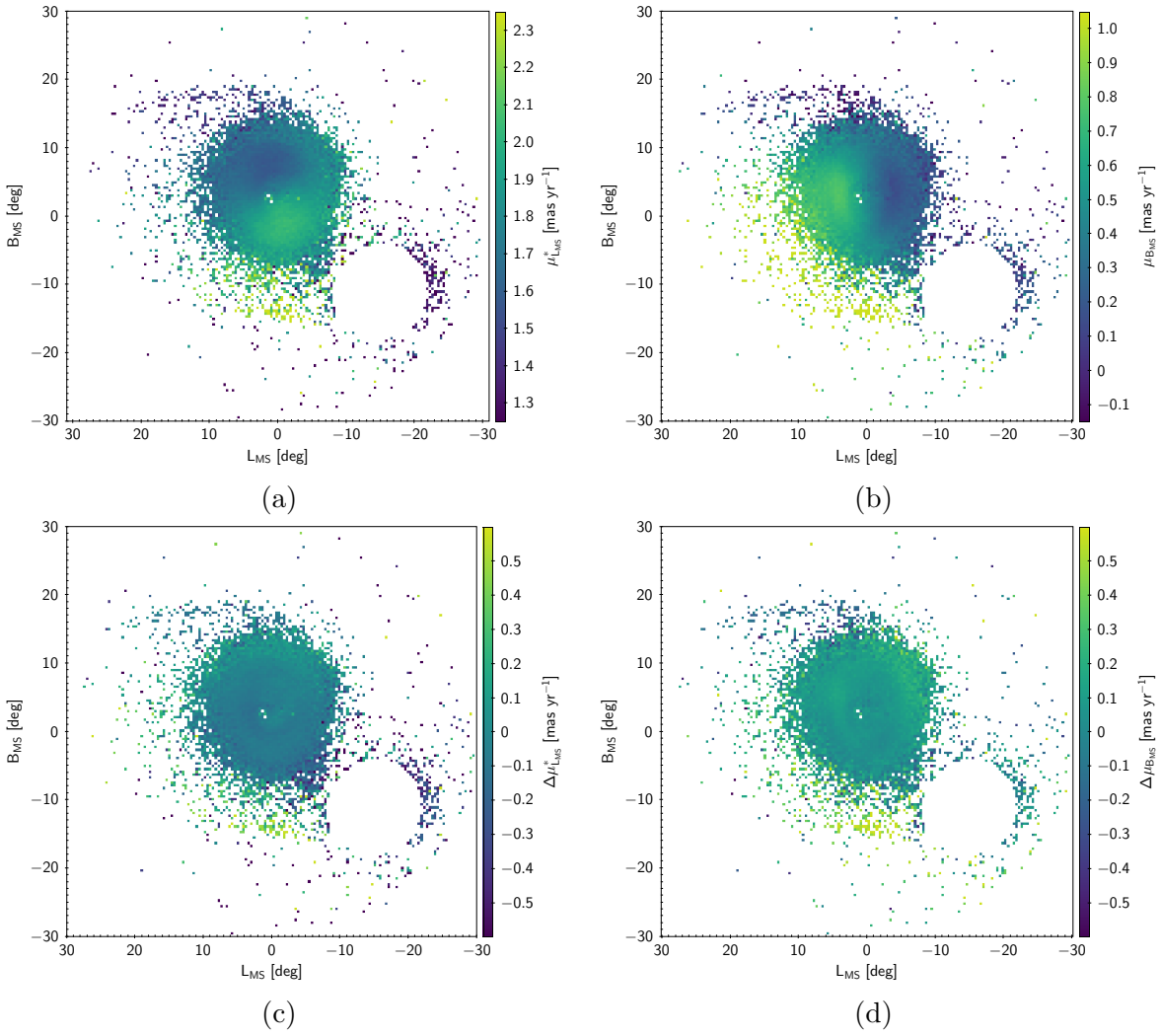

Figure 4.2: The observed proper motion distribution of the LMC star sample in Magellanic Stream coordinates (panels a and b). The reported longitudinal proper motion, $\mu^*_{L_{MS}}$, has the $\cos(B)$ correction applied. In panels (c) and (d) the observed proper motions are differenced against those predicted in the LMC kinematic model ($\Delta\mu = \mu_{obs} - \mu_{model}$, see Section 4.3.1).

lying in between the LMC and SMC ("Substructure 2" in Mackey et al. 2018), are revealed around the LMC periphery. The residual maps in the lower panels show that our kinematical model fits the disk rotation well, whereas the features on the periphery exhibit strong departures in proper motion from our simple model of a rotating disk. In particular, as previously found by Mackey et al., while the substructure to the north features low proper motions, stars in the hook in the south have a much larger proper motion than stars in the immediately surrounding area. In addition, in the southern part of the LMC, at radii extending beyond about 10 degrees from LMC center and starting near the end of the hook and wrapping clockwise around the LMC to about $(L_{MS},\ B_{MS}) = (10^{\circ},\ -5^{\circ})$, there is a swath of stars that shows higher proper motions in both the longitudinal and latitudinal dimensions.

To explore these kinematical structures of the LMC periphery further, we contrast the observed motions against those from a kinematical model of the LMC that includes the effects of bulk center-of-mass motion and internal rotation, as described in (Choi et al. 2022). This model is based on fits to $\sim 10^4$ LMC disk stars with both proper motion measurements from *Gaia* EDR3 (Gaia Collaboration et al. 2021b) and line-of-sight velocity measurements from a variety of sources, including Hydra-CTIO observations of 4226 stars by Olsen et al. (2011) and 5386 stars from SDSS DR16/APOGEE-2 (Ahumada et al. 2020). In brief, the modeling procedure, which is based on the formalism of van der Marel et al. (2002), fits several parameters jointly to the proper motion and line-of-sight velocity data. These parameters include the location of the LMC's kinematical center in RA and Dec, the LMC's bulk transverse motion along the RA and Dec axes, the line-of-sight velocity of the kinematical center, the position angle of the line of nodes, the inclination of the disk, two parameters describing the shape and amplitude of an internal rotation curve that is flat after a scale radius

R_0, and the velocity dispersion in three orthogonal directions. We assume that the LMC disk has no precession or nutation and that the distance to the LMC is 50.1 kpc (Freedman et al. 2001). The model predicts the proper motion distribution well within the inner disk of the LMC, but does significantly deviate from the observations at larger radii (Choi et al. 2022), and (as expected) fits especially poorly to stars in the periphery of the SMC.

To probe the possible origins of the previously discussed features more deeply, we use the model fit as described above to deproject the proper motions into in-plane velocity, V_{int}, as shown in Figure 4.3a. To derive an expression for V_{int}, we use the coordinate system and formalism developed by van der Marel et al. (2002), in particular: (1) their Equation 7, which describes the relationship between the proper motion vector and the orthogonal velocity components v_2 and v_3 in the plane of the sky (as defined in Equation 1 of van der Marel et al. 2002, the direction of v_2 is parallel to radius vector originating at the LMC center and ending at the sky coordinate in question, while v_3 is orthogonal to this in the direction of the position angle Φ), and (2) their Equation 21, which describes the projection of the rotation curve to v_2 and v_3. The distances to the individual stars assume that they are moving in the inclined plane of the LMC disk, and as such depend on the distance to the center of mass of the LMC and on the disk inclination. We adopted 18.5 as the LMC distance modulus (which is within 1% of the measurement by Pietrzyński et al. 2019 from eclipsing binaries) and derived the inclination from the model fit, which we found to be 22.7 deg, in close agreement with that derived from red clump distances by Choi et al. (2018). We use the observed proper motion vector, after subtracting the contribution from center of mass motion, to compute $v_{2,int}$ and $v_{3,int}$, and then derive an expression for the rotation velocity V_{int} as a function of the magnitude of the velocity vector in the

plane of the sky:

$$V_{int} = s\frac{(v_{2,int}^2 + v_{3,int}^2)^{\frac{1}{2}}}{[(f_1/f_2)^2 \sin^2(i)\cos^2(\Phi - \Theta) + f_2^2]^{\frac{1}{2}}} \tag{4.1}$$

where

$$f_1 = \cos(i)\sin(\rho) + \sin(i)\cos(\rho)\sin(\Phi - \Theta)$$

and

$$f_2 = [\cos^2(i)\cos^2(\Phi - \Theta) + \sin^2(\Phi - \Theta)]^{\frac{1}{2}}$$

are terms in the geometric projection and $s = \pm 1$ is the direction of orbital motion of the given star (s=+1 in the direction of spin of the LMC disk), i is the inclination of the LMC disk to the plane of the sky, ρ is the radius coordinate expressed as angle on the sky, Φ is the position angle measured east of north, and Θ is the position angle of the line of nodes. To determine s, we compute the angle of the proper motion vector Θ_t and compare it to the position angle Φ, and set $s = -1$ if $90 < (\Phi - \Theta_t) < 270$ and $s = +1$ otherwise.

The resulting deprojection shows *roughly* the ordered rotational velocity in the inner $\sim 10^\circ$ of the LMC. We refer to (Choi et al. 2022) for the detailed discussion about the stellar kinematics in the inner disk of the LMC. Beyond 8–10° from LMC center, on the other hand, the stars show a remarkable spread in V_{int} values, as shown by the color scale markings of stars in Figure 4.3a, with many of the various substructures discussed earlier showing markedly distinct, and even extreme, V_{int} values. Meanwhile, stars in the region associated with "Substructure 1" have V_{int} somewhat elevated above that for stars in the outer disk, whereas stars in the region associated with "Substructure 2" have very low, even negative V_{int} relative to the outer disk.

To demonstrate the dramatic change in the kinematical character of stars just beyond a radius of ∼10° in the southern LMC periphery, Figure 4.3b compares the distribution of V_{int} values for stars within 8° of the LMC center to those within the "southeast periphery sector (SPS)" outlined in Figure 4.3a and spanning radii of 10-20°. As stated before, stars within the SMC Exclusion Zone (red dotted line) are not included in the SPS. Figure 4.3b also includes as a control sample those stars in a similar range of radius but spanning the entire northern LMC periphery (the "northern periphery sector (NPS)").

As may be seen in Figure 4.3b, the SPS stars span a vastly broader range (∼600 km s^{-1}) in V_{int} than either the stars in the inner, disk-dominated region or in the NPS, which looks very much like the inner disk in terms of V_{int} distribution. While some SPS stars share the nominal V_{int} velocities of disk stars, the former are generally confined to SPS stars at smaller radius, as is evident in Figure 4.3a. On the other hand, a larger fraction of SPS stars have velocities with *more extreme* V_{int} — either much higher than the nominal LMC disk, or retrograde. Neither of these types of V_{int} are what is expected for the outermost parts of disks, where galaxy mass is typically distributed so that rotational velocity decreases with radius (but remains prograde). Moreover, given that V_{int} represents a 2-D, deprojected velocity to the LMC disk plane, not only does Figure 4.3b demonstrate just how "non-disk-like" are the motions of a large fraction of SPS stars, but it suggests that the full 3-D motions of some SPS may be even more distinct and extreme. That assessment is borne out by the stars in hand for which full 3-D motions are possible due to the availability of APOGEE radial velocities (RVs).

In Section 6 of Gaia Collaboration et al. (2021a), a similar kinematical study of LMC outskirts is also reported. The authors pointed out that both the northern (north-

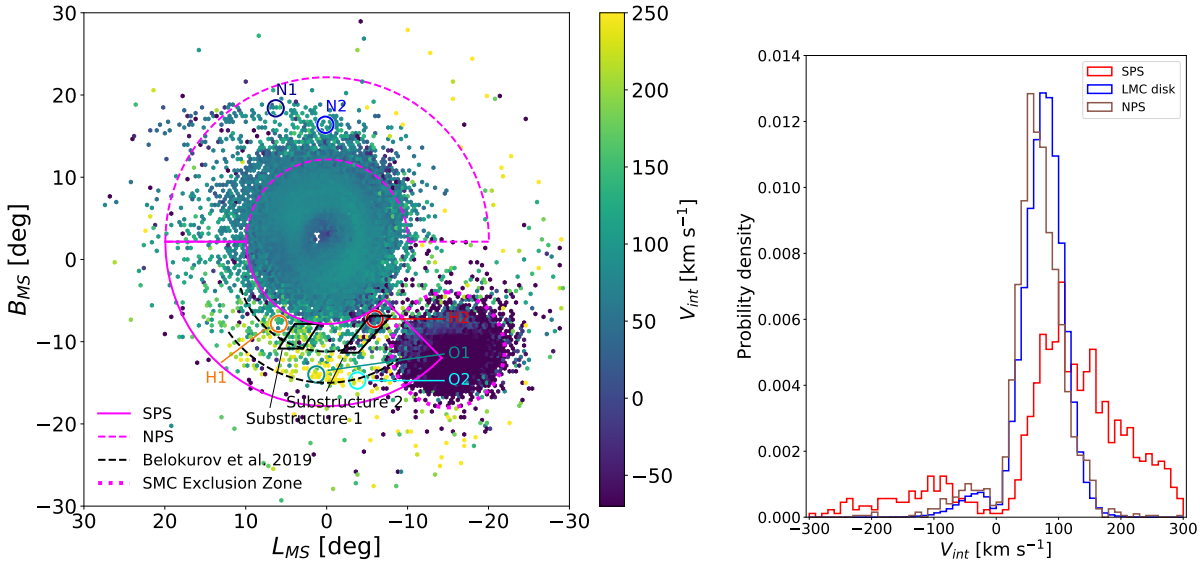

(a) (b)

Figure 4.3: In-plane velocity distributions for our selected LMC star sample. (a) The in-plane velocity distribution, V_{int} in Magellanic Stream coordinates (L_{MS}, B_{MS}). Some previously identified substructures are indicated, as is the placement of the APOGEE-2 fields and the southern periphery sector (SPS) analyzed separately. A northern periphery sector (NPS) is placed to the north of LMC, with the same inner and outer radius as SPS. (b) A comparison of the V_{int}, in-plane velocity distributions for stars in the nominal disk of the LMC (radii less than 8° from LMC center, blue curve), stars in NPS region (brown curve) to those in the SPS region.

ern tidal arm, NTA, in their paper) and southern substructure (southern tidal arm, STA, in their paper) have consistent velocities to those of LMC, and an additional substructure is detected to the east of LMC (ESS in their paper). While we agree that the northern substructure has consistent velocity distribution with those of the outer LMC disk, the southern substructure shows significant differences in velocity, especially an increase in stars with high in-plane velocities that is not present in the northern periphery region, and only a slightly larger velocity is detected to the east of LMC, which could be interpreted as an extension of the southern substructures.

4.3.2 3D Motions and Metallicities for APOGEE Stars

By combining APOGEE DR17 RVs with *Gaia* proper motions, full three-dimensional (3-D) motions can be calculated. We use the same orientation of the LMC disk (i.e., line-of-nodes and inclination angle) as used in the model to calculate V_{int} in Section 4.3.1 to transform those 3-D motions into a cylindrical coordinate system appropriate to the LMC disk reference frame, where V_R and V_ϕ are the radial and rotational motions projected onto the LMC disk plane and V_Z is the motion perpendicular to the disk plane (where a positive V_Z is towards the Sun). To perform this transformation, we first inverted Equation (5) from van der Marel et al. (2002) to solve for v'_x, v'_y, and v'_z in the plane of LMC disk, computed the in-plane positions x' and y' using Equation (7) from van der Marel and Cioni (2001), and then computed V_R, V_ϕ, and V_Z as:

$$V_R = (x'v'_x + y'v'_y)/R,$$

$$V_\phi = (y'v'_x - x'v'_y)/R,$$

$$V_Z = v'_z.$$

Figure 4.4 shows the velocity distributions in this parameter space for each of the six individual APOGEE fields shown in Figure 4.1c, along with stars from the LMC disk. This LMC disk sample is the same as in Nidever et al. (2020). The latter stars define clear concentrations in velocity space. It is immediately obvious that the stars in the O1 and O2 APOGEE fields have velocities very different from those of LMC disk stars, with strong (by more than 100 km s^{-1}), "infalling" radial motion and typically a faster V_ϕ (i.e., azimuthal) motion than that of LMC disk stars. In the case of the

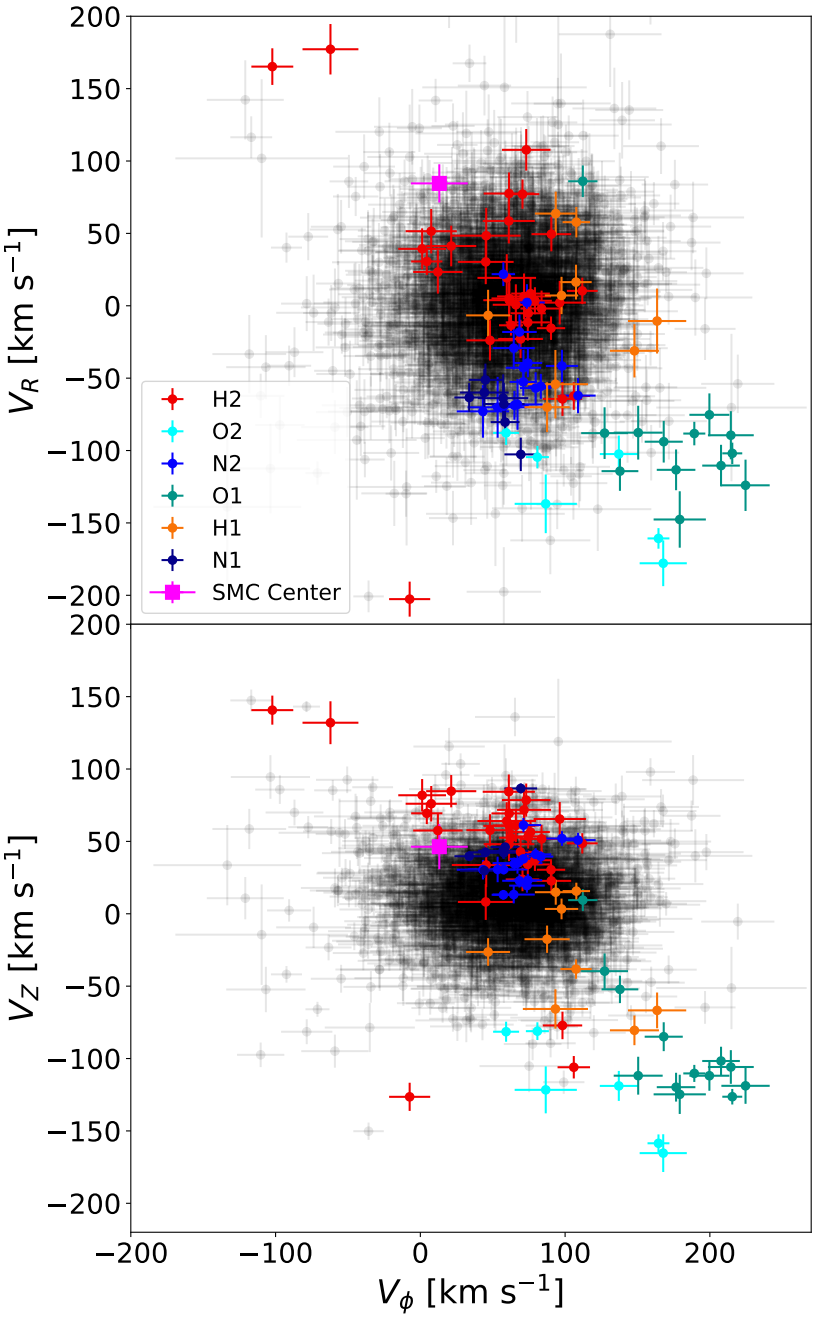

Figure 4.4: The vertical velocity (V_Z) and radial velocity (V_R) versus azimuthal velocity (V_ϕ) of APOGEE DR17 stars, with symbols colored for stars in the six outer LMC fields in the same way as in Figure 4.1c and Figure 4.3a and with LMC disk stars colored in grey as well as the SMC center as a magenta square. The error bars on individual velocities reflect only the measurement uncertainties in line-of-sight velocity and 2D proper motion.

O1 field the V_ϕ motions of some of the stars exceed that of the most rapidly rotating LMC disk stars by of order 100 km s^{-1}. Given these quite different and extreme kinematics, it is difficult to conclude that the stars in the O1 and O2 fields are simple extensions of the LMC disk.

This assessment would seem to be at least partly supported by the spectroscopic metallicities for the stars in the O1 and O2 fields as derived by APOGEE. These are shown by the probability distribution functions derived by kernel density estimation (KDE) in Figure 4.5. As may be seen, the peak of the metallicity distribution function (MDF) for the O2 field is shifted by about 0.6 dex in [Fe/H] from that of the LMC inner disk. Even accounting for the gentle radial metallicity gradient in the LMC disk, the O2 field is still shifted by about 0.2 dex from the MDF of the outermost part of the disk (stars 8-10° from the LMC center, shown as the solid line in Figure 4.5). Indeed, the MDF for the O2 field is similar to, though slightly more metal poor than that of the SMC; however, while the O2 field lies very close to the SMC in the sky, the kinematics of the O2 and SMC stars are so disparate (e.g., separated by some 300 km s^{-1} in the simple V_{int} projection of proper motion; Figure 4.3a) that it would seem to preclude a simple connection of the O2 stars to the SMC.

On the other hand, while the MDF of the O1 stars seems to match well that of the LMC outer disk, their 3-D motions are clearly quite distinct (Figure 4.4). However, all of these MDF comparisons must be considered tentative, given that there are only 13 and 6 stars with APOGEE data in each of the O1 and O2 fields, respectively. The metallicity and detailed chemical abundances of the stars in these six APOGEE fields are explored further in a companion paper by Muñoz et al. (2023).

In contrast to the situation for the O1 and O2 fields, the stars in fields N1, N2, H1 and H2 do lie within the approximate 3-D velocity envelope of the LMC disk stars

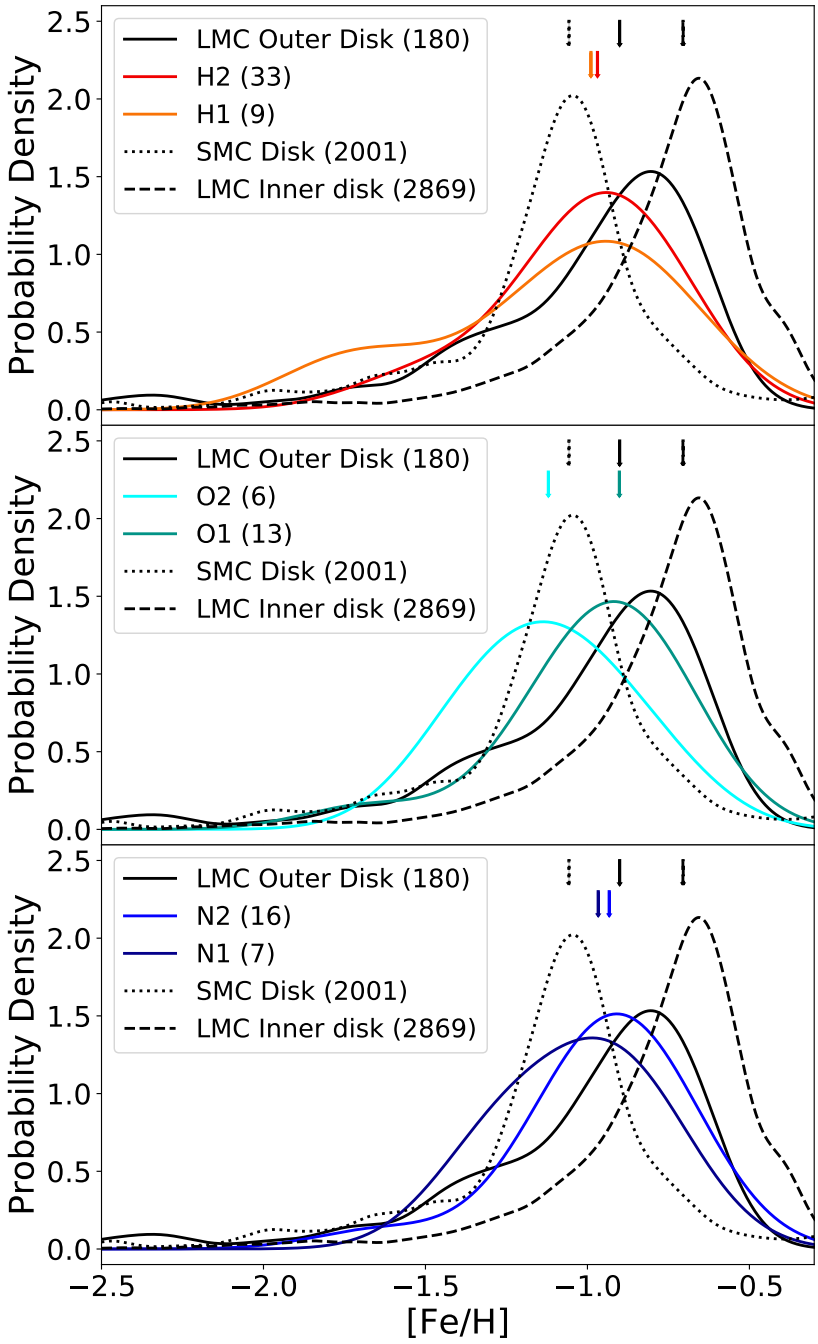

Figure 4.5: Probability density functions derived from KDE applied to the observed metallicities for the LMC inner disk (within 8 deg of the LMC center, black dashed lines), LMC outer disk (further than 8 deg from LMC center, black solid lines), SMC disk (within 7 deg from SMC center), and stars in all six APOGEE fields (same color with Figure 4.3a). The median metallicity of each sample is labelled by the arrow close to the top of the figure. The number of stars within each sample is labelled in the legend of each panel.

(Figure 4.4), albeit generally near the "edge" of the envelope. This suggests a closer connection of the stars in these APOGEE fields to the LMC disk. This association is apparently supported by the MDFs of the various populations, in particular for the N1, N2 and H2 fields, which match well to the MDF of the outer disk. Only the H1 MDF seems less consistent with the others, but this MDF consists of data for only seven stars. It is perhaps not so surprising that the N1 and N2 groups might be associated with the LMC disk, given that they lie right on the apparent spiral arm feature. However, these new APOGEE results suggest a closer connection of the two southern "hook" features to the LMC disk than previously thought. It also points to these two features as being exceptions to the bulk of the stars in the SPS region, which, based on their V_{int} values, seem kinematically distinct from the LMC disk (Section 4.3.1).

4.3.3 Comparison with Simulations

To obtain better insight on the observed extreme in-plane velocities in the SPS region, we investigate the two simulations from Besla et al. (2012) of an interacting pair of LMC and SMC analogs, subject to the MW's gravitational potential under a first infall scenario. In these simulations, the LMC/SMC binary interaction produces tidal features qualitatively similar to what is broadly observed in the Magellanic system, and so are potentially useful for understanding our results on kinematic outliers. There is as of yet no consensus in the field regarding the recent interaction history between the Clouds (e.g., Cullinane et al. 2022). The major difference between the two Besla et al. (2012) simulations is the impact parameter of the most recent encounter ($\sim$100 Myr ago) between the Clouds: Model 1 has an impact parameter of $\sim$20 kpc, with consequently less dramatic effect on the structure of the galaxies, while Model

2 has an impact parameter of ∼2 kpc, with substantially more tidal debris at large distance from the parent bodies.

To make our comparisons, we translate the 6D phase space information of the simulated LMC/SMC stellar particles to the observed frame. More specifically, we recenter all simulated LMC/SMC particles to match the observed center of mass position and velocity vectors of the LMC, (X, Y, Z) = (-1, -41, -28) kpc and (V_X,V_Y,V_Z) = (-57, -226, 221) km s^{-1} (Kallivayalil et al. 2013). This step is necessary as these simulations were designed such that 3D velocity vector of the LMC matched that measured earlier by Kallivayalil et al. (2006). This shift is applied to the entire simulated Magellanic system and does not change any of the motions of stellar particles internal to each simulated galaxy. We then translate the positions and velocities of each star particle from the Galactocentric coordinate system to α, δ, line-of-sight distance, $\mu_{\alpha*}$, μ_δ, and line-of-sight velocities using the Python library `astropy.coordinates`. We note that we exclude any star particles younger than 1 Gyr old from our analysis, in order to enable comparisons to the observational results based on RGB stars.

We apply the same kinematic modeling procedure to these simulated LMC disk star particles as we did for the data (Section 4.3), which result in fitted parameters for both the bulk center-of-mass motion and internal rotation of the LMC in the two simulations. We then apply these model parameters to all star particles in the simulations, including the SMC particles, returning values for V_{int}, V_R, V_ϕ, and V_Z for all particles with respect to the LMC center-of-mass reference frame.

We note that the inclination and line-of-node position angle of the simulated LMC disk in Model 1 and Model 2 are not an exact match to the observed values with regards to our line of sight (see Section 3.2 in Besla et al. 2016), and that the center of mass position and velocity of the simulated SMC is not exactly matched to the

observed values as described in Besla et al. (2012). However, no corrections are made to the simulated LMC and SMC to make them consistent with these two observed values, as the velocities that we care about are all relative to the LMC center-of-mass reference frame. Thus, the analysis of simulations presented here is only to serve as a proof of concept for the plausible range of kinematics associated with stellar debris tidally removed from the LMC-SMC interactions.

Figure 4.6 presents the kinematic properties of Model 1 (upper panels) and Model 2 (lower panels). We apply the same spatial cuts as described in Section 4.2. Specifically, we define the LMC main disk as the inner 8° from the LMC center, focus on the 10-20° annulus to look for kinematically distinct populations, and exclude the SMC particles within 7° from the SMC center in our analysis. We also exclude those SMC particles that are outside the SMC exclusion zone but within the 10-20° annulus if they have proper motions inconsistent with the majority of the LMC particles. Due to the inconsistent line-of-node position angles of the simulated LMC disks with that of the observed disk, we analyze the 10-20° annulus as a whole instead of dividing the annulus into two sectors as we did for the observation (North vs. South sectors).

From the V_{int} distribution of all the LMC/SMC star particles within the 10-20° annulus (except for the SMC particles inside the SMC exclusion zone), we identify kinematic outlier stars as those that have V_{int} below the 0.15 percentile value (low V_{int} stars) or above the 99.85 percentile value (high V_{int} stars). This is equivalent to 3-sigma outlier selection for the case of a normal distribution. We mark the low/high V_{int} values for Model 1 (-143/185 km s^{-1}) and Model 2 (-226/251 km s^{-1}) in the upper and lower right panels, respectively. The mass fraction of kinematic outlier stars in the 10-20° annulus relative to the stars in the LMC main disk is ∼0.0043% in both Model 1 and 2. If we do the same outlier selection for the observational data,

the computed low and high V_{int} values are -254 km s^{-1} and 319 km s^{-1}, respectively. Model 2, which has a closer LMC/SMC impact parameter than Model 1, shows a better agreement with the observation in terms of the low and high V_{int} values. However, even Model 2 cannot reach V_{int} values as high as those observed, indicating that a stronger tidal perturbation might be needed to reproduce the extreme velocity stars seen in the observation. The number fraction (which is a proxy for mass fraction by virtue of the fact that RGB stars have similar masses) of the kinematic outliers among the Gaia-selected RGB stars relative to the those within the inner 8° is ∼0.0045%, which might be considered a rough upper limit because the RGB selection is likely not 100% complete in the innermost region due to crowding (Gaia Collaboration et al. 2021a). However, it is notable that the simulations contain roughly the same fraction of kinematic outliers as the observations.

The upper and lower left panels in Figure 4.6 show the spatial distribution of kinematic outlier star particles on the 2D star count maps of the simulated LMC from Model 1 and Model 2, respectively. The two solid black circles denote the radii of 10° and 20° from the LMC center, while the blue dashed circle marks the radius of 8° from the LMC center. The green dashed line shows the SMC exclusion zone. The population consisting of the kinematic outliers in the 10-20° annulus for each model is different. In Model 1, most of the high V_{int} stars in the annulus have an LMC origin, while the low V_{int} stars have both LMC and SMC origin. In Model 2, all the low V_{int} stars in the annulus are SMC debris. In general, all the kinematic outliers in both Model 1 and 2 are found around tidally induced low surface brightness features. However, the detailed spatial distributions of kinematic outliers are different in the two models. Model 1 shows a rough bi-polar distribution, while Model 2 shows a one-sided distribution. In 3D space, the kinematic outliers are mostly extraplanar,

as is clearly seen in the edge-on view of the simulated LMC disks (middle panels). In Model 1, the majority of the outliers with LMC origin are found both above and below the main disk, but within ∼10 kpc. On the other hand, the outliers with SMC origin are located far above or below the main LMC disk. In Model 2, almost all of the kinematic outliers, including the LMC debris, are ∼10-20 kpc above the LMC main disk.

On the recommendation of the anonymous referee to our submitted journal paper, we also examined plots of component velocities V_Z and V_R versus Z for the simulations, and compared features found in them to those selected by V_{int}. We find that our V_{int} selection identifies features that would also be seen as outliers in these plots of component velocity versus Z; the advantage of V_{int} is that we can compute its value for the observations, whereas we have no way to measure Z, and thus must assume that $Z = 0$ for all stars.

In Figure 4.7, we show the V_R, V_ϕ, and V_Z velocity components for the two models. The underlying gray scale shows the velocity distributions of star particles in the LMC disk within 8°. We overplot the kinematical outliers shown in Figure 4.6 using the same color and symbol schemes. Similar to what we see from the stars in the O1 and O2 APOGEE fields (Figure 4.4), the kinematical outliers in the simulations show distinct behaviors from the majority of the star particles in the main disk. It is difficult to make a fair comparison between the observations and the simulations because the O1 and O2 APOGEE fields probe a tiny portion of the 10-20° annulus with a narrow coverage of position angles (∼10° around the position angle of 180°), whereas the kinematical outliers in the simulations are tied to a larger range of position angles. Nevertheless, the amplitudes of offsets in each velocity component from the majority of the LMC disk star particles in the models are comparable to those seen in the

observations.

4.4 Discussion and Conclusion

From our analysis of the 2-D velocities based on *Gaia* proper motions for a large number of stars — from which we derive a deprojected, in-plane velocity, V_{int}, per star — combined with 3-D velocities and metallicities for a smaller collection of stars in new APOGEE fields, we find and conclude the following:

- The periphery of the LMC contains stars from a variety of origins and with a clear north-south dichotomy: The stars in the northern LMC periphery (represented by stars in the NPS region of proper motions and the N1 and N2 APOGEE fields) seem to have ties to the outer LMC disk, based on both their kinematics and MDFs. In contrast, the stars in the southern LMC periphery (represented by those in the SPS region generally) show a more heterogeneous MDF and an especially diverse kinematical character, with the latter exhibiting a remarkably extreme range in velocities, with some stars sharing the motions of the LMC disk, but a significant fraction of stars moving quite unlike the stars in the LMC disk.

- Within the SPS region, the areas represented by the hook-like features previously identified by Mackey et al. (2018) have V_{int} values more like those found in the LMC outer disk, and this kinematical association is supported by the observations of stars in the H1 and H2 fields, which show 3-D velocities and MDFs like those of the outer LMC disk.

- On the other hand, stars at larger radius in the SPS contain stars with more

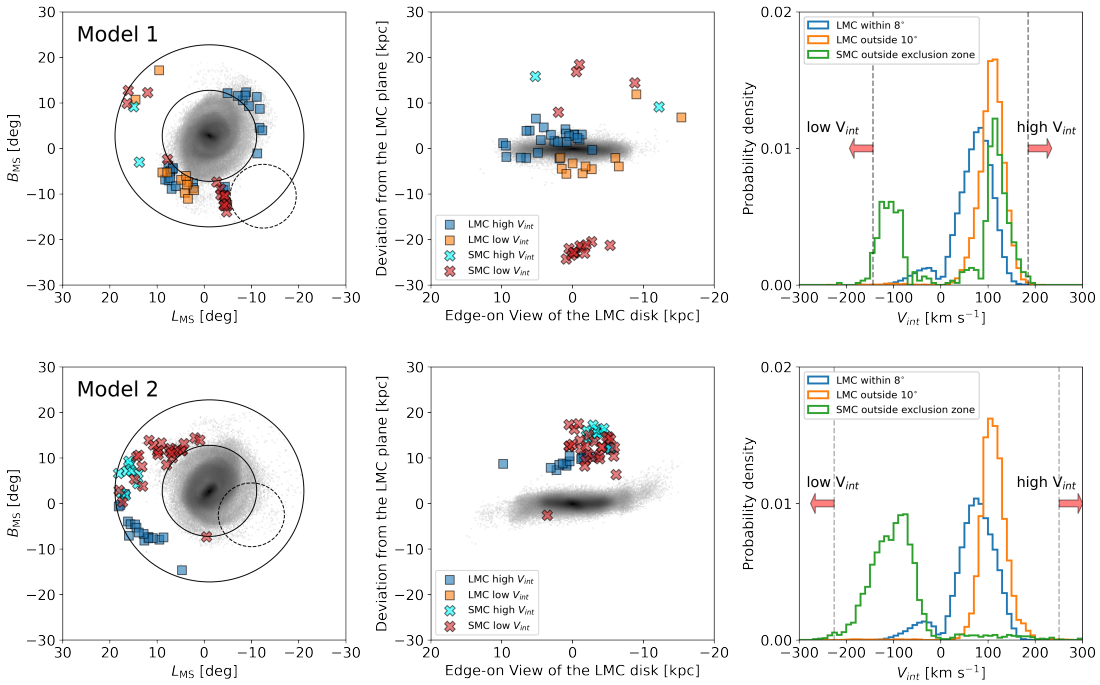

Figure 4.6: *Top row (Model 1):* the 2D star count map of the simulated LMC (left column) and the edge-on view of the simulated LMC (middle column) overplotted with the kinematic outliers with high and low V_{int}. As shown in the right column, the kinematic outliers are identified as 0.15% population in the low and high tails of the V_{int} distribution of all the star particles that are within the 10-20° annulus, but outside the SMC exclusion zone. These outliers preferentially reside in tidally-induced low-density structures and are found above and below the main disk plane. While high V_{int} star particles mainly originate in the LMC, low V_{int} star particles have both LMC and SMC origin. *Bottom row (Model 2):* The panels are the same as for Model 1. Similar to Model 1, the kinematic outliers are found in low surface brightness tidal features, but with a more skewed spatial distribution. Model 2 shows much stronger extraplanar features; most outliers reside 10-20 kpc above the main disk.

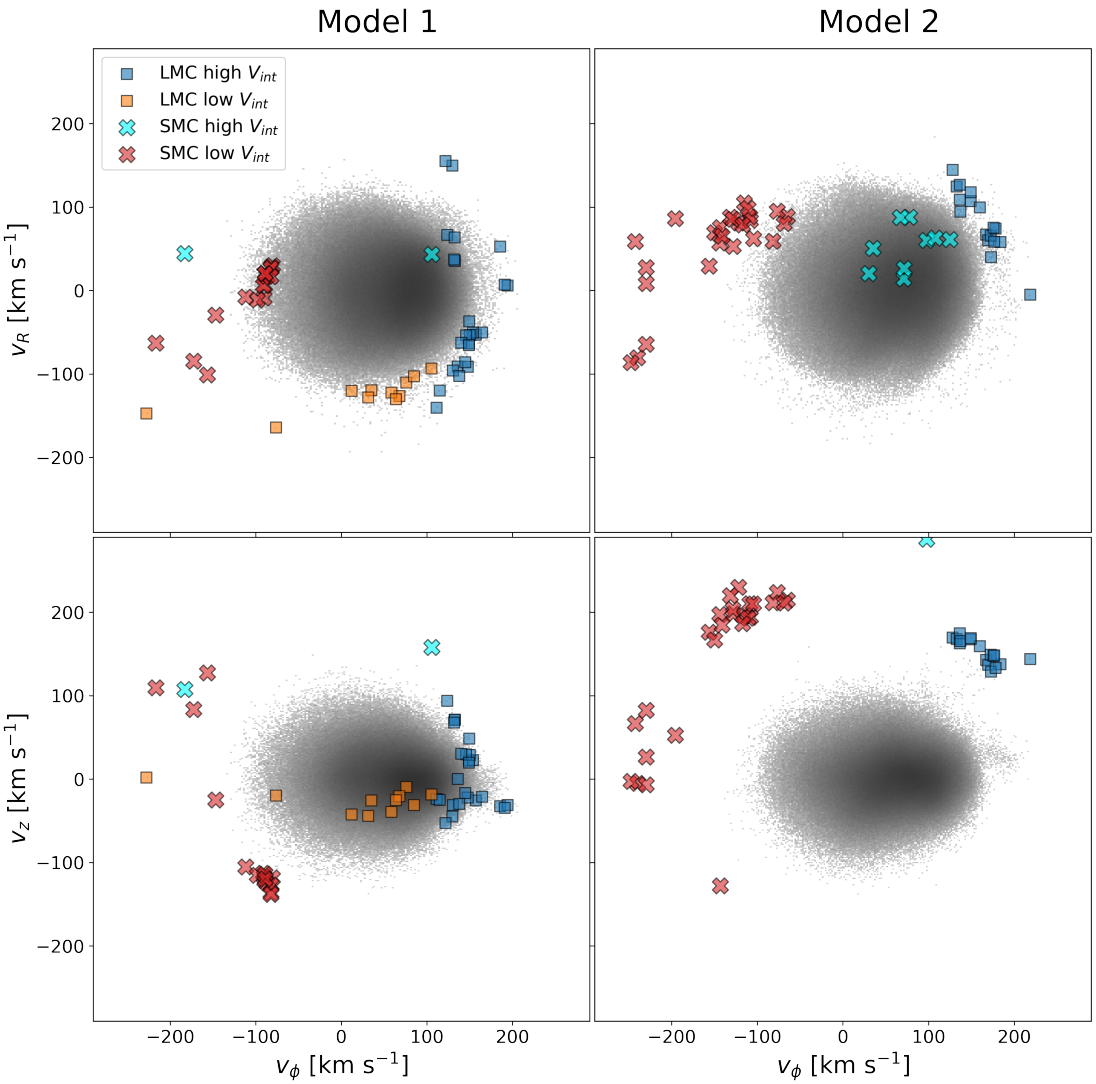

Figure 4.7: The vertical velocity (V_Z) and radial velocity (V_R) versus azimuthal velocity (V_ϕ) distributions for the simulated LMC from Model 1 (left columns) and Model 2 (right columns). Kinematical outliers from the LMC (blue and red squares) and SMC (cyan and orange crosses) are highlighted. The coloring scheme for kinematical outliers is the same as in Figure 4.6. As seen for the stars in the APOGEE O1 and O2 fields (see Figure 4.4), most of the V_{int}-selected kinematical outliers also have extreme individual velocity components compared to the stars in the main disk.

extreme kinematics (showing both retrograde velocities and prograde velocities at much higher velocity than the LMC disk), as exemplified by the 3D motions of the stars in the O1 and O2 fields, which cannot be viewed as a simple dynamical extension of the LMC disk.

- The stars in the O2 field have a spatial and metallicity distribution suggesting a connection to the SMC, but a velocity character extremely distinct from the SMC. Meanwhile, stars in the O1 field have an MDF resembling that of the outer LMC disk, but, again, a kinematical character quite distinct from that association. For these stars, one possibility is that they are highly disturbed tidal debris from the LMC/SMC interaction, which we explore by comparing their kinematical nature with those from hydrodynamical N-body simulations (see below). However, we cannot rule out that some APOGEE stars in these fields are of an "external" origin, the LMC-equivalent of accreted halo substructure, evidence for which has previously been suggested by Majewski et al. (2009).

From our comparisons with two hydrodynamical N-body simulations of an interacting LMC-SMC system (Besla et al. 2012), we find and conclude the following:

- The observed extreme velocity stars can be qualitatively reproduced by the tidal interactions between the LMC and SMC. The kinematical outliers identified in the simulations are extraplanar and preferentially found in tidally-induced low density features. This suggests that many of the stars in the SPS region are also out of the plane of the LMC.

- The detailed populations of the kinematical outliers depend on the interaction histories. In Model 1, where there is no direct collision between the MCs, the

contribution of the SMC particles to the high positive in-plane velocity population is negligible. In Model 2, where a recent direct collision occurred between the MCs, there is no contribution of the LMC particles to the high negative in-plane velocity population. We note that the LMC (SMC) debris are dominant components of the high positive (negative) in-plane velocity population in both models.

- Although the simulations are able to provide a plausible explanation for the kinematical properties of extreme velocity stars, neither models reproduce the details of the observed V_{int} distribution, including the extended high positive in-plane velocity tail seen in the observation. This might suggest that future models need a stronger perturbation (e.g., heavier SMC) to reach the observed highest V_{int} values. To test this, exploring a much broader parameter space for the interaction history is required.

Obviously, additional investigation is needed to solidify these conclusions. Larger spectroscopic samples would, of course, be a great help. But other data exist now that might help with firming up or ruling out the above conclusions. One particularly useful aid would be the discernment of relative distances of the LMC disk, SMC disk, and the periphery field stars, which, combined with the relative motions, would provide more definitive conclusions regarding the origin of the various spatio-kinematically distinct features. Unfortunately, at present the uncertainties associated with distance gauging individual sources at these great separations from us are still too large. We attempted to statistically assess the relative distances of stars based on color-magnitude distributions, but confess that these investigations proved quite inconclusive.

Chapter 5

The Search for White Dwarf - M-Dwarf Binaries in Large Stellar Spectral Databases using Artificial Intelligence

5.1 Introduction

Numerous astrophysical problems depend critically on the evolution of white dwarf - main sequence (WD-MS) binary systems. Depending on the initial parameters of the system, these alternate evolutionary paths can include one or two common envelope episodes, mass transfer via wind accretion, mass stripping, and stellar mergers (see Fig.1(a) for examples). Theory cannot yet securely predict the evolutionary path or the final product of specific main-sequence binaries, but such predictions are necessary for numerous astrophysical problems, from assessing occurrence rates of novae and cataclysmic variables (Kalomeni et al. 2016), to modeling extragalactic stellar populations (Götberg et al. 2019) and establishing formation rates and delay time distributions of important transients like Type Ia Supernovae and the progenitors of gravitational wave sources in the LIGO and LISA passbands (Lamberts et al. 2019).

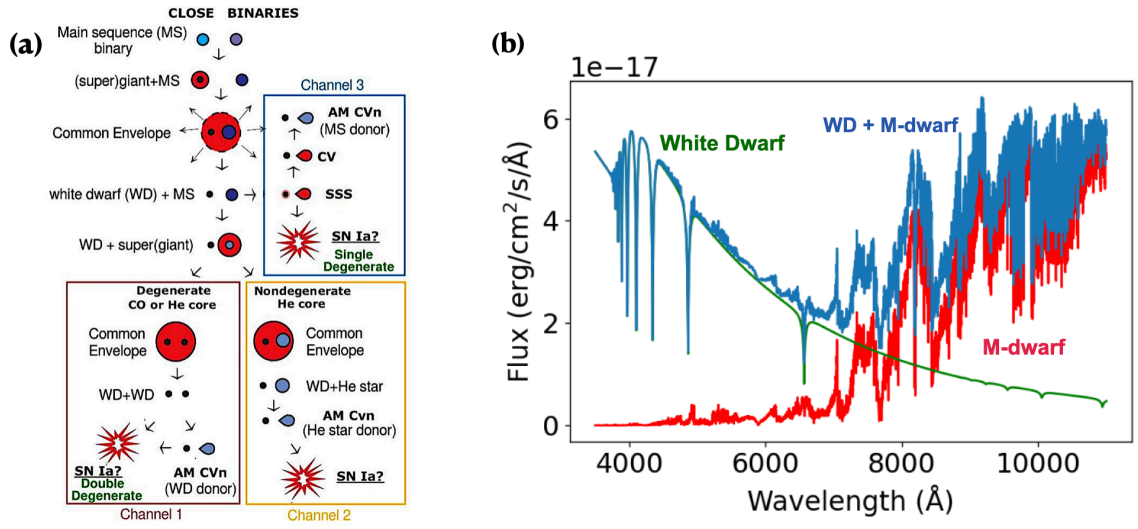

Figure 5.1: (a) The evolution of a close binary system, and a variety of pathways leading to various endpoints, including a Type Ia supernova (Toloza et al. 2019). (b) A sample spectrum of a WD-Md binary (blue line), which results from merging the individual spectra of a WD (green line) and an M-dwarf (red line).

To fully characterize the rich phenomenology of these binaries and enable reliable multivariate statistical analysis, assembling a catalog of WD-MS systems with accurately determined parameters in sufficient quantity is necessary.

About 70% of the main sequence stars in the Milky Way Galaxy are M-dwarfs (dM), making white dwarf - M-dwarf (WD-Md) binary systems the most common among white dwarf - main sequence (WD-MS) binary systems. They are also the easiest to identify due to the cool effective temperature of the M-dwarf photosphere compared with the typically hot temperature of a WD (Anguiano et al. 2022). Law et al. (2012) estimated that around 1 in 1000 M-dwarfs has a WD companion. This suggests that there are approximately 10^9 WD-Md pairs in the Milky Way. Surprisingly, there are only around 3,000 spectroscopically confirmed WD-Md binaries known (Rebassa-Mansergas et al. 2012; Ren et al. 2018). This small number hampers our ability to understand WD-Md pairs as potential progenitors of Type Ia supernovae and

sources of gravitational waves (Scaringi et al. 2023). Recently, a number of large scale spectroscopic surveys have been announced and/or have undergone their initial data releases. The largest among them that has available data released, the *Gaia* survey, through *Gaia* Data Release 3 (De Angeli et al. 2023) published low-resolution spectra for about 220 million objects, including over 8 million M-dwarfs. Similarly, Sloan Digital Sky Survey V (SDSS-V, Kollmeier et al. 2017) have also released its first batch of stellar spectra taken under the Milky Way Mapper (MWM) and Black Hole Mapper (BHM) programs via SDSS Data Release 18 (DR18, Almeida et al. 2023), with more expected on subsequent data releases. Consequently, the number of confirmed WD-Md pairs could potentially increase by two orders of magnitude. There is an urgent but achievable need to construct the most extensive WD-Md catalog to date, and these spectroscopic surveys provide a means to accomplish this. Such a catalog will enable us to establish a state-of-the-art sample for studying compact binary evolution and also allow us to directly address pressing astrophysical questions, such as assessing whether WD-Md pairs and their mass ratios are abundant enough to support an adequate rate of supernovae explosions. Moreover, such a complete catalog can offer insights into key aspects of stellar evolution, where vital mass transfer mechanisms are often modeled using simplified recipes that have limited predictive power and may only be calibrated on small samples of end products, if any.

To construct a WD-Md catalog from these large spectroscopic databases, we turn to Artificial Intelligence (AI) to help address this computationally intensive task. Identifying WD-Md binaries among the vast ocean of single stars and non-WD-Md binaries in stellar spectrum databases can be treated as an (extremely unbalanced) classification problem, and acquiring the characteristics of WD-Md binaries (i.e., temperature, radius and masses of WD and Md) can be formulated as regression problems.

Leveraging machine learning for the identification and characterization of WD-Md binaries has the potential to revolutionize astrophysics. Traditional methods rely on matching observed spectra to either theoretical or empirical template models (see Figure 5.1(b)). By comparing the measured spectra with various templates, these approaches may identify WD-Md binaries when provided high-resolution and high signal-to-noise (S/N) spectra (Rebassa-Mansergas et al. 2012). However, this methodology is no longer feasible to explore the vast amount of data released by enormous surveys like *Gaia* due to its slow computational speed. With significant advancements in machine learning, the methodology is now mature and well-equipped to tackle complex problems in scientific domains. Machine learning has recently been applied to various exotic astronomical phenomena, such as the hunt for supernovae (Lochner et al. 2016; Möller and de Boissière 2020), gravitational waves, and gravitational lensing (Hezaveh et al. 2017; Petrillo et al. 2017).

5.2 Contrastive Self-Supervised Learning

In general, the vast amount of annotated data required during training would pose significant challenge to the application of AI technology to the particular problem at hand. In the community of deep learning, machine learning models are often trained with hundreds of thousands if not millions of labeled samples, given that the number of parameters in a neural network could easily reach into the millions, if not billions. For example, ImageNet (Deng et al. 2009), a resource upon which most image recognition deep learning models have been trained, has more than 14 million labeled images. For the cases where annotated training data are rare and make the application of AI impractical — a problem known as few-shot learning — a number of paradigms have

been developed to circumvent this troublesome requirement. Here, we will focus on one of these paradigms, *contrastive self-supervised learning (contrastive SSL)*. Exploiting the nature that a neural network essentially learns a highly nonlinear mapping from a much higher dimensional input data space to a lower dimensional latent space, contrastive SSL is a discriminative approach that focuses on grouping similar samples closer and different samples far from each other in the learned latent space (Jaiswal et al. 2020). As such, contrastive SSL learns a summarization of the input sample that preserves as much information as possible while being robust to noise and other small changes, all without any annotation. We utilized SimCLRv2 (Chen et al. 2020) because of its simplicity yet high accuracy in the domain of image classification as well as its easy migration to our particular problem, as spectra are essentially one dimensional images. In our case, each input spectrum first goes through the process of data augmentation, where noise and bad-pixels are artificially added into each spectrum, generating 2 augmented inputs. The two inputs are then fed into a convolutional neural network followed by a multi-layer perceptron, generating a 64-dimensional vector representation of each input spectrum. Then the NX-ENT loss function (Chen et al. 2020) with the parameter of $\tau = 0.5$ (see above cited paper for the closed form of this function) was used, which minimizes the differences between the two 64-dimensional vectors from the 2 augmented input and at the same time maximizes the differences between the 64-dimensional vector representations from the different input spectra within the same batch.

Apart from the advantage of not requiring a large annotated training set, self-supervised learning usual results in a model with smaller generalization errors, less spurious correlations, and more resilience to noisy input data (Liu et al.Liu et al. 2021). This makes this method particularly well-suited for noisy input data scenarios, such as fi-

nancial time series data in stock and future markets, natural language processing with web-scraped data, and images with significant noise, the latter a common scenario for those taken under low light condition, which is the premise of many astronomical images and spectra.

5.3 Dataset, Architecture Design, and Training Strategy

We selected our training data from the SDSS DR17 and previous data releases. We only consider stellar spectra from the Baryon Oscillation Spectroscopic Survey (BOSS) spectrograph. The BOSS spectrograph has a resolution running from about R = 1560 at 3700 Angstroms to R= 2270 at 6000 Angstroms (blue channel), and from R = 1850 at 6000 Angstroms to R = 2650 at 9000 Angstroms (reds channel). The positive samples are the full WD-Md catalogue from Rebassa-Mansergas et al. (2012). The negative samples were picked from a combination of confirmed single WD, Md, and subdwarf (SD) stars, and then sampled randomly to have the same number of samples as the positive sample. The positive and negative samples combined together into the annotated dataset for fine-tuning, with a total sample size of 6438. This annotated dataset is then subdivided into a training set (60%), a validation set (20%), and a hold-out testing set (20%). 75000 SDSS stellar spectra from the BOSS spectrograph were also picked randomly from the full SDSS DR17 and previous data releases as the pretraining dataset.

One of the most common neural network architectures to analyze for images is the *convolutional neural network (CNN)*, a type of feed-forward neural network that

learns feature engineering by itself via tunable parameters in hierarchically applied filters and downsampling through pooling or non-unitary striding of the convolution layers. CNN is capable of hierarchically summarizing information from input, which is analogous to how human vision system works. In particular, we adapted Resnet (He et al. 2016) to be capable of dealing with one dimensional input. The input to our deep learning model, a sequence of flux values and error of flux values at given wavelength points, first goes through a convolution layer with a kernel size of 7 and a output channel of 64, and then goes through 4 Resnet blocks. The input to each Resnet block goes through two pathways. One pathway is a skip identity connection directly to the output if the input and output have the same number of channels or a convolution with kernel size of 1 otherwise, and the other pathway is a [convolution - batch normalization - ReLU - convolution - batch normalization - ReLU] sequence with all convolution layers within this pathway having a filter size of 3 and number of channels being [64, 128, 256, 256], respectively. Max pooling is performed in between each Resnet block and an adaptive average pooling is performed after the last Resnet block. The output is flattened and fed into a multi-layer perceptron (MLP). The MLP has an output channel of z=64 during pretraining and a channel of z=2 during fine-tuning. A diagram of the architecture is provided in Figure 5.2. The total parameter count in the encoder Resnet is 832 960, the total parameter count in the MLP is 45 056 during pretraining and 41 088 during fine-tuning.

Due to the large batch size used in pretraining, a traditional optimization method has been proven to produce unstable gradients. Thus, the network was trained with an Stochastic Gradient Descent (SGD)-based, Layer-wise Adaptive Rate Scaling (LARS) optimizer (You et al. 2017) with an initial learning rate of 0.1 during pretraining, a batch size of 1024. NX-ENT was used as loss function, and pretraining was considered

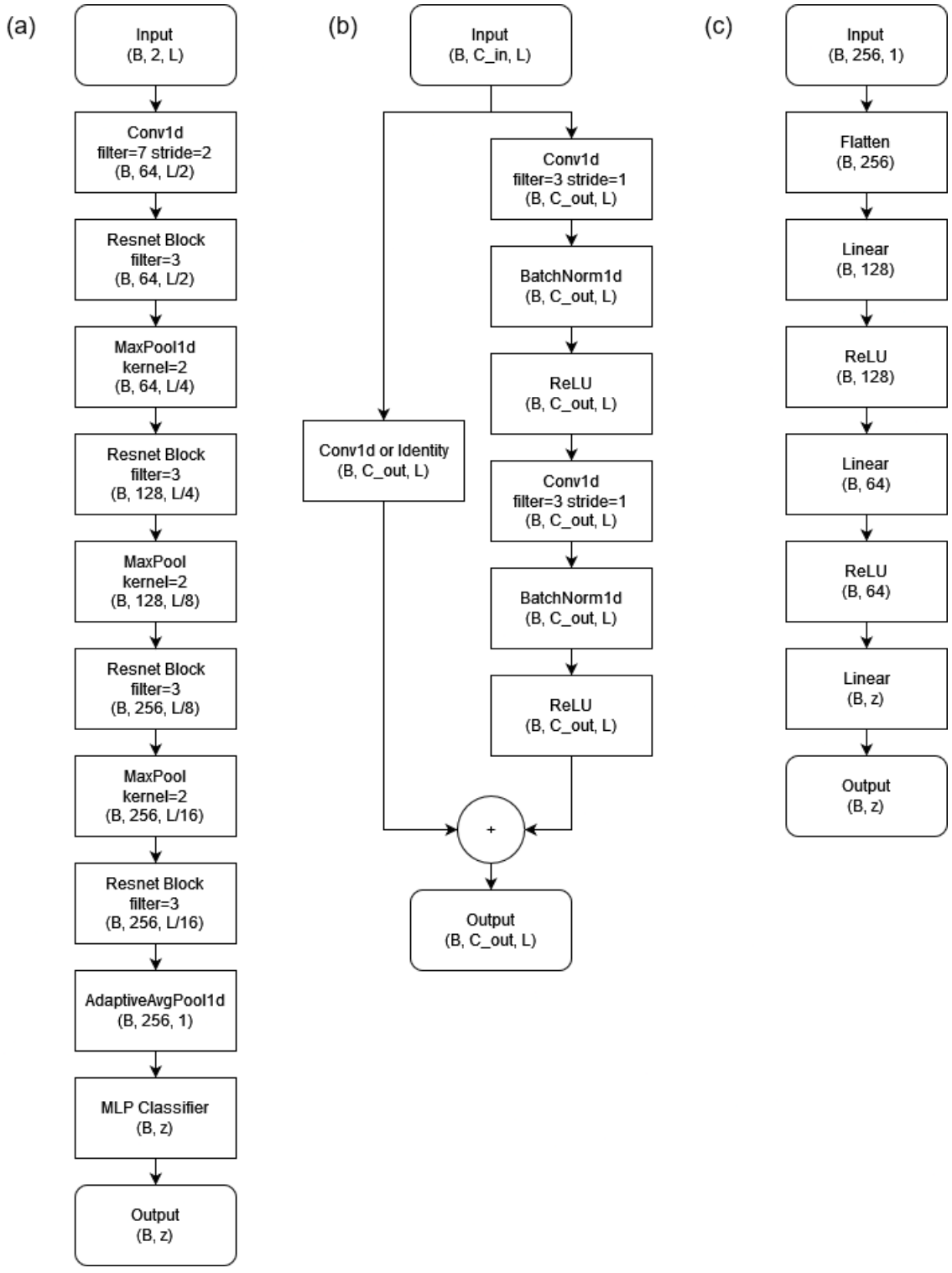

Figure 5.2: Architecture of the (a) 1d Resnet, (b) Resnet blocks within the Resnet, and (c) MLP classifier. Here the output and key hyperparameter of each layer is labeled following PyTorch convention. B is the batch size and L is the length of the sequence.

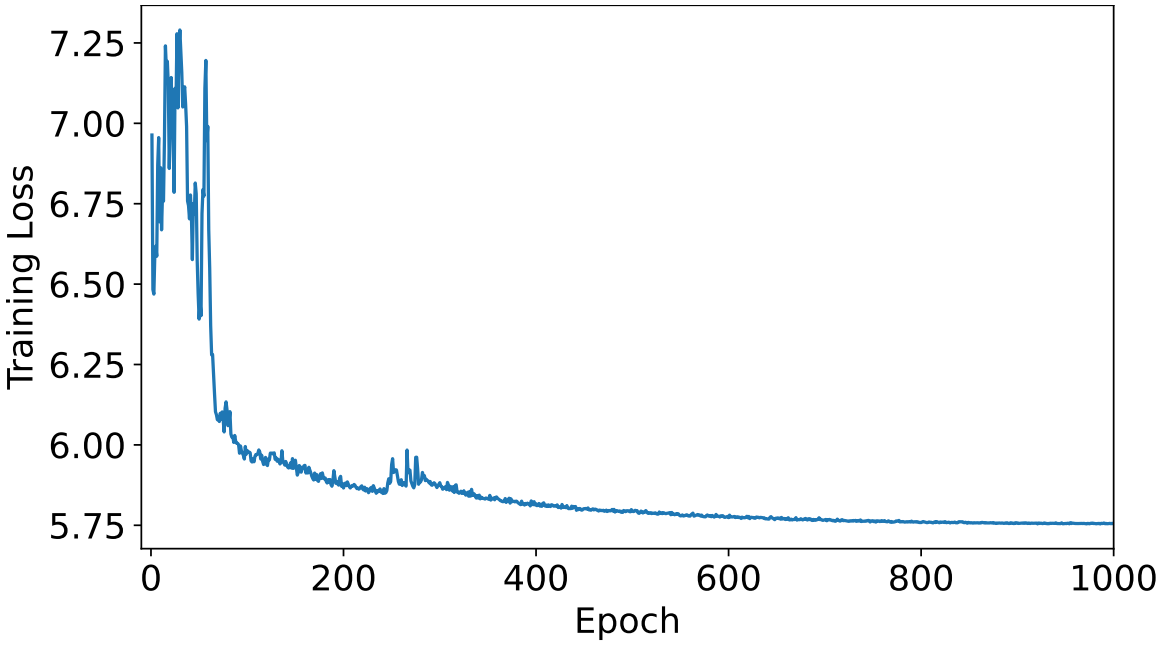

Figure 5.3: Loss history during pretraining. Pretraining is considered complete if the loss stopped improving by at least 10^{-2}, which occurred at epoch 600.

complete if the loss stopped improving by at least 10^{-2} in 30 epochs or upon reaching a maximum epoch of 1000. Cosine annealing learning rate scheduling is applied with a minimal learning rate of 10^{-6} at epoch 1000. The pretraining loss history is shown in Figure 5.3. During fine-tuning, the network is trained with an Adam optimizer (Kingma and Ba 2014) with an initial learning rate of 10^{-5} and no regularization. The batch size is reduced to 64, and cross-entropy is used as the loss function. The fine-tuning is considered complete if the validation dataset loss stopped improving after 30 epochs or reached a maximum epoch of 500. The epoch with the best validation dataset performance was chosen as the final machine learning model.

5.4 Results

We first test the model on our hold-out testing set, before migrating to inference on the SDSS Data Release 18 (DR18, Almeida et al. 2023) dataset. The first experiment is a test where we can evaluate the performance of the model, i.e., whether it overfitted, underfitted, or properly fitted the data. The second experiment on the full SDSS DR18 would provide us with an assessment of the zero-shot learning probability of the model. While DR18 has a limited number of stars in a very limited range of sky positions, it marks the first data releases of many from SDSS-V and we aim to eventually apply this methodology on the much larger complete SDSS-V dataset. As DR18 were from the same telescope and spectrograph setup, one can surmise that model trained on previous data releases should also be applicable on DR18, despite spectra within DR18 having significantly lower signal-to-noise ratio than before due to shorter exposure time. Nevertheless, it is not a straightforward process as we will focus on in later sections, partly due to the black box nature of deep learning models.

5.4.1 Hold-out testing set

We first performed a test on the hold-out testing set, where a portion of the annotated spectra were set aside and never seen during training. A perfect model would be able to achieve an accuracy of 100%, meaning no false positives or false negatives. For our testing set (1312 spectra, 656 binaries and 656 single WD/Md), we achieved an accuracy of 95.51%, with 44 false positives and 15 false negatives.

A further test is performed on an annotated dataset with only negative samples (i.e., samples of single stars), since there are a significant number of leftovers during the selection of the training set. A perfect model would be able to label all 100% of the

dataset as negative, and in practice, we have a false positive rate of 2.81% within this leftover sample of 25,983 spectra. This indicates that the model is very capable at the WD-Md classification task.

5.4.2 SDSS DR18

We further performed inference on SDSS DR18 spectra. Compared to our training, validation, and testing set, the DR18 spectra taken as part of SDSS-V have lower signal-to-noise ratio, as exposure time was decreased for the collection of these data (Kollmeier et al. 2017), although they were collected with the same spectrograph and detector setup, making this a good option for a zero-shot learning scenario. As DR18 includes both stellar and non-stellar (e.g., AGNs targeted from the Black Hole Mapper (BHM) program) spectra, we first selected for stellar spectra by enforcing `class=="STAR"`. That leaves us with 3862 stellar spectra out of 25,000 spectra released in DR18.

However, directly applying the fine-tuned neural network on DR18 gives us unreasonable results, where the entire WD branch in the color-absolute magnitude diagram is labeled as high probability binary candidates, clear evidence for the lack of ability to generalize outside the coverage of the training set, despite the high classification accuracy on the hold-out testing set. In the classical problem of bias-variance trade-off, a complex model would usually achieve higher accuracy but less ability to generalize and a simpler model would be vice versa. Therefore, inspired by the matching network zero-shot learning technique proposed in Vinyals et al. (2016), we kept the pretrained network intact without any fine-tuning and projected the annotated training set and DR18 spectra onto the 64-dimensional space (the output of our pretrained

network). We examined the distribution of our annotated training set and DR18 in this 64-dimensional space, and found their distribution to be very similar, thus indicating a high chance of success in zero-shot learning. A k-nearest neighbor (KNN) classifier was then trained on the annotated training set in the 64-dimensional space with 5-fold cross validation to determine the best value for $k = 12$. The probability distribution of a system being a WD-Md binary as a function of position in the *Gaia* color-absolute magnitude diagram is shown in Figure 5.4. In theory, by combining a blue WD star with a red Md star, the system should have a color that is in between the Md and WD branch. We observe such a trend in our own catalogue, with almost all systems that live between the Md and WD branch being high probability candidates. We also notice that the redder end of the WD branch also has a concentration of binary candidates, the reason of which is under investigation.

Furthermore, we see an initially non-intuitive feature of our output in that a large portion of the overall dataset is being labeled as WD-Md binary systems — much more than would be theoretically expected. However, a quick investigation into the `FIRSTCARTON`, which encodes the selection reasoning and criteria used by the SDSS-V MWM survey for targeting sources, reveals that a large fraction of the survey specifically targets compact binary systems having a UV excess (e.g. `mwm_cb_uvex` and `mwm_cb_gaiagalex`). Therefore, in the end, it is not surprising that binary systems, and specifically WD-binaries, might be over-represented in the SDSS DR18 stellar catalog, and therefore gives us a higher than expected ratio of WD-Md binaries.

Another factor that we did not initially anticipate was revealed by a more thorough examination of the DR18 spectra. It seems that the removal of airglow lines in DR18 is less than ideal compared with the spectra seen in our training set. This may be a result of the lower signal-to-noise of the SDSS-V spectra. This poor line removal has

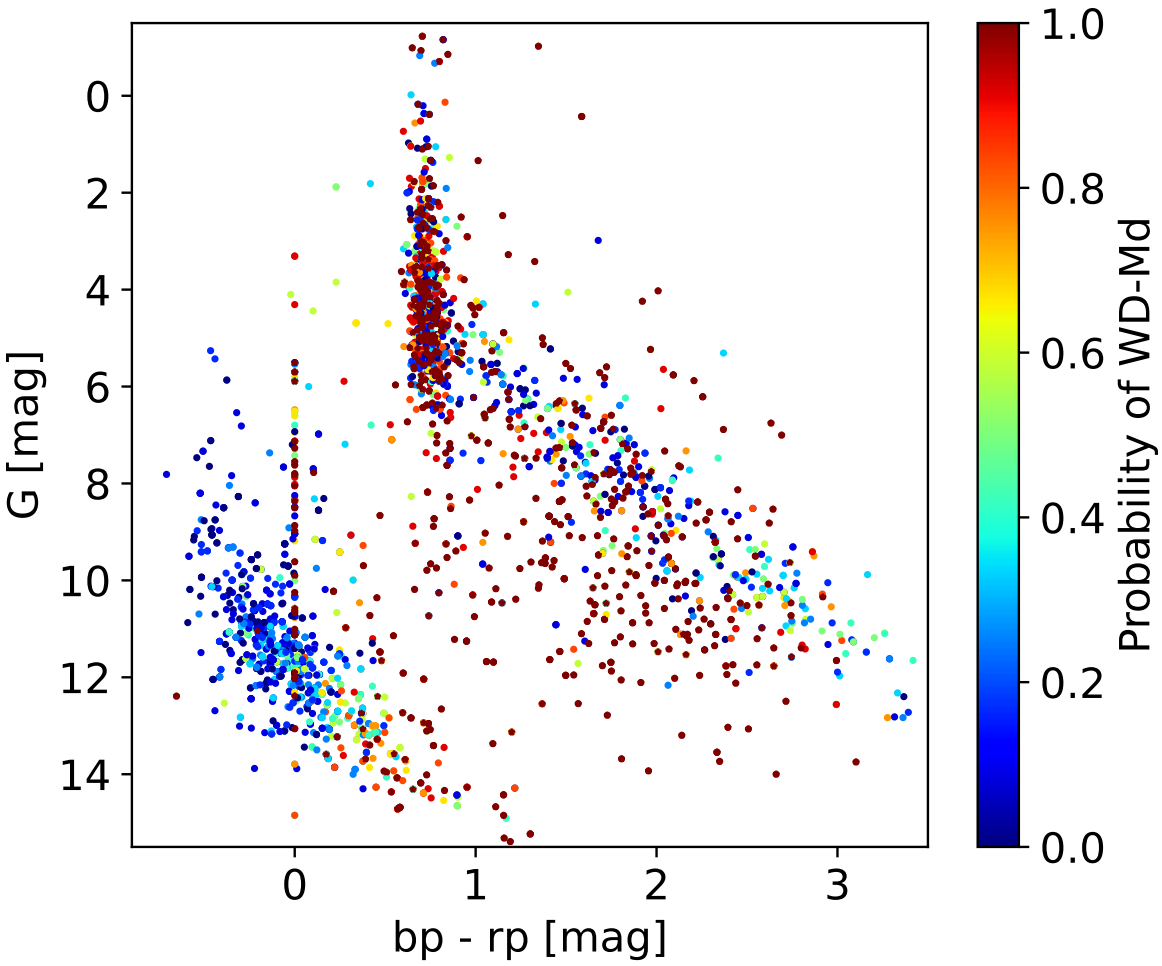

Figure 5.4: Probability of a system being a WD-Md binary as a function of position in the *Gaia* color-absolute magnitude diagram for stars in SDSS DR18. We noticed that the redder end of WD branch and the areas in between the WD and Md branches have higher numbers of high probability binary candidates. High probability candidates near the Md branch do not seem to exhibit any patterns.

the potential to throw off the predictions as it changes the noise profile and potentially makes the decision making process different; but the effect is currently unknown as there are no overlaps between DR18 and previous data releases nor is there a WD-Md catalogue selected from this most recent data release, thus no annotated training set could be put together easily for further investigation. Overall the preliminary testing on DR18 shows promise that our model is working reasonably under a new

dataset taken from the same telescope, spectrograph, and detector, but with different exposure lengths (i.e., signal-to-noise) and further refinement would produce hopeful results. However, care needs to be take during model design and training strategy to avoid overfitting.

A few examples of high probability candidates are shown in Figure 5.5. We can see a clear increase of flux in the bluer wavelength end and absorption lines indicative of WD below 5000 A. On the red wavelength end, we can once again spot clear indications of a Md, the complicated series of molecular lines between 6000 A and 8000 A. Therefore, even without going through the process of template fitting, one can be sure that the candidates shown here are indeed WD-Md binaries.

5.5 Discussion and Conclusion

In conclusion, by utilizing a novel machine learning method, contrastive self-supervised learning and fine-tuning, we successfully trained a Resnet-based deep learning model with only ∼6000 annotated training samples. The classification accuracy on a hold-out testing set is ∼96% after fine-tuning, but at the cost of the ability to generalize to lower S/N samples. Preliminary attempts at searching for WD-Md binaries on SDSS DR18 with few-shot learning techniques show promise of the model in situations where a machine learning model trained from data taken on one instrument can be utilized on other data from the same instrument even though the exposure time (thus noise profile) is different.

We are optimistic about the further application and innovation of contrastive SSL in the field of observational astronomy. A common problem faced by applications of deep learning is the lack of annotated data for a training set despite having a

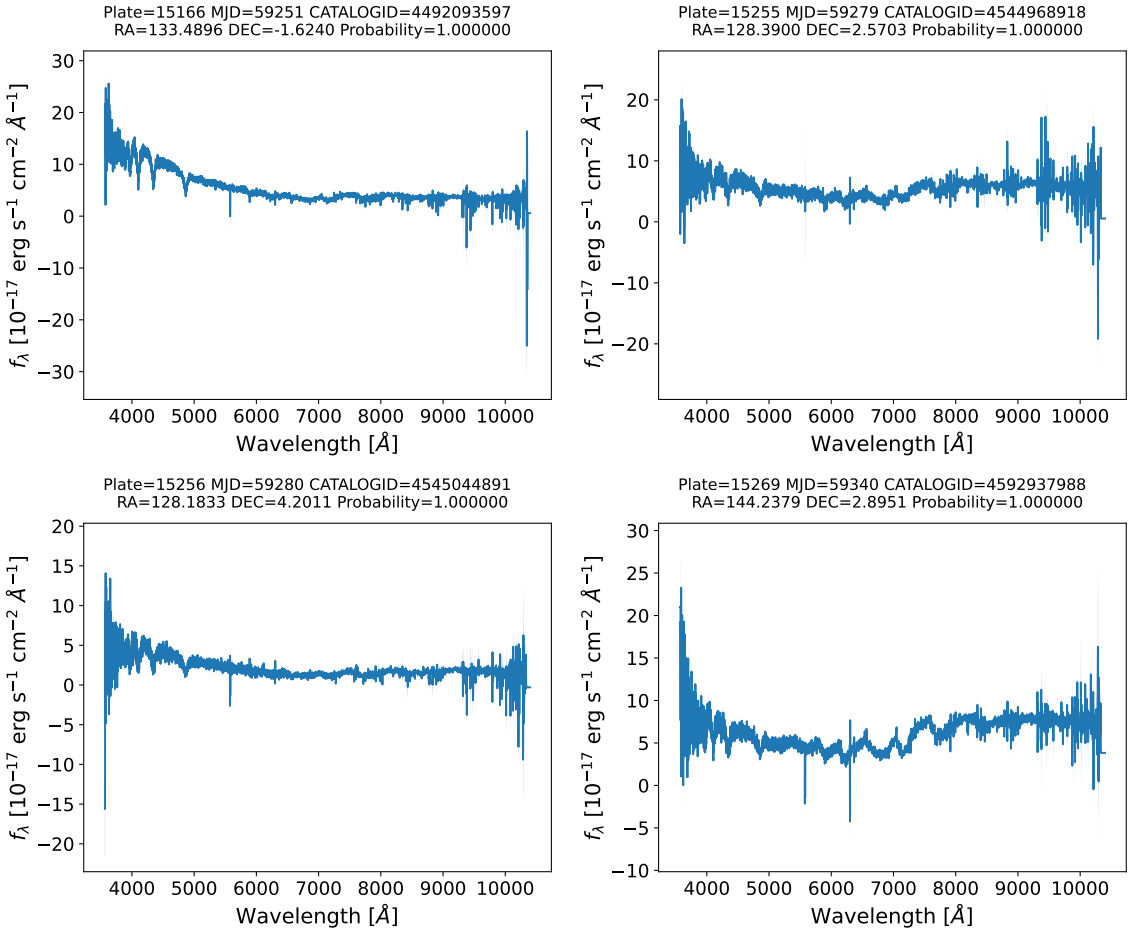

Figure 5.5: Four examples of high probability WD-Md candidates found in SDSS DR18 spectra. WD absorption lines below 5000 A and Md spectral wiggle patterns beyond 6000 A are clearly visible in all four examples, with the two examples on the left being more WD dominated and the two on the right having roughly equal contribution from both stars in the binary.

large amount of unannotated data, and contrastive SSL presents a solution to the issue. Traditionally, such an issue is usually solved by first applying unsupervised learning methods, such as principle component analysis (PCA), and/or clustering algorithms, such as t-SNE, on the unannotated data to extract key features, and then using a classification or regression algorithm on the limited annotated data to train the machine learning model to solve the problem. In comparison, contrastive SSL has the advantage of smaller generalization errors, less spurious correlations, and

more resilience to noise (Liu et al. 2021). Furthermore, contrastive SSL is capable of extracting non-linear features as neural network is mathematically speaking a non-linear mapping from an input data manifold to latent space, unlike PCA, which is mathematically a linear dimensional reduction technique. As such, contrastive learning can play a large role in the exploration of the ever increasing volumes of data being generated by large sky surveys. In the near term, application to the *Gaia* low resolution stellar spectra stands to herald a very beneficial immediate reward.

Chapter 6

Conclusion

In this thesis, I have presented several discoveries enabled by the new generation of large sky surveys, *Gaia* and APOGEE, in the context of Galactic and extra-galactic astronomy. Using measured stellar kinematics to infer global dynamics, we discovered the precession of the Galactic warp in the outer stellar disk. While such a phenomenon is strong in medium-aged thin disk stars, older populations in the thick disk and stellar halo, as well as very young populations, do not show such a behavior. The precession rate remains consistent across different populations and we believe the warp to be induced by interactions of the Milky Way disk with dwarf galaxies. By digging deeper into the velocity dispersion patterns of Milky Way stars, we also discovered that many previously commonly adopted assumptions made in the calculation of surface mass density (e.g. velocity dispersion profile, stellar density profile) are in fact inconsistent with observations. Small but statistically significant wiggle patterns exist in velocity dispersion, and while the traditional Jeans Equation modelling of the thick disk population at large vertical height is capable of reproducing previously established surface density measurement results, the thin disk population, populations close to midplane, and populations outside the solar radius pose significant challenges to the analytical formulation. Applying a similar technique of 3-D stellar kinematics to dynamical studies of the LMC population reveals a kinematically and chemically distinct population to the south of the LMC. Its velocity distribution

is distinct from that of the LMC disk, but consistent with theoretical predictions of perturbations from SMC. Lastly, digging ever deeper into the large amount of data provided by current and future sky surveys, we proposed a novel contrastive learning neural network to mitigate the inability to apply machine learning in spectroscopic analysis when limited by annotated training sets. In the task of WD-Md searching, the proposed network achieved high accuracy in the hold-out testing set and good generalization in the form of promising results in never-before-seen and more noisy spectra.

While impressive progresses have been made by data mining in large sky surveys, as have been discussed in each chapter separately, a number of outstanding questions still remains. Most evidence for galactic warp favors gravitational perturbation as possible cause for the Galactic warp of the Milky Way, but the culprit of which dwarf galaxy has not been identified. Further exploration by comparing numerical simulations would prove to be beneficial. The consensus density profiles of stellar populations have also been called into question. Evidence for flaring (e.g., Mackereth et al. 2017) and warping (e.g., Cheng et al. 2020) suggests that the outer disk might not be following the known scale-height of thin and thick disk, while recent foray into mono-abundance populations (e.g., Lian et al. 2022) reveals that scale height of stellar populations can vary drastically with Galactocentric radius and chemical composition. On the other hand, velocity dispersion profiles are also more complicated than what was being assumed in most previous studies, and some have also proposed alternative dark matter models that allows for the clumping of dark matter beyond the standard halo model. Interactions between LMC, SMC and MW is also a topic where observational results have outpaced theoretical understanding, and a number of observed results, including the kinematical distinct population discussed in

Chapter 4, are poorly explained by theoretical works. Lastly, while machine learning techniques have been successfully applied to a number of astrophysics problems, such an endeavor is still quite limited due to the lack of annotated training samples in many astrophysical data mining problems, and adaption of more cutting-edge deep learning techniques, such as contrastive SSL, will prove to be largely beneficial. With many larger and deeper on-going and planned sky surveys, such as Legacy Survey of Space and Time (LSST, Ivezić et al. 2019), astronomers are increasingly challenged by the growing volume of data to be analyzed. Nevertheless, these sky surveys are bound to result in many revolutionary discoveries in many fields of astronomy in the foreseeable future.

Bibliography

Abbott, T. M. C. et al. (2018). "Dark Energy Survey year 1 results: Cosmological constraints from galaxy clustering and weak lensing". *PhRvD* 98, 043526. DOI: 10.1103/PhysRevD.98.043526. arXiv: 1708.01530 [astro-ph.CO].

Abdurro'uf et al. (2022). "The Seventeenth Data Release of the Sloan Digital Sky Surveys: Complete Release of MaNGA, MaStar, and APOGEE-2 Data". *ApJS* 259, 35. DOI: 10.3847/1538-4365/ac4414. arXiv: 2112.02026 [astro-ph.GA].

Ahumada, Romina et al. (2020). "The 16th Data Release of the Sloan Digital Sky Surveys: First Release from the APOGEE-2 Southern Survey and Full Release of eBOSS Spectra". *ApJS* 249, 3. DOI: 10.3847/1538-4365/ab929e. arXiv: 1912.02905 [astro-ph.GA].

Almeida, Andrés et al. (2023). "The Eighteenth Data Release of the Sloan Digital Sky Surveys: Targeting and First Spectra from SDSS-V". *ApJS* 267, 44. DOI: 10.3847/1538-4365/acda98. arXiv: 2301.07688 [astro-ph.GA].

Amôres, E. B., A. C. Robin, and C. Reylé (2017). "Evolution over time of the Milky Way's disc shape". *A&A* 602, A67. DOI: 10.1051/0004-6361/201628461. arXiv: 1701.00475 [astro-ph.GA].

Anders, F. et al. (2019). "Photo-astrometric distances, extinctions, and astrophysical parameters for Gaia DR2 stars brighter than G = 18". *A&A* 628, A94. DOI: 10.1051/0004-6361/201935765. arXiv: 1904.11302 [astro-ph.GA].

Anguiano, Borja et al. (2020). "The Stellar Velocity Distribution Function in the Milky Way Galaxy". *AJ* 160, 43. DOI: 10.3847/1538-3881/ab9813. arXiv: 2005.14534 [astro-ph.GA].

Anguiano, Borja et al. (2022). "White Dwarf Binaries across the H-R Diagram". *AJ* 164, 126. DOI: 10.3847/1538-3881/ac8357. arXiv: 2207.13992 [astro-ph.SR].

Antoja, T. et al. (2018). "A dynamically young and perturbed Milky Way disk". *Nature* 561, 360–362. DOI: 10.1038/s41586-018-0510-7. arXiv: 1804.10196 [astro-ph.GA].

Aumer, Michael, James Binney, and Ralph Schönrich (2016). "Age-velocity dispersion relations and heating histories in disc galaxies". *MNRAS* 462, 1697–1713. DOI: 10.1093/mnras/stw1639. arXiv: 1607.01972 [astro-ph.GA].

Aumer, Michael and Ralph Schönrich (2015). "Origin of the high v_{los} feature in the Galactic bar". *MNRAS* 454, 3166–3184. DOI: 10.1093/mnras/stv2252. arXiv: 1507.00907 [astro-ph.GA].

Auvergne, M. et al. (2009). "The CoRoT satellite in flight: description and performance". *A&A* 506, 411–424. DOI: 10.1051/0004-6361/200810860. arXiv: 0901.2206 [astro-ph.SR].

Bahcall, J. N. (1984). "Self-consistent determinations of the total amount of matter near the sun." *ApJ* 276, 169–181. DOI: 10.1086/161601.

Baldwin, J. E., D. Lynden-Bell, and R. Sancisi (1980). "Lopsided galaxies". *MNRAS* 193, 313–319. DOI: 10.1093/mnras/193.2.313.

Battaner, E., E. Florido, and M. L. Sanchez-Saavedra (1990). "Intergalactic magnetic field and galactic warps." *A&A* 236, 1.

Belokurov, Vasily et al. (2017). "Clouds, Streams and Bridges. Redrawing the blueprint of the Magellanic System with Gaia DR1". *MNRAS* 466, 4711–4730. DOI: 10.1093/mnras/stw3357. arXiv: 1611.04614 [astro-ph.GA].

Belokurov, Vasily A. and Denis Erkal (2019). "Clouds in arms". *MNRAS* 482, L9–L13. DOI: 10.1093/mnrasl/sly178. arXiv: 1808.00462 [astro-ph.GA].

Bennett, Morgan and Jo Bovy (2019). "Vertical waves in the solar neighbourhood in Gaia DR2". *MNRAS* 482, 1417–1425. DOI: 10.1093/mnras/sty2813. arXiv: 1809.03507 [astro-ph.GA].

Bennett, Morgan, Jo Bovy, and Jason A. S. Hunt (2022). "Exploring the Sgr-Milky Way-disk Interaction Using High-resolution N-body Simulations". *ApJ* 927, 131. DOI: 10.3847/1538-4357/ac5021. arXiv: 2107.08055 [astro-ph.GA].

Bensby, T., S. Feltzing, and I. Lundström (2003). "Oxygen in the Galactic Thin and Thick Disks". In: *CNO in the Universe*. Ed. by Corinne Charbonnel, Daniel Schaerer, and Georges Meynet. Vol. 304. Astronomical Society of the Pacific Conference Series, p. 175. DOI: 10.48550/arXiv.astro-ph/0212029. arXiv: astro-ph/0212029 [astro-ph].

— (2004). "A possible age-metallicity relation in the Galactic thick disk?" *A&A* 421, 969–976. DOI: 10.1051/0004-6361:20035957. arXiv: astro-ph/0403591 [astro-ph].

Bensby, T., S. Feltzing, and M. S. Oey (2014). "Exploring the Milky Way stellar disk. A detailed elemental abundance study of 714 F and G dwarf stars in the solar neighbourhood". *A&A* 562, A71. DOI: 10.1051/0004-6361/201322631. arXiv: 1309.2631 [astro-ph.GA].

Bergemann, Maria et al. (2018). "Two chemically similar stellar overdensities on opposite sides of the plane of the Galactic disk". *Nature* 555, 334–337. DOI: 10.1038/nature25490. arXiv: 1803.00563 [astro-ph.GA].

Bertone, Gianfranco, Dan Hooper, and Joseph Silk (2005). "Particle dark matter: evidence, candidates and constraints". *PhR* 405, 279–390. DOI: 10.1016/j.physrep.2004.08.031. arXiv: hep-ph/0404175 [hep-ph].

Besla, Gurtina et al. (2012). "The role of dwarf galaxy interactions in shaping the Magellanic System and implications for Magellanic Irregulars". *MNRAS* 421, 2109–2138. DOI: 10.1111/j.1365-2966.2012.20466.x. arXiv: 1201.1299 [astro-ph.GA].

Besla, Gurtina et al. (2016). "Low Surface Brightness Imaging of the Magellanic System: Imprints of Tidal Interactions between the Clouds in the Stellar Periphery". *ApJ* 825, 20. DOI: 10.3847/0004-637X/825/1/20. arXiv: 1602.04222 [astro-ph.GA].

Bienayme, O., A. C. Robin, and M. Creze (1987). "The mass density in our galaxy. I. A dynamical model constrained by general star counts". *A&A* 180, 94–110.

Binney, James (1992). "Warps." *ARA&A* 30, 51–74. DOI: 10.1146/annurev.aa.30.090192.000411.

— (2012a). "Actions for axisymmetric potentials". *MNRAS* 426, 1324–1327. DOI: 10.1111/j.1365-2966.2012.21757.x. arXiv: 1207.4910 [astro-ph.GA].

— (2012b). "More dynamical models of our Galaxy". *MNRAS* 426, 1328–1337. DOI: 10.1111/j.1365-2966.2012.21692.x. arXiv: 1207.4917 [astro-ph.GA].

Bland-Hawthorn, Joss and Ortwin Gerhard (2016). "The Galaxy in Context: Structural, Kinematic, and Integrated Properties". *ARA&A* 54, 529–596. DOI: 10.1146/annurev-astro-081915-023441. arXiv: 1602.07702 [astro-ph.GA].

Bland-Hawthorn, Joss et al. (2019). "The GALAH survey and Gaia DR2: dissecting the stellar disc's phase space by age, action, chemistry, and location". *MNRAS* 486, 1167–1191. DOI: 10.1093/mnras/stz217. arXiv: 1809.02658 [astro-ph.GA].

Blanton, Michael R. et al. (2017). "Sloan Digital Sky Survey IV: Mapping the Milky Way, Nearby Galaxies, and the Distant Universe". *AJ* 154, 28. DOI: 10.3847/1538-3881/aa7567. arXiv: 1703.00052 [astro-ph.GA].

Bobylev, V. V. (2010). "Parameters of the local warp of the stellar-gaseous galactic disk from the kinematics of Tycho-2 nearby red giant clump stars". *Astron-*

omy Letters 36, 634–644. DOI: 10.1134/S1063773710090021. arXiv: 1008.4208 [astro-ph.GA].

Borucki, William J. et al. (2010). "Kepler Planet-Detection Mission: Introduction and First Results". *Science* 327, 977. DOI: 10.1126/science.1185402.

Bosma, A. (1978). "The distribution and kinematics of neutral hydrogen in spiral galaxies of various morphological types". PhD thesis. -.

Bovy, Jo (2015). "galpy: A python Library for Galactic Dynamics". *ApJS* 216, 29. DOI: 10.1088/0067-0049/216/2/29. arXiv: 1412.3451 [astro-ph.GA].

Bovy, Jo and Scott Tremaine (2012). "On the Local Dark Matter Density". *ApJ* 756, 89. DOI: 10.1088/0004-637X/756/1/89. arXiv: 1205.4033 [astro-ph.GA].

Bovy, Jo et al. (2016). "The Shape of the Inner Milky Way Halo from Observations of the Pal 5 and GD–1 Stellar Streams". *ApJ* 833, 31. DOI: 10.3847/1538-4357/833/1/31. arXiv: 1609.01298 [astro-ph.GA].

Bowen, I. S. and Jr. Vaughan A. H. (1973). "The optical design of the 40-in. telescope and of the Irénée DuPont telescope at Las Campanas Observatory, Chile." *ApOpt* 12, 1430–1434. DOI: 10.1364/AO.12.001430.

Burke, Bernard F. (1957). "Systematic distortion of the outer regions of the galaxy." *AJ* 62, 90. DOI: 10.1086/107463.

Calcáneo-Roldán, Carlos et al. (2000). "Galaxy destruction and diffuse light in clusters". *MNRAS* 314, 324–333. DOI: 10.1046/j.1365-8711.2000.03289.x. arXiv: astro-ph/9811450 [astro-ph].

Carrillo, I. et al. (2019). "Kinematics with Gaia DR2: the force of a dwarf". *MNRAS* 490, 797–812. DOI: 10.1093/mnras/stz2343. arXiv: 1903.01493 [astro-ph.GA].

Chambers, K. C. et al. (2016). "The Pan-STARRS1 Surveys". *arXiv e-prints*, arXiv:1612.05560. arXiv: 1612.05560 [astro-ph.IM].

Chen, Ting et al. (2020). "Big self-supervised models are strong semi-supervised learners". *Advances in neural information processing systems* 33, 22243–22255.

Chen, Xiaodian et al. (2019). "An intuitive 3D map of the Galactic warp's precession traced by classical Cepheids". *Nature Astronomy* 3, 320–325. DOI: 10.1038/s41550-018-0686-7. arXiv: 1902.00998 [astro-ph.GA].

Cheng, Xinlun et al. (2019). "Ripple Patterns in In-plane Velocities of OB Stars from LAMOST and Gaia". *ApJL* 872, L1. DOI: 10.3847/2041-8213/ab020e. arXiv: 1901.09305 [astro-ph.GA].

Cheng, Xinlun et al. (2020). "Exploring the Galactic Warp through Asymmetries in the Kinematics of the Galactic Disk". *ApJ* 905, 49. DOI: 10.3847/1538-4357/abc3c2. arXiv: 2010.10398 [astro-ph.GA].

Cheng, Xinlun et al. (2024). "The surface mass density of the Milky Way: does the traditional K_Z approach work in the context of new surveys?" *MNRAS* 527, 959–976. DOI: 10.1093/mnras/stad3013. arXiv: 2309.17405 [astro-ph.GA].

Choi, Yumi et al. (2018). "SMASHing the LMC: A Tidally Induced Warp in the Outer LMC and a Large-scale Reddening Map". *ApJ* 866, 90. DOI: 10.3847/1538-4357/aae083. arXiv: 1804.07765 [astro-ph.GA].

Choi, Yumi et al. (2022). "The Recent LMC-SMC Collision: Timing and Impact Parameter Constraints from Comparison of Gaia LMC Disk Kinematics and N-body Simulations". *ApJ* 927, 153. DOI: 10.3847/1538-4357/ac4e90. arXiv: 2201.04648 [astro-ph.GA].

Chou, Mei-Yin et al. (2010). "The Chemical Evolution of the Monoceros Ring/Galactic Anticenter Stellar Structure". *ApJL* 720, L5–L10. DOI: 10.1088/2041-8205/720/1/L5. arXiv: 1007.1056 [astro-ph.GA].

Cioni, M. -R. L. et al. (2011). "The VMC survey. I. Strategy and first data". *A&A* 527, A116. DOI: 10.1051/0004-6361/201016137. arXiv: 1012.5193 [astro-ph.CO].

Creze, M. et al. (1998). "The distribution of nearby stars in phase space mapped by Hipparcos. I. The potential well and local dynamical mass". *A&A* 329, 920–936. arXiv: astro-ph/9709022 [astro-ph].

Cropper, M. et al. (2018). "Gaia Data Release 2. Gaia Radial Velocity Spectrometer". *A&A* 616, A5. DOI: 10.1051/0004-6361/201832763. arXiv: 1804.09369 [astro-ph.IM].

Cuddeford, Phil and Peter Amendt (1992). "The radius dependence of velocity dispersion in spiral galaxies". *MNRAS* 256, 166–176. DOI: 10.1093/mnras/256.1.166.

Cullinane, L. R. et al. (2022). "The Magellanic Edges Survey - II. Formation of the LMC's northern arm". *MNRAS* 510, 445–468. DOI: 10.1093/mnras/stab3350. arXiv: 2106.03274 [astro-ph.GA].

Czekaj, M. A. et al. (2014). "The Besançon Galaxy model renewed. I. Constraints on the local star formation history from Tycho data". *A&A* 564, A102. DOI: 10.1051/0004-6361/201322139. arXiv: 1402.3257 [astro-ph.GA].

D'Onghia, E. et al. (2016). "Excitation of Coupled Stellar Motions in the Galactic Disk by Orbiting Satellites". *ApJ* 823, 4. DOI: 10.3847/0004-637X/823/1/4. arXiv: 1511.01503 [astro-ph.GA].

Darling, Keir and Lawrence M. Widrow (2019). "Eigenfunctions of Galactic phase space spirals from dynamic mode decomposition". *MNRAS* 490, 114–123. DOI: 10.1093/mnras/stz2539. arXiv: 1904.08896 [astro-ph.GA].

Dawson, Kyle S. et al. (2013). "The Baryon Oscillation Spectroscopic Survey of SDSS-III". *AJ* 145, 10. DOI: 10.1088/0004-6256/145/1/10. arXiv: 1208.0022 [astro-ph.CO].

De Angeli, F. et al. (2023). "Gaia Data Release 3. Processing and validation of BP/RP low-resolution spectral data". *A&A* 674, A2. DOI: 10.1051/0004-6361/202243680. arXiv: 2206.06143 [astro-ph.IM].

De Propris, Roberto et al. (2011). "Separating the Conjoined Red Clump in the Galactic Bulge: Kinematics and Abundances". *ApJL* 732, L36. DOI: 10.1088/2041-8205/732/2/L36. arXiv: 1104.0223 [astro-ph.GA].

de Salas, Pablo F. and A. Widmark (2021). "Dark matter local density determination: recent observations and future prospects". *Reports on Progress in Physics* 84, 104901. DOI: 10.1088/1361-6633/ac24e7. arXiv: 2012.11477 [astro-ph.GA].

de Vaucouleurs, G. and K. C. Freeman (1972). "Structure and dynamics of barred spiral galaxies, in particular of the Magellanic type". *Vistas in Astronomy* 14, 163–294. DOI: 10.1016/0083-6656(72)90026-8.

Del Nobile, Eugenio (2021). "Appendiciario – A hands-on manual on the theory of direct Dark Matter detection". *arXiv e-prints*, arXiv:2104.12785. arXiv: 2104.12785 [hep-ph].

Deng, Jia et al. (2009). "ImageNet: A large-scale hierarchical image database". In: *2009 IEEE Conference on Computer Vision and Pattern Recognition*, pp. 248–255. DOI: 10.1109/CVPR.2009.5206848.

Derriere, S. and A. C. Robin (2001). "Near-infrared Surveys and the Shape of the Galactic Disc." In: *The New Era of Wide Field Astronomy*. Ed. by Roger Clowes, Andrew Adamson, and Gordon Bromage. Vol. 232. Astronomical Society of the Pacific Conference Series, p. 229.

Drimmel, R., R. L. Smart, and M. G. Lattanzi (2000). "The Galactic warp in OB stars from Hipparcos". *A&A* 354, 67–76. arXiv: astro-ph/9912398 [astro-ph].

Drimmel, Ronald and Eloisa Poggio (2018). "On the Solar Velocity". *Research Notes of the American Astronomical Society* 2, 210. DOI: 10.3847/2515-5172/aaef8b.

Drimmel, Ronald and David N. Spergel (2001). "Three-dimensional Structure of the Milky Way Disk: The Distribution of Stars and Dust beyond 0.35 R_{solar}". *ApJ* 556, 181–202. DOI: 10.1086/321556. arXiv: astro-ph/0101259 [astro-ph].

Drlica-Wagner, A. et al. (2021). "The DECam Local Volume Exploration Survey: Overview and First Data Release". *ApJS* 256, 2. DOI: 10.3847/1538-4365/ac079d. arXiv: 2103.07476 [astro-ph.GA].

Duong, L. et al. (2018). "The GALAH survey: properties of the Galactic disc(s) in the solar neighbourhood". *MNRAS* 476, 5216–5232. DOI: 10.1093/mnras/sty525. arXiv: 1801.01514 [astro-ph.GA].

Edvardsson, B. et al. (1993). "The Chemical Evolution of the Galactic Disk - Part One - Analysis and Results". *A&A* 275, 101.

Eggen, O. J., D. Lynden-Bell, and A. R. Sandage (1962). "Evidence from the motions of old stars that the Galaxy collapsed." *ApJ* 136, 748. DOI: 10.1086/147433.

Eilers, Anna-Christina et al. (2020). "The Strength of the Dynamical Spiral Perturbation in the Galactic Disk". *ApJ* 900, 186. DOI: 10.3847/1538-4357/abac0b. arXiv: 2003.01132 [astro-ph.GA].

Eilers, Anna-Christina et al. (2022). "Stellar Abundance Maps of the Milky Way Disk". *ApJ* 928, 23. DOI: 10.3847/1538-4357/ac54ad. arXiv: 2112.03295 [astro-ph.GA].

Eisenstein, Daniel J. et al. (2011). "SDSS-III: Massive Spectroscopic Surveys of the Distant Universe, the Milky Way, and Extra-Solar Planetary Systems". *AJ* 142, 72. DOI: 10.1088/0004-6256/142/3/72. arXiv: 1101.1529 [astro-ph.IM].

El Youssoufi, Dalal et al. (2021). "Stellar substructures in the periphery of the magellanic clouds with the VISTA hemisphere survey from the red clump and other tracers". *MNRAS*. DOI: 10.1093/mnras/stab1075. arXiv: 2104.08054 [astro-ph.GA].

Evans, N. Wyn, Ciaran A. J. O'Hare, and Christopher McCabe (2019). "Refinement of the standard halo model for dark matter searches in light of the Gaia Sausage". *PhRvD* 99, 023012. DOI: 10.1103/PhysRevD.99.023012.

Feuillet, Diane K. et al. (2019). "Spatial variations in the Milky Way disc metallicity-age relation". *MNRAS* 489, 1742–1752. DOI: 10.1093/mnras/stz2221. arXiv: 1908.02772 [astro-ph.GA].

Flynn, C. and B. Fuchs (1994). "Density of dark matter in the Galactic disk". *MNRAS* 270, 471–479. DOI: 10.1093/mnras/270.3.471.

Freedman, Wendy L. et al. (2001). "Final Results from the Hubble Space Telescope Key Project to Measure the Hubble Constant". *ApJ* 553, 47–72. DOI: 10.1086/320638. arXiv: astro-ph/0012376 [astro-ph].

Freeman, Ken and Joss Bland-Hawthorn (2002). "The New Galaxy: Signatures of Its Formation". *ARA&A* 40, 487–537. DOI: 10.1146/annurev.astro.40.060401.093840. arXiv: astro-ph/0208106 [astro-ph].

Freudenreich, H. T. et al. (1994). "DIRBE Evidence for a Warp in the Interstellar Dust Layer and Stellar Disk of the Galaxy". *ApJL* 429, L69. DOI: 10.1086/187415.

Friske, Jennifer K. S. and Ralph Schönrich (2019). "More than just a wrinkle: a wave-like pattern in U_g versus L_z from Gaia data". *MNRAS* 490, 5414–5423. DOI: 10.1093/mnras/stz2951. arXiv: 1902.09569 [astro-ph.GA].

Fuhrmann, Klaus (1998). "Nearby stars of the Galactic disk and halo". *A&A* 338, 161–183.

Gaia Collaboration et al. (2016a). "The Gaia mission". *A&A* 595, A1. DOI: 10.1051/0004-6361/201629272. arXiv: 1609.04153 [astro-ph.IM].

Gaia Collaboration et al. (2016b). "The Gaia mission". *A&A* 595, A1. DOI: 10.1051/0004-6361/201629272. arXiv: 1609.04153 [astro-ph.IM].

Gaia Collaboration et al. (2018a). "Gaia Data Release 2. Mapping the Milky Way disc kinematics". *A&A* 616, A11. DOI: 10.1051/0004-6361/201832865. arXiv: 1804.09380 [astro-ph.GA].

Gaia Collaboration et al. (2018b). "Gaia Data Release 2. Mapping the Milky Way disc kinematics". *A&A* 616, A11. DOI: 10.1051/0004-6361/201832865. arXiv: 1804.09380 [astro-ph.GA].

Gaia Collaboration et al. (2018c). "Gaia Data Release 2. Observational Hertzsprung-Russell diagrams". *A&A* 616, A10. DOI: 10.1051/0004-6361/201832843. arXiv: 1804.09378 [astro-ph.SR].

Gaia Collaboration et al. (2021a). "Gaia Early Data Release 3. Structure and properties of the Magellanic Clouds". *A&A* 649, A7. DOI: 10.1051/0004-6361/202039588. arXiv: 2012.01771 [astro-ph.GA].

Gaia Collaboration et al. (2021b). "Gaia Early Data Release 3. Summary of the contents and survey properties". *A&A* 649, A1. DOI: 10.1051/0004-6361/202039657. arXiv: 2012.01533 [astro-ph.GA].

Gaia Collaboration et al. (2023). "Gaia Data Release 3. Summary of the content and survey properties". *A&A* 674, A1. DOI: 10.1051/0004-6361/202243940. arXiv: 2208.00211 [astro-ph.GA].

Garavito-Camargo, Nicolas et al. (2019). "Hunting for the Dark Matter Wake Induced by the Large Magellanic Cloud". *ApJ* 884, 51. DOI: 10.3847/1538-4357/ab32eb. arXiv: 1902.05089 [astro-ph.GA].

García Pérez, Ana E. et al. (2016). "ASPCAP: The APOGEE Stellar Parameter and Chemical Abundances Pipeline". *AJ* 151, 144. DOI: 10.3847/0004-6256/151/6/144. arXiv: 1510.07635 [astro-ph.SR].

Gilmore, G. and N. Reid (1983). "New light on faint stars - III. Galactic structure towards the South Pole and the Galactic thick disc." *MNRAS* 202, 1025–1047. DOI: 10.1093/mnras/202.4.1025.

Götberg, Y. et al. (2019). "The impact of stars stripped in binaries on the integrated spectra of stellar populations". *A&A* 629, A134. DOI: 10.1051/0004-6361/201834525. arXiv: 1908.06102 [astro-ph.GA].

Grand, Robert J. J. et al. (2018). "Aurigaia: mock Gaia DR2 stellar catalogues from the AURIGA cosmological simulations". *MNRAS* 481, 1726–1743. DOI: 10.1093/mnras/sty2403. arXiv: 1804.08549 [astro-ph.GA].

Gravity Collaboration et al. (2018a). "Detection of the gravitational redshift in the orbit of the star S2 near the Galactic centre massive black hole". *A&A* 615, L15. DOI: 10.1051/0004-6361/201833718. arXiv: 1807.09409 [astro-ph.GA].

— (2018b). "Detection of the gravitational redshift in the orbit of the star S2 near the Galactic centre massive black hole". *A&A* 615, L15. DOI: 10.1051/0004-6361/201833718. arXiv: 1807.09409 [astro-ph.GA].

Guijarro, A. et al. (2010). "Near-infrared and optical observations of galactic warps: a common, unexplained feature of most discs". *A&A* 519, A53. DOI: 10.1051/0004-6361/201014506. arXiv: 1009.2112 [astro-ph.CO].

Gunn, James E. et al. (2006). "The 2.5 m Telescope of the Sloan Digital Sky Survey". *AJ* 131, 2332–2359. DOI: 10.1086/500975. arXiv: astro-ph/0602326 [astro-ph].

Guo, Rui et al. (2020). "Measuring the local dark matter density with LAMOST DR5 and Gaia DR2". *MNRAS* 495, 4828–4844. DOI: 10.1093/mnras/staa1483. arXiv: 2005.12018 [astro-ph.GA].

Gustafsson, B. et al. (2008). "A grid of MARCS model atmospheres for late-type stars. I. Methods and general properties". *A&A* 486, 951–970. DOI: 10.1051/0004-6361:200809724. arXiv: 0805.0554 [astro-ph].

Hagen, Jorrit H. J. and Amina Helmi (2018). "The vertical force in the solar neighbourhood using red clump stars in TGAS and RAVE. Constraints on the local

dark matter density". *A&A* 615, A99. DOI: 10.1051/0004-6361/201832903. arXiv: 1802.09291 [astro-ph.GA].

Hawkins, K. et al. (2015). "Using chemical tagging to redefine the interface of the Galactic disc and halo". *MNRAS* 453, 758–774. DOI: 10.1093/mnras/stv1586. arXiv: 1507.03604 [astro-ph.GA].

Hayden, Michael R. et al. (2014). "Chemical Cartography with APOGEE: Large-scale Mean Metallicity Maps of the Milky Way Disk". *AJ* 147, 116. DOI: 10.1088/0004-6256/147/5/116. arXiv: 1311.4569 [astro-ph.GA].

Hayden, Michael R. et al. (2015). "Chemical Cartography with APOGEE: Metallicity Distribution Functions and the Chemical Structure of the Milky Way Disk". *ApJ* 808, 132. DOI: 10.1088/0004-637X/808/2/132. arXiv: 1503.02110 [astro-ph.GA].

Hayden, Michael R. et al. (2020). "The GALAH survey: chemodynamics of the solar neighbourhood". *MNRAS* 493, 2952–2964. DOI: 10.1093/mnras/staa335. arXiv: 1901.07565 [astro-ph.GA].

Hayes, Christian R. et al. (2018). "Disk-like Chemistry of the Triangulum-Andromeda Overdensity as Seen by APOGEE". *ApJL* 859, L8. DOI: 10.3847/2041-8213/aac38c. arXiv: 1805.03706 [astro-ph.GA].

He, Kaiming et al. (2016). "Deep residual learning for image recognition". In: *Proceedings of the IEEE conference on computer vision and pattern recognition*, pp. 770–778.

Henderson, A. P., P. D. Jackson, and F. J. Kerr (1982). "The distribution of neutral atomic hydrogen in our galaxy beyond the solar circle". *ApJ* 263, 116–122. DOI: 10.1086/160486.

Henon, M. (1982). "Vlasov equation". *A&A* 114, 211.

Hezaveh, Yashar D., Laurence Perreault Levasseur, and Philip J. Marshall (2017). "Fast automated analysis of strong gravitational lenses with convolutional neural networks". *Nature* 548, 555–557. DOI: 10.1038/nature23463. arXiv: 1708.08842 [astro-ph.IM].

Hill, E. R. (1960). "The component of the galactic gravitational field perpendicular to the galactic plane, K_z". *BAN* 15, 1.

Holmberg, Johan and Chris Flynn (2000). "The local density of matter mapped by Hipparcos". *MNRAS* 313, 209–216. DOI: 10.1046/j.1365-8711.2000.02905.x. arXiv: astro-ph/9812404 [astro-ph].

Holtzman, Jon A. et al. (2015). "Abundances, Stellar Parameters, and Spectra from the SDSS-III/APOGEE Survey". *AJ* 150, 148. DOI: 10.1088/0004-6256/150/5/148. arXiv: 1501.04110 [astro-ph.GA].

Holtzman, Jon A. et al. (2018). "APOGEE Data Releases 13 and 14: Data and Analysis". *AJ* 156, 125. DOI: 10.3847/1538-3881/aad4f9. arXiv: 1807.09773 [astro-ph.GA].

Huang, Y. et al. (2018). "On the Kinematic Signature of the Galactic Warp As Revealed By the LAMOST-TGAS Data". *ApJ* 864, 129. DOI: 10.3847/1538-4357/aad285. arXiv: 1807.02920 [astro-ph.GA].

Hubeny, Ivan and Thierry Lanz (2011). *Synspec: General Spectrum Synthesis Program*. Astrophysics Source Code Library, record ascl:1109.022. ascl: 1109.022.

Hunter, C. and Alar Toomre (1969). "Dynamics of the Bending of the Galaxy". *ApJ* 155, 747. DOI: 10.1086/149908.

Ibata, R. A. and A. O. Razoumov (1998). "Archer of the Galactic disk? The effect on the outer HI disk of the Milky Way of collisional encounters with the Sagittarius dwarf galaxy". *A&A* 336, 130–136. arXiv: astro-ph/9806132 [astro-ph].

Ivezić, Željko, Timothy C. Beers, and Mario Jurić (2012). "Galactic Stellar Populations in the Era of the Sloan Digital Sky Survey and Other Large Surveys". *ARA&A* 50, 251–304. DOI: 10.1146/annurev-astro-081811-125504. arXiv: 1308.6386 [astro-ph.GA].

Ivezić, Željko et al. (2019). "LSST: From Science Drivers to Reference Design and Anticipated Data Products". *ApJ* 873, 111. DOI: 10.3847/1538-4357/ab042c. arXiv: 0805.2366 [astro-ph].

Jacobs, C. et al. (2017). "Finding strong lenses in CFHTLS using convolutional neural networks". *MNRAS* 471, 167–181. DOI: 10.1093/mnras/stx1492. arXiv: 1704.02744 [astro-ph.IM].

Jaiswal, Ashish et al. (2020). "A survey on contrastive self-supervised learning". *Technologies* 9, 2.

Jeans, J. H. (1915). "On the theory of star-streaming and the structure of the universe". *MNRAS* 76, 70–84. DOI: 10.1093/mnras/76.2.70.

Jenkins, Adrian and James Binney (1990). "Spiral heating of galactic discs". *MNRAS* 245, 305–317.

Jönsson, Henrik et al. (2020). "APOGEE Data and Spectral Analysis from SDSS Data Release 16: Seven Years of Observations Including First Results from APOGEE-South". *AJ* 160, 120. DOI: 10.3847/1538-3881/aba592. arXiv: 2007.05537 [astro-ph.GA].

Jurić, Mario et al. (2008). "The Milky Way Tomography with SDSS. I. Stellar Number Density Distribution". *ApJ* 673, 864–914. DOI: 10.1086/523619. arXiv: astro-ph/0510520 [astro-ph].

Kallivayalil, Nitya et al. (2006). "The Proper Motion of the Large Magellanic Cloud Using HST". *ApJ* 638, 772–785. DOI: 10.1086/498972. arXiv: astro-ph/0508457 [astro-ph].

Kallivayalil, Nitya et al. (2013). "Third-epoch Magellanic Cloud Proper Motions. I. Hubble Space Telescope/WFC3 Data and Orbit Implications". *ApJ* 764, 161. DOI: 10.1088/0004-637X/764/2/161. arXiv: 1301.0832 [astro-ph.CO].

Kalomeni, B. et al. (2016). "Evolution of Cataclysmic Variables and Related Binaries Containing a White Dwarf". *ApJ* 833, 83. DOI: 10.3847/1538-4357/833/1/83. arXiv: 1610.03051 [astro-ph.SR].

Kapteyn, J. C. (1922). "First Attempt at a Theory of the Arrangement and Motion of the Sidereal System". *ApJ* 55, 302. DOI: 10.1086/142670.

Katz, D. et al. (2023). "Gaia Data Release 3. Properties and validation of the radial velocities". *A&A* 674, A5. DOI: 10.1051/0004-6361/202244220. arXiv: 2206.05902 [astro-ph.GA].

Kawata, Daisuke et al. (2018). "Radial distribution of stellar motions in Gaia DR2". *MNRAS* 479, L108–L112. DOI: 10.1093/mnrasl/sly107. arXiv: 1804.10175 [astro-ph.GA].

Kazantzidis, Stelios et al. (2008). "Cold Dark Matter Substructure and Galactic Disks. I. Morphological Signatures of Hierarchical Satellite Accretion". *ApJ* 688, 254–276. DOI: 10.1086/591958. arXiv: 0708.1949 [astro-ph].

Kerr, F. J. (1957). "A Magellanic effect on the galaxy." *AJ* 62, 93–93. DOI: 10.1086/107466.

Kingma, Diederik P and Jimmy Ba (2014). "Adam: A method for stochastic optimization". *arXiv preprint arXiv:1412.6980*.

Klypin, Anatoly, HongSheng Zhao, and Rachel S. Somerville (2002). "ΛCDM-based Models for the Milky Way and M31. I. Dynamical Models". *ApJ* 573, 597–613. DOI: 10.1086/340656. arXiv: astro-ph/0110390 [astro-ph].

Kochanek, C. S. et al. (2017). "The All-Sky Automated Survey for Supernovae (ASAS-SN) Light Curve Server v1.0". *PASP* 129, 104502. DOI: 10.1088/1538-3873/aa80d9. arXiv: 1706.07060 [astro-ph.SR].

Kollmeier, Juna A. et al. (2017). "SDSS-V: Pioneering Panoptic Spectroscopy". *arXiv e-prints*, arXiv:1711.03234. DOI: 10.48550/arXiv.1711.03234. arXiv: 1711.03234 [astro-ph.GA].

Kuijken, K. and G. Gilmore (1989a). "The mass distribution in the galactic disc -III. The local volume mass density." *MNRAS* 239, 651–664. DOI: 10.1093/mnras/239.2.651.

Kuijken, Konrad and Gerard Gilmore (1989b). "The mass distribution in the galactic disc. I - A technique to determine the integral surface mass density of the disc near the sun." *MNRAS* 239, 571–603. DOI: 10.1093/mnras/239.2.571.

Lake, George (1989). "Must the Disk and Halo Dark Matter Be Different?" *AJ* 98, 1554. DOI: 10.1086/115238.

Lamberts, Astrid et al. (2019). "Predicting the LISA white dwarf binary population in the Milky Way with cosmological simulations". *MNRAS* 490, 5888–5903. DOI: 10.1093/mnras/stz2834. arXiv: 1907.00014 [astro-ph.HE].

Laporte, Chervin F. P. et al. (2018). "The influence of Sagittarius and the Large Magellanic Cloud on the stellar disc of the Milky Way Galaxy". *MNRAS* 481, 286–306. DOI: 10.1093/mnras/sty1574. arXiv: 1710.02538 [astro-ph.GA].

Laporte, Chervin F. P. et al. (2019). "Footprints of the Sagittarius dwarf galaxy in the Gaia data set". *MNRAS* 485, 3134–3152. DOI: 10.1093/mnras/stz583. arXiv: 1808.00451 [astro-ph.GA].

Law, David R., Steven R. Majewski, and Kathryn V. Johnston (2009). "Evidence for a Triaxial Milky Way Dark Matter Halo from the Sagittarius Stellar Tidal Stream".

ApJL 703, L67–L71. DOI: 10.1088/0004-637X/703/1/L67. arXiv: 0908.3187 [astro-ph.GA].

Law, Nicholas M. et al. (2012). "Three New Eclipsing White-dwarf-M-dwarf Binaries Discovered in a Search for Transiting Planets around M-dwarfs". *ApJ* 757, 133. DOI: 10.1088/0004-637X/757/2/133. arXiv: 1112.1701 [astro-ph.SR].

Levine, E. S., Leo Blitz, and Carl Heiles (2006). "The Vertical Structure of the Outer Milky Way H I Disk". *ApJ* 643, 881–896. DOI: 10.1086/503091. arXiv: astro-ph/0601697 [astro-ph].

Li, Ting S. et al. (2017). "Exploring Halo Substructure with Giant Stars. XV. Discovery of a Connection between the Monoceros Ring and the Triangulum-Andromeda Overdensity?" *ApJ* 844, 74. DOI: 10.3847/1538-4357/aa7a0d. arXiv: 1703.05384 [astro-ph.GA].

Li, X. -Y. et al. (2020). "Mapping the Galactic Disk with the LAMOST and Gaia Red Clump Sample. IV. The Kinematic Signature of the Galactic Warp". *ApJ* 901, 56. DOI: 10.3847/1538-4357/aba61e. arXiv: 2007.06947 [astro-ph.GA].

Li, Zhao-Yu (2021). "Vertical Phase Mixing across the Galactic Disk". *ApJ* 911, 107. DOI: 10.3847/1538-4357/abea17. arXiv: 2011.11250 [astro-ph.GA].

Lian, Jianhui et al. (2022). "The Milky Way tomography with APOGEE: intrinsic density distribution and structure of mono-abundance populations". *MNRAS* 513, 4130–4151. DOI: 10.1093/mnras/stac1151. arXiv: 2204.10327 [astro-ph.GA].

Lindegren, L. et al. (2018). "Gaia Data Release 2. The astrometric solution". *A&A* 616, A2. DOI: 10.1051/0004-6361/201832727. arXiv: 1804.09366 [astro-ph.IM].

Liu, Xiao et al. (2021). "Self-supervised learning: Generative or contrastive". *IEEE transactions on knowledge and data engineering* 35, 857–876.

Lochner, Michelle et al. (2016). "Photometric Supernova Classification with Machine Learning". *ApJS* 225, 31. DOI: 10.3847/0067-0049/225/2/31. arXiv: 1603.00882 [astro-ph.IM].

López-Corredoira, M. et al. (2014). "Vertical velocities from proper motions of red clump giants". *A&A* 572, A101. DOI: 10.1051/0004-6361/201424573. arXiv: 1409.6222 [astro-ph.GA].

López-Corredoira, M. et al. (2020). "Gaia-DR2 extended kinematical maps. II. Dynamics in the Galactic disk explaining radial and vertical velocities". *A&A* 634, A66. DOI: 10.1051/0004-6361/201936711. arXiv: 2001.05455 [astro-ph.GA].

Mackereth, J. Ted et al. (2017). "The age-metallicity structure of the Milky Way disc using APOGEE". *MNRAS* 471, 3057–3078. DOI: 10.1093/mnras/stx1774. arXiv: 1706.00018 [astro-ph.GA].

Mackereth, J. Ted et al. (2019). "The origin of accreted stellar halo populations in the Milky Way using APOGEE, Gaia, and the EAGLE simulations". *MNRAS* 482, 3426–3442. DOI: 10.1093/mnras/sty2955. arXiv: 1808.00968 [astro-ph.GA].

Mackey, A. D. et al. (2016). "A 10 kpc stellar substructure at the edge of the Large Magellanic Cloud: perturbed outer disc or evidence for tidal stripping?" *MNRAS* 459, 239–255. DOI: 10.1093/mnras/stw497. arXiv: 1508.01356 [astro-ph.GA].

Mackey, Dougal et al. (2018). "Substructures and Tidal Distortions in the Magellanic Stellar Periphery". *ApJL* 858, L21. DOI: 10.3847/2041-8213/aac175. arXiv: 1804.06431 [astro-ph.GA].

Majewski, S. R. (1993). "Galactic structure surveys and the evolution of the Milky Way." *ARA&A* 31, 575–638. DOI: 10.1146/annurev.aa.31.090193.003043.

Majewski, Steven R. et al. (2003). "A Two Micron All Sky Survey View of the Sagittarius Dwarf Galaxy. I. Morphology of the Sagittarius Core and Tidal Arms". *ApJ* 599, 1082–1115. DOI: 10.1086/379504. arXiv: astro-ph/0304198 [astro-ph].

Majewski, Steven R. et al. (2004). "Detection of the Main-Sequence Turnoff of a Newly Discovered Milky Way Halo Structure in the Triangulum-Andromeda Region". *ApJ* 615, 738–743. DOI: 10.1086/424586. arXiv: astro-ph/0406221 [astro-ph].

Majewski, Steven R. et al. (2009). "Discovery of an extended, halo-like stellar population around the Large Magellanic Cloud". In: *The Magellanic System: Stars, Gas, and Galaxies*. Ed. by Jacco Th. Van Loon and Joana M. Oliveira. Vol. 256, pp. 51–56. DOI: 10.1017/S1743921308028251.

Majewski, Steven R. et al. (2017). "The Apache Point Observatory Galactic Evolution Experiment (APOGEE)". *AJ* 154, 94. DOI: 10.3847/1538-3881/aa784d. arXiv: 1509.05420 [astro-ph.IM].

Marquez, A. and W. J. Schuster (1994). "Uvby-β photometry of high-velocity and metal-poor stars. VII. Ages of halo and thick-disk field stars." *A&AS* 108, 341–358.

Marshall, D. J. et al. (2006). "Modelling the Galactic interstellar extinction distribution in three dimensions". *A&A* 453, 635–651. DOI: 10.1051/0004-6361:20053842. arXiv: astro-ph/0604427 [astro-ph].

Martínez-Delgado, David et al. (2019). "Nature of a shell of young stars in the outskirts of the Small Magellanic Cloud". *A&A* 631, A98. DOI: 10.1051/0004-6361/201936021. arXiv: 1907.02264 [astro-ph.GA].

Masci, Frank J. et al. (2019). "The Zwicky Transient Facility: Data Processing, Products, and Archive". *PASP* 131, 018003. DOI: 10.1088/1538-3873/aae8ac. arXiv: 1902.01872 [astro-ph.IM].

Masseron, T. and G. Gilmore (2015). "Carbon, nitrogen and α-element abundances determine the formation sequence of the Galactic thick and thin discs". *MNRAS* 453, 1855–1866. DOI: 10.1093/mnras/stv1731. arXiv: 1503.00537 [astro-ph.SR].

McKee, Christopher F., Antonio Parravano, and David J. Hollenbach (2015). "Stars, Gas, and Dark Matter in the Solar Neighborhood". *ApJ* 814, 13. DOI: 10.1088/0004-637X/814/1/13. arXiv: 1509.05334 [astro-ph.GA].

Mihalas, D. and J. Binney (1981). *Galactic astronomy. Structure and kinematics*.

Miyamoto, M., M. Yoshizawa, and S. Suzuki (1988). "An optical warp of the Galaxy". *A&A* 194, 107–115.

Möller, A. and T. de Boissière (2020). "SuperNNova: an open-source framework for Bayesian, neural network-based supernova classification". *MNRAS* 491, 4277–4293. DOI: 10.1093/mnras/stz3312. arXiv: 1901.06384 [astro-ph.IM].

Moni Bidin, C. et al. (2012). "Kinematical and Chemical Vertical Structure of the Galactic Thick Disk. II. A Lack of Dark Matter in the Solar Neighborhood". *ApJ* 751, 30. DOI: 10.1088/0004-637X/751/1/30. arXiv: 1204.3924 [astro-ph.GA].

Moni Bidin, C. et al. (2015). "On the local dark matter density". *A&A* 573, A91. DOI: 10.1051/0004-6361/201424675.

Muñoz, César et al. (2023). "Chemo-dynamical tagging in the outskirts: The origins of stellar substructures in the Magellanic Clouds". *A&A* 680, A79. DOI: 10.1051/0004-6361/202347046. arXiv: 2305.19460 [astro-ph.GA].

Navarro, Julio F., Carlos S. Frenk, and Simon D. M. White (1997). "A Universal Density Profile from Hierarchical Clustering". *ApJ* 490, 493–508. DOI: 10.1086/304888. arXiv: astro-ph/9611107 [astro-ph].

Newberg, Heidi Jo and Yan Xu (2017). "The Vertical Displacement of the Milky Way Disk". In: *Formation and Evolution of Galaxy Outskirts*. Ed. by Armando Gil de Paz, Johan H. Knapen, and Janice C. Lee. Vol. 321. IAU Symposium, pp. 13–15. DOI: 10.1017/S1743921316011121. arXiv: 1708.03680 [astro-ph.GA].

Newberg, Heidi Jo et al. (2002). "The Ghost of Sagittarius and Lumps in the Halo of the Milky Way". *ApJ* 569, 245–274. DOI: 10.1086/338983. arXiv: astro-ph/0111095 [astro-ph].

Nidever, David L., Steven R. Majewski, and W. Butler Burton (2008). "The Origin of the Magellanic Stream and Its Leading Arm". *ApJ* 679, 432–459. DOI: 10.1086/587042.

Nidever, David L. et al. (2015). "The Data Reduction Pipeline for the Apache Point Observatory Galactic Evolution Experiment". *AJ* 150, 173. DOI: 10.1088/0004-6256/150/6/173. arXiv: 1501.03742 [astro-ph.IM].

Nidever, David L. et al. (2017). "SMASH: Survey of the MAgellanic Stellar History". *AJ* 154, 199. DOI: 10.3847/1538-3881/aa8d1c. arXiv: 1701.00502 [astro-ph.GA].

Nidever, David L. et al. (2020). "The Lazy Giants: APOGEE Abundances Reveal Low Star Formation Efficiencies in the Magellanic Clouds". *ApJ* 895, 88. DOI: 10.3847/1538-4357/ab7305. arXiv: 1901.03448 [astro-ph.GA].

Nitschai, Maria Selina et al. (2021). "Dynamical Model of the Milky Way Using APOGEE and Gaia Data". *ApJ* 916, 112. DOI: 10.3847/1538-4357/ac04b5. arXiv: 2106.05286 [astro-ph.GA].

Norris, John (1987). "Population Studies: The Nature of the Thick Disk". *ApJL* 314, L39. DOI: 10.1086/184847.

Norris, John E. and Sean G. Ryan (1989). "Population Studies. VII. On the Use of UBV Data for Kinematically Selected Samples to Determine the Dependence of Kinematics on Abundance". *ApJ* 340, 739. DOI: 10.1086/167434.

Okabe, Nobuhiro et al. (2013). "LoCuSS: The Mass Density Profile of Massive Galaxy Clusters at z = 0.2". *ApJL* 769, L35. DOI: 10.1088/2041-8205/769/2/L35. arXiv: 1302.2728 [astro-ph.CO].

Olsen, K. A. G. and C. Salyk (2002). "A Warp in the Large Magellanic Cloud Disk?" *AJ* 124, 2045–2053. DOI: 10.1086/342739.

Olsen, Knut A. G. et al. (2011). "A Population of Accreted Small Magellanic Cloud Stars in the Large Magellanic Cloud". *ApJ* 737, 29. DOI: 10.1088/0004-637X/737/1/29. arXiv: 1106.0044 [astro-ph.GA].

Oort, J. H. (1932). "The force exerted by the stellar system in the direction perpendicular to the galactic plane and some related problems". *BAN* 6, 249.

Osorio, Y. et al. (2020). "NLTE for APOGEE: simultaneous multi-element NLTE radiative transfer". *A&A* 637, A80. DOI: 10.1051/0004-6361/201937054. arXiv: 2003.13353 [astro-ph.SR].

Ostriker, E. C. and J. J. Binney (1989). "Warped and tilted galactic discs". *MNRAS* 237, 785–798. DOI: 10.1093/mnras/237.3.785.

Palicio, Pedro A. et al. (2018). "Signatures of the Galactic bar on stellar kinematics unveiled by APOGEE". *MNRAS* 478, 1231–1243. DOI: 10.1093/mnras/sty1156. arXiv: 1805.04347 [astro-ph.GA].

Panithanpaisal, Nondh and Robyn Sanderson (2023). "Understanding the Milky Way: What Can We Learn from Tidal Streams?" In: *American Astronomical Society Meeting Abstracts*. Vol. 55. American Astronomical Society Meeting Abstracts, 228.04D, p. 228.04D.

Pasetto, S. et al. (2012a). "Thick disk kinematics from RAVE and the solar motion". *A&A* 547, A70. DOI: 10.1051/0004-6361/201219464. arXiv: 1209.0456 [astro-ph.GA].

— (2012b). "Thin disk kinematics from RAVE and the solar motion". *A&A* 547, A71. DOI: 10.1051/0004-6361/201219462. arXiv: 1209.0460 [astro-ph.GA].

Peñarrubia, J. et al. (2005). "A Comprehensive Model for the Monoceros Tidal Stream". *ApJ* 626, 128–144. DOI: 10.1086/429903. arXiv: astro-ph/0410448 [astro-ph].

Perryman, M. A. C. et al. (1997). "The HIPPARCOS Catalogue". *A&A* 323, L49–L52.

Petrillo, C. E. et al. (2017). "Finding strong gravitational lenses in the Kilo Degree Survey with Convolutional Neural Networks". *MNRAS* 472, 1129–1150. DOI: 10.1093/mnras/stx2052. arXiv: 1702.07675 [astro-ph.GA].

Pieres, A. et al. (2017). "A stellar overdensity associated with the Small Magellanic Cloud". *MNRAS* 468, 1349–1360. DOI: 10.1093/mnras/stx507. arXiv: 1612.03938 [astro-ph.GA].

Pietrzyński, G. et al. (2019). "A distance to the Large Magellanic Cloud that is precise to one per cent". *Nature* 567, 200–203. DOI: 10.1038/s41586-019-0999-4. arXiv: 1903.08096 [astro-ph.GA].

Piffl, T. et al. (2014). "Constraining the Galaxy's dark halo with RAVE stars". *MNRAS* 445, 3133–3151. DOI: 10.1093/mnras/stu1948. arXiv: 1406.4130 [astro-ph.GA].

Pinsonneault, Marc H. et al. (2014). "The APOKASC Catalog: An Asteroseismic and Spectroscopic Joint Survey of Targets in the Kepler Fields". *ApJS* 215, 19. DOI: 10.1088/0067-0049/215/2/19. arXiv: 1410.2503 [astro-ph.SR].

Pinsonneault, Marc H. et al. (2018). "The Second APOKASC Catalog: The Empirical Approach". *ApJS* 239, 32. DOI: 10.3847/1538-4365/aaebfd. arXiv: 1804.09983 [astro-ph.SR].

Poggio, E. et al. (2018). "The Galactic warp revealed by Gaia DR2 kinematics". *MNRAS* 481, L21–L25. DOI: 10.1093/mnrasl/sly148. arXiv: 1805.03171 [astro-ph.GA].

Poggio, E. et al. (2020). "Evidence of a dynamically evolving Galactic warp". *Nature Astronomy* 4, 590–596. DOI: 10.1038/s41550-020-1017-3. arXiv: 1912.10471 [astro-ph.GA].

Portail, Matthieu et al. (2017). "Dynamical modelling of the galactic bulge and bar: the Milky Way's pattern speed, stellar and dark matter mass distribution". *MNRAS* 465, 1621–1644. DOI: 10.1093/mnras/stw2819. arXiv: 1608.07954 [astro-ph.GA].

Posti, Lorenzo and Amina Helmi (2019). "Mass and shape of the Milky Way's dark matter halo with globular clusters from Gaia and Hubble". *A&A* 621, A56. DOI: 10.1051/0004-6361/201833355. arXiv: 1805.01408 [astro-ph.GA].

Purcell, Chris W., James S. Bullock, and Manoj Kaplinghat (2009). "The Dark Disk of the Milky Way". *ApJ* 703, 2275–2284. DOI: 10.1088/0004-637X/703/2/2275. arXiv: 0906.5348 [astro-ph.GA].

Queiroz, A. B. A. et al. (2018). "StarHorse: a Bayesian tool for determining stellar masses, ages, distances, and extinctions for field stars". *MNRAS* 476, 2556–2583. DOI: 10.1093/mnras/sty330. arXiv: 1710.09970 [astro-ph.IM].

Queiroz, A. B. A. et al. (2020). "From the bulge to the outer disc: StarHorse stellar parameters, distances, and extinctions for stars in APOGEE DR16 and other spectroscopic surveys". *A&A* 638, A76. DOI: 10.1051/0004-6361/201937364. arXiv: 1912.09778 [astro-ph.GA].

Read, J. I. (2014). "The local dark matter density". *Journal of Physics G Nuclear Physics* 41, 063101. DOI: 10.1088/0954-3899/41/6/063101. arXiv: 1404.1938 [astro-ph.GA].

Read, J. I. et al. (2008). "Thin, thick and dark discs in ΛCDM". *MNRAS* 389, 1041–1057. DOI: 10.1111/j.1365-2966.2008.13643.x. arXiv: 0803.2714 [astro-ph].

Rebassa-Mansergas, A. et al. (2012). "Post-common envelope binaries from SDSS - XVI. Long orbital period systems and the energy budget of common envelope evolution". *MNRAS* 423, 320–327. DOI: 10.1111/j.1365-2966.2012.20880.x. arXiv: 1203.1208 [astro-ph.SR].

Recio-Blanco, A. et al. (2023). "Gaia Data Release 3. Analysis of RVS spectra using the General Stellar Parametriser from spectroscopy". *A&A* 674, A29. DOI: 10.1051/0004-6361/202243750. arXiv: 2206.05541 [astro-ph.GA].

Reddy, Bacham E., David L. Lambert, and Carlos Allende Prieto (2006). "Elemental abundance survey of the Galactic thick disc". *MNRAS* 367, 1329–1366. DOI: 10.1111/j.1365-2966.2006.10148.x. arXiv: astro-ph/0512505 [astro-ph].

Reid, M. J. and A. Brunthaler (2004). "The Proper Motion of Sagittarius A*. II. The Mass of Sagittarius A*". *ApJ* 616, 872–884. DOI: 10.1086/424960. arXiv: astro-ph/0408107 [astro-ph].

Reid, M. J. et al. (2014). "Trigonometric Parallaxes of High Mass Star Forming Regions: The Structure and Kinematics of the Milky Way". *ApJ* 783, 130. DOI: 10.1088/0004-637X/783/2/130. arXiv: 1401.5377 [astro-ph.GA].

Ren, J. -J. et al. (2018). "White dwarf-main sequence binaries from LAMOST: the DR5 catalogue". *MNRAS* 477, 4641–4654. DOI: 10.1093/mnras/sty805. arXiv: 1803.09523 [astro-ph.SR].

Reylé, C. et al. (2009). "The Milky Way's external disc constrained by 2MASS star counts". *A&A* 495, 819–826. DOI: 10.1051/0004-6361/200811341. arXiv: 0812.3739 [astro-ph].

Richter, O. -G. and R. Sancisi (1994). "Asymmetries in disk galaxies. How often? How strong?" *A&A* 290, L9–L12.

Ricker, George R. et al. (2015). "Transiting Exoplanet Survey Satellite (TESS)". *Journal of Astronomical Telescopes, Instruments, and Systems* 1, 014003. DOI: 10.1117/1.JATIS.1.1.014003.

Rocha-Pinto, Helio J. et al. (2004). "Exploring Halo Substructure with Giant Stars: A Diffuse Star Cloud or Tidal Debris around the Milky Way in Triangulum-Andromeda". *ApJ* 615, 732–737. DOI: 10.1086/424585. arXiv: astro-ph/0405437 [astro-ph].

Romero-Gómez, M. et al. (2019). "Gaia kinematics reveal a complex lopsided and twisted Galactic disc warp". *A&A* 627, A150. DOI: 10.1051/0004-6361/201834908. arXiv: 1812.07576 [astro-ph.GA].

Sales Silva, J. V. et al. (2019). "Triangulum Andromeda Overdensity: a Region with a Complex Stellar Population". *ApJ* 886, 113. DOI: 10.3847/1538-4357/ab4ada. arXiv: 1910.06457 [astro-ph.GA].

Sánchez-Salcedo, F. J., Chris Flynn, and A. M. Hidalgo-Gámez (2011). "On the Vertical Equilibrium of the Local Galactic Disk and the Search for Disk Dark Matter". *ApJL* 731, L35. DOI: 10.1088/2041-8205/731/2/L35. arXiv: 1103.4356 [astro-ph.GA].

Sanders, Jason L. and James Binney (2015). "Extended distribution functions for our Galaxy". *MNRAS* 449, 3479–3502. DOI: 10.1093/mnras/stv578. arXiv: 1501.02227 [astro-ph.GA].

Sanders, Jason L. and Payel Das (2018). "Isochrone ages for˜3 million stars with the second Gaia data release". *MNRAS* 481, 4093–4110. DOI: 10.1093/mnras/sty2490. arXiv: 1806.02324 [astro-ph.GA].

Santiago, Basílio X. et al. (2016). "Spectro-photometric distances to stars: A general purpose Bayesian approach". *A&A* 585, A42. DOI: 10.1051/0004-6361/201323177. arXiv: 1501.05500 [astro-ph.IM].

Scaringi, S. et al. (2023). "Cataclysmic variables are a key population of gravitational wave sources for LISA". *MNRAS* 525, L50–L55. DOI: 10.1093/mnrasl/slad093. arXiv: 2307.02553 [astro-ph.HE].

Schlafly, Edward F. and Douglas P. Finkbeiner (2011). "Measuring Reddening with Sloan Digital Sky Survey Stellar Spectra and Recalibrating SFD". *ApJ* 737, 103. DOI: 10.1088/0004-637X/737/2/103. arXiv: 1012.4804 [astro-ph.GA].

Schonhut-Stasik, Jessica et al. (2024). "The APO-K2 Catalog. I. 7500 Red Giants with Fundamental Stellar Parameters from APOGEE DR17 Spectroscopy and K2-GAP Asteroseismology". *AJ* 167, 50. DOI: 10.3847/1538-3881/ad0b13. arXiv: 2304.10654 [astro-ph.SR].

Schönrich, Ralph and Walter Dehnen (2018). "Warp, waves, and wrinkles in the Milky Way". *MNRAS* 478, 3809–3824. DOI: 10.1093/mnras/sty1256. arXiv: 1712.06616 [astro-ph.GA].

Schulz, A. E. et al. (2013). "Gravitational collapse in one dimension". *MNRAS* 431, 49–62. DOI: 10.1093/mnras/stt073. arXiv: 1206.0299 [astro-ph.CO].

Searle, L. and R. Zinn (1978). "Composition of halo clusters and the formation of the galactic halo." *ApJ* 225, 357–379. DOI: 10.1086/156499.

Sellwood, J. A. (2013). "Dynamics of Disks and Warps". In: *Planets, Stars and Stellar Systems. Volume 5: Galactic Structure and Stellar Populations*. Ed. by Terry D. Oswalt and Gerard Gilmore. Vol. 5, p. 923. DOI: 10.1007/978-94-007-5612-0_18.

Sharma, Sanjib et al. (2010). "Group Finding in the Stellar Halo Using M-giants in the Two Micron All Sky Survey: An Extended View of the Pisces Overdensity?" *ApJ* 722, 750–759. DOI: 10.1088/0004-637X/722/1/750. arXiv: 1009.0924 [astro-ph.GA].

Sharma, Sanjib et al. (2021). "Fundamental relations for the velocity dispersion of stars in the Milky Way". *MNRAS* 506, 1761–1776. DOI: 10.1093/mnras/stab1086. arXiv: 2004.06556 [astro-ph.GA].

Shaviv, Nir J., Andreas Prokoph, and Ján Veizer (2014). "Is the Solar System's Galactic Motion Imprinted in the Phanerozoic Climate?" *Scientific Reports* 4, 6150. DOI: 10.1038/srep06150.

Sheffield, Allyson A. et al. (2014). "Exploring Halo Substructure with Giant Stars. XIV. The Nature of the Triangulum-Andromeda Stellar Features". *ApJ* 793, 62. DOI: 10.1088/0004-637X/793/1/62. arXiv: 1407.4463 [astro-ph.GA].

Shih, David et al. (2022). "VIA MACHINAE: Searching for stellar streams using unsupervised machine learning". *MNRAS* 509, 5992–6007. DOI: 10.1093/mnras/stab3372. arXiv: 2104.12789 [astro-ph.GA].

Siebert, A. et al. (2012). "The properties of the local spiral arms from RAVE data: two-dimensional density wave approach". *MNRAS* 425, 2335–2342. DOI: 10.1111/j.1365-2966.2012.21638.x. arXiv: 1207.0363 [astro-ph.GA].

Siegel, M. H. et al. (2002). "Star Counts Redivivus. IV. Density Laws through Photometric Parallaxes". *ApJ* 578, 151–175. DOI: 10.1086/342469. arXiv: astro-ph/0206323 [astro-ph].

Silva, J. V. Sales et al. (2020). "The Abundance Pattern of α Elements in the Triangulum-Andromeda Overdensity". *ApJ* 901, 27. DOI: 10.3847/1538-4357/abaaad. arXiv: 2007.15764 [astro-ph.GA].

Skowron, Dorota M. et al. (2019). "A three-dimensional map of the Milky Way using classical Cepheid variable stars". *Science* 365, 478–482. DOI: 10.1126/science.aau3181. arXiv: 1806.10653 [astro-ph.GA].

Skrutskie, M. F. et al. (2006). "The Two Micron All Sky Survey (2MASS)". *AJ* 131, 1163–1183. DOI: 10.1086/498708.

Smith, Verne V. et al. (2021). "The APOGEE Data Release 16 Spectral Line List". *AJ* 161, 254. DOI: 10.3847/1538-3881/abefdc. arXiv: 2103.10112 [astro-ph.SR].

Sollima, A. et al. (2011). "A Deep View of the Monoceros Ring in the Anticenter Direction: Clues of Its Extra-galactic Origin". *ApJL* 730, L6. DOI: 10.1088/2041-8205/730/1/L6. arXiv: 1102.2137 [astro-ph.GA].

Sparke, Linda S. and Stefano Casertano (1988). "A model for persistent galactic warps." *MNRAS* 234, 873–898. DOI: 10.1093/mnras/234.4.873.

Spicker, J. and J. V. Feitzinger (1986). "Are there typical corrugation scales in our Galaxy ?" *A&A* 163, 43–55.

Sullivan, Devin P et al. (2018). "Deep learning is combined with massive-scale citizen science to improve large-scale image classification". *Nature biotechnology* 36, 820–828.

The Dark Energy Survey Collaboration (2005). "The Dark Energy Survey". *arXiv e-prints*, astro–ph/0510346. arXiv: astro-ph/0510346 [astro-ph].

Toloza, Odette et al. (2019). "Understanding the evolution of close white dwarf binaries". *BAAS* 51, 168. arXiv: 1903.04612 [astro-ph.SR].

Tremaine, Scott, Neige Frankel, and Jo Bovy (2023). "The origin and fate of the Gaia phase-space snail". *MNRAS* 521, 114–123. DOI: 10.1093/mnras/stad577. arXiv: 2212.11990 [astro-ph.GA].

Tyson, J. Anthony et al. (1998). "Deep Optical Imaging of the Bright Seyfert Galaxy NGC 5548: A Long, Very Low Surface Brightness Tail". *AJ* 116, 102–110. DOI: 10.1086/300395.

van der Marel, Roeland P. and Maria-Rosa L. Cioni (2001). "Magellanic Cloud Structure from Near-Infrared Surveys. I. The Viewing Angles of the Large Magellanic Cloud". *AJ* 122, 1807–1826. DOI: 10.1086/323099. arXiv: astro-ph/0105339 [astro-ph].

van der Marel, Roeland P. et al. (2002). "New Understanding of Large Magellanic Cloud Structure, Dynamics, and Orbit from Carbon Star Kinematics". *AJ* 124, 2639–2663. DOI: 10.1086/343775. arXiv: astro-ph/0205161 [astro-ph].

Vinyals, Oriol et al. (2016). "Matching networks for one shot learning". *Advances in neural information processing systems* 29.

Voskes, Tom and W. Butler Burton (2006). "The Warped HI Layer of the Outer Galaxy". *arXiv e-prints*, astro–ph/0601653. arXiv: astro-ph/0601653 [astro-ph].

Walo-Martín, Daniel et al. (2022). "Local variations of the stellar velocity ellipsoid - II. The effect of the bar in the inner regions of Auriga galaxies". *MNRAS* 513, 4587–4604. DOI: 10.1093/mnras/stac769. arXiv: 2203.07288 [astro-ph.GA].

Wang, H. -F. et al. (2020). "Mapping the Galactic Disk with the LAMOST and Gaia Red Clump Sample. VI. Evidence for the Long-lived Nonsteady Warp of Nongravitational Scenarios". *ApJ* 897, 119. DOI: 10.3847/1538-4357/ab93ad. arXiv: 2004.06600 [astro-ph.GA].

Weaver, H. (1974). "Space distribution and motion of the local H I gas". *Highlights of Astronomy* 3, 423–438.

Weber, M. and W. de Boer (2010). "Determination of the local dark matter density in our Galaxy". *A&A* 509, A25. DOI: 10.1051/0004-6361/200913381. arXiv: 0910.4272 [astro-ph.CO].

Weinberg, Martin D. and Leo Blitz (2006). "A Magellanic Origin for the Warp of the Galaxy". *ApJL* 641, L33–L36. DOI: 10.1086/503607. arXiv: astro-ph/0601694 [astro-ph].

Westerhout, G. (1957). "The distribution of atomic hydrogen in the outer parts of the Galactic System". *BAN* 13, 201.

Widmark, A. et al. (2021). "Weighing the Galactic disk using phase-space spirals. II. Most stringent constraints on a thin dark disk using Gaia EDR3". *A&A* 653, A86. DOI: 10.1051/0004-6361/202141466. arXiv: 2105.14030 [astro-ph.GA].

Widrow, Lawrence M. et al. (2012). "Galactoseismology: Discovery of Vertical Waves in the Galactic Disk". *ApJL* 750, L41. DOI: 10.1088/2041-8205/750/2/L41. arXiv: 1203.6861 [astro-ph.GA].

Widrow, Lawrence M. et al. (2014). "Bending and breathing modes of the Galactic disc". *MNRAS* 440, 1971–1981. DOI: 10.1093/mnras/stu396. arXiv: 1404.4069 [astro-ph.GA].

Willett, Kyle W. et al. (2013). "Galaxy Zoo 2: detailed morphological classifications for 304 122 galaxies from the Sloan Digital Sky Survey". *MNRAS* 435, 2835–2860. DOI: 10.1093/mnras/stt1458. arXiv: 1308.3496 [astro-ph.CO].

Wilson, J. C. et al. (2019). "The Apache Point Observatory Galactic Evolution Experiment (APOGEE) Spectrographs". *PASP* 131, 055001. DOI: 10.1088/1538-3873/ab0075. arXiv: 1902.00928 [astro-ph.IM].

Wouterloot, J. G. A. et al. (1990). "IRAS sources beyond the solar circle. II. Distribution in the galactic warp." *A&A* 230, 21–36.

Wright, Edward L. et al. (2010). "The Wide-field Infrared Survey Explorer (WISE): Mission Description and Initial On-orbit Performance". *AJ* 140, 1868–1881. DOI: 10.1088/0004-6256/140/6/1868. arXiv: 1008.0031 [astro-ph.IM].

York, Donald G. et al. (2000). "The Sloan Digital Sky Survey: Technical Summary". *AJ* 120, 1579–1587. DOI: 10.1086/301513. arXiv: astro-ph/0006396 [astro-ph].

You, Yang, Igor Gitman, and Boris Ginsburg (2017). "Large batch training of convolutional networks". *arXiv preprint arXiv:1708.03888*.

Yusifov, I. (2004). "Pulsars and the Warp of the Galaxy". In: *The Magnetized Interstellar Medium*. Ed. by B. Uyaniker, W. Reich, and R. Wielebinski, pp. 165–169. arXiv: astro-ph/0405517 [astro-ph].

Zamora, O. et al. (2015). "New H-band Stellar Spectral Libraries for the SDSS-III/APOGEE Survey". *AJ* 149, 181. DOI: 10.1088/0004-6256/149/6/181. arXiv: 1502.05237 [astro-ph.SR].

Zasowski, G. et al. (2017). "Target Selection for the SDSS-IV APOGEE-2 Survey". *AJ* 154, 198. DOI: 10.3847/1538-3881/aa8df9. arXiv: 1708.00155 [astro-ph.GA].

Zevin, M. et al. (2017). "Gravity Spy: integrating advanced LIGO detector characterization, machine learning, and citizen science". *Classical and Quantum Gravity* 34, 064003. DOI: 10.1088/1361-6382/aa5cea. arXiv: 1611.04596 [gr-qc].

Zhang, Lan et al. (2013). "The Gravitational Potential near the Sun from SEGUE K-dwarf Kinematics". *ApJ* 772, 108. DOI: 10.1088/0004-637X/772/2/108. arXiv: 1209.0256 [astro-ph.GA].

Zhang, Z. et al. (2022). "The Substructures in the Anticenter Region of the Milky Way". *ApJ* 933, 151. DOI: 10.3847/1538-4357/ac7231.

Appendices

Appendix A

Velocity dispersion as a function of vertical height in different Galactocentric radius bins

As stated in Section 3.3, we use a linear function to represent the trend in velocity dispersions and use the results to calculate surface density at different Galactocentric radius bin. Here, we present detailed figures of σ_Z and σ_{RZ} and our fitting results. Figure A.1 shows these for the thin disk population, and Figure A.2 shows these for the thick disk population.

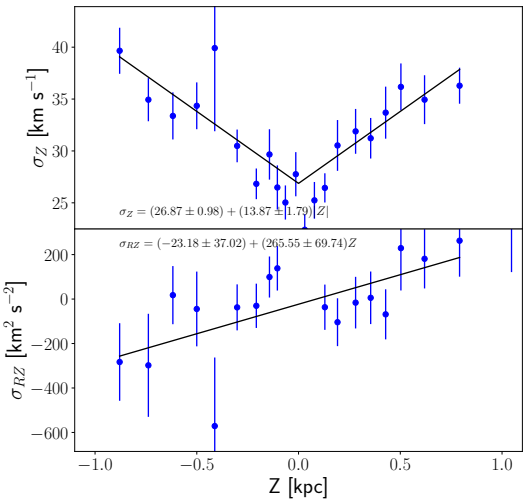

(a) $4 < R < 5$ kpc

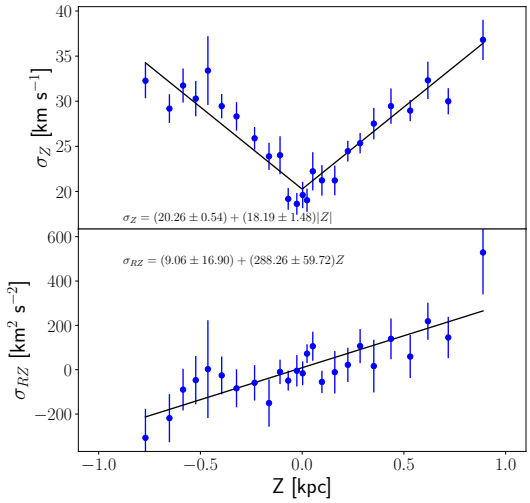

(b) $5 < R < 6$ kpc

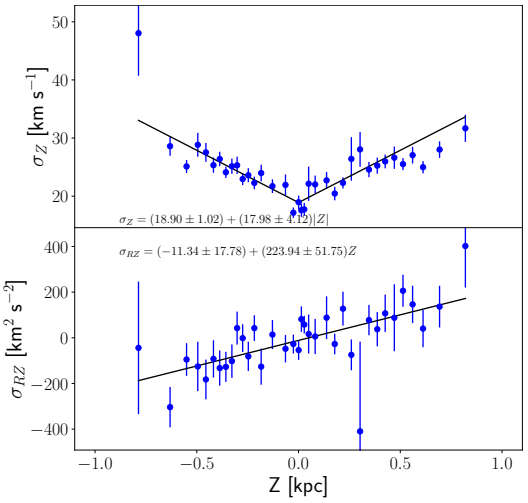

(c) $6 < R < 7$ kpc

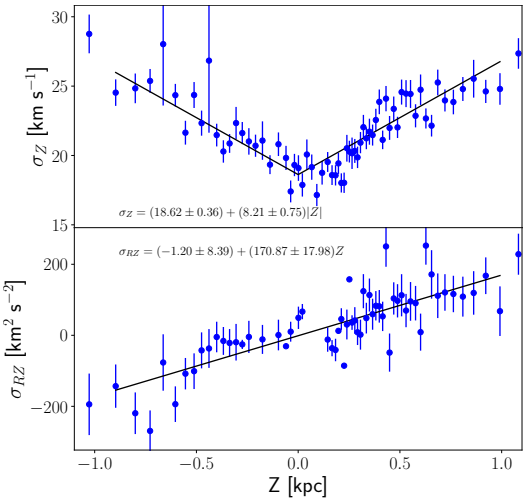

(d) $7 < R < 8$ kpc

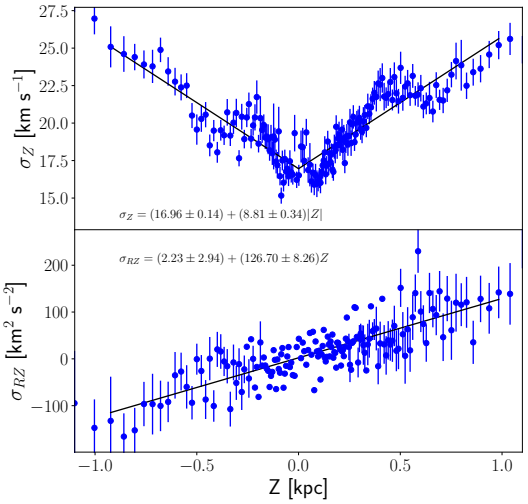

(e) $8 < R < 9$ kpc

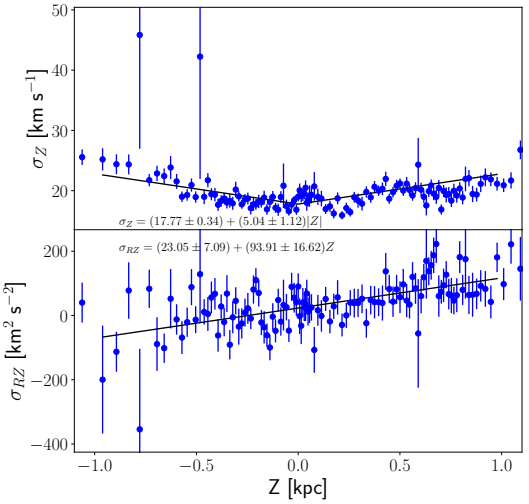

(f) $9 < R < 10$ kpc

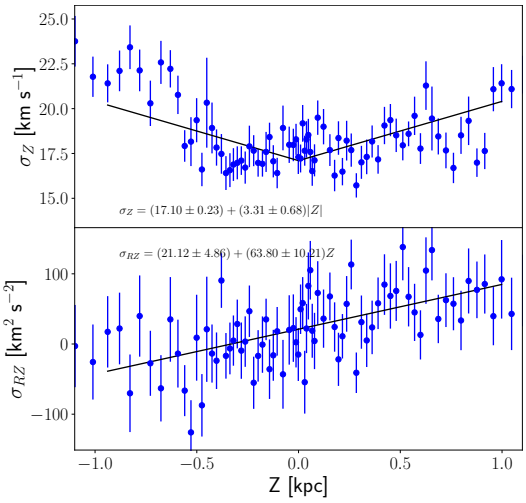

(g) $10 < R < 11$ kpc

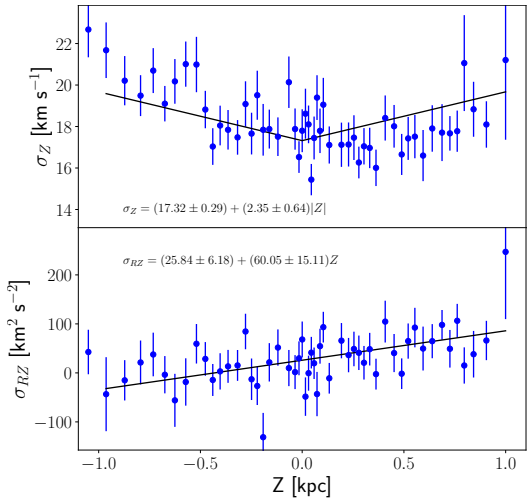

(h) $11 < R < 12$ kpc

Figure A.1: Vertical and RZcross-term velocity dispersion as a function of vertical height for different Galactocentric radii for thin disk.

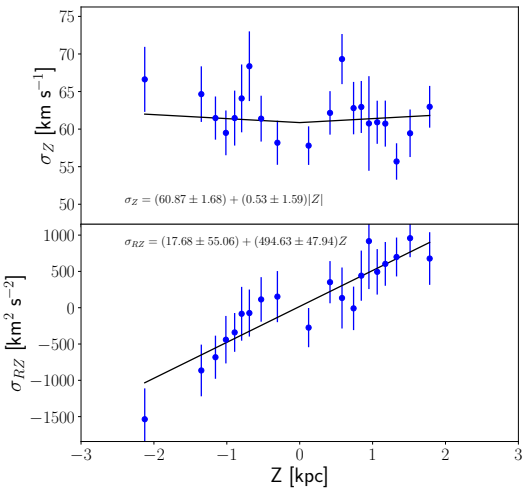

(a) $4 < R < 5$ kpc

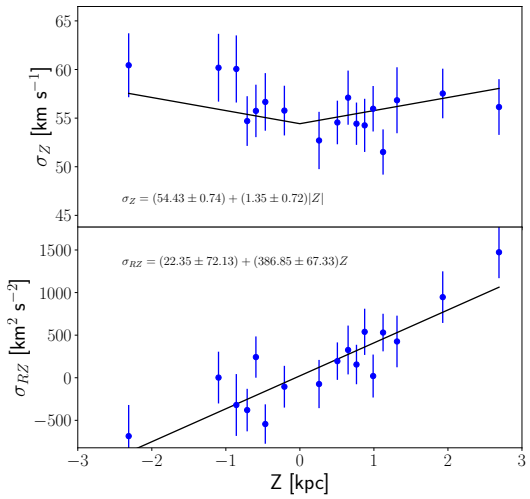

(b) $5 < R < 6$ kpc

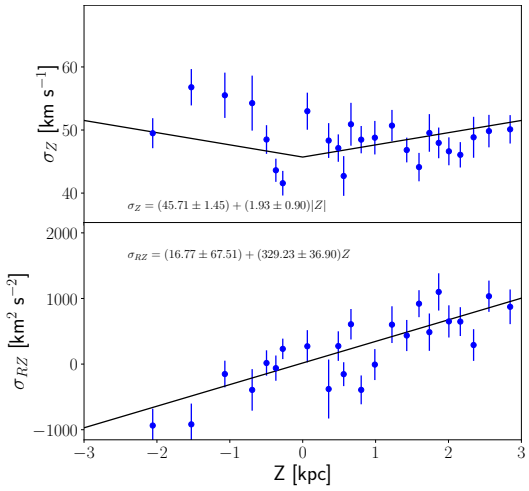

(c) $6 < R < 7$ kpc

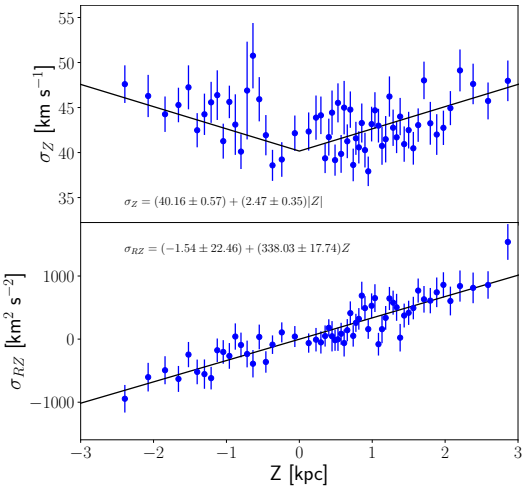

(d) $7 < R < 8$ kpc

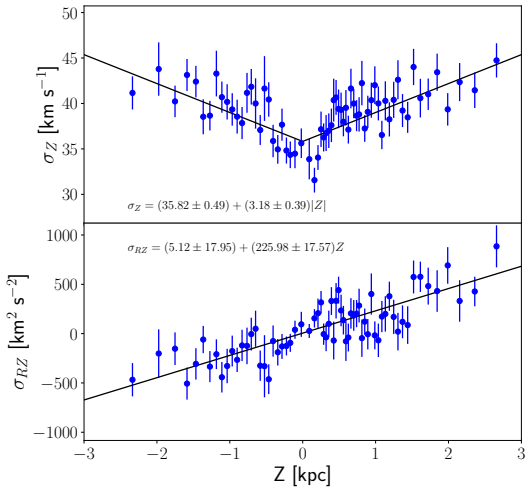

(e) $8 < R < 9$ kpc

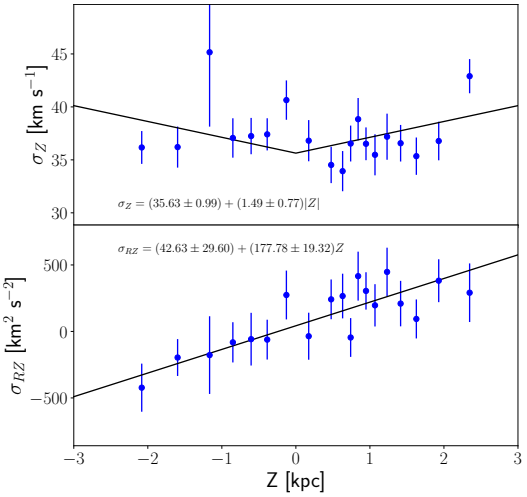

(f) $9 < R < 10$ kpc

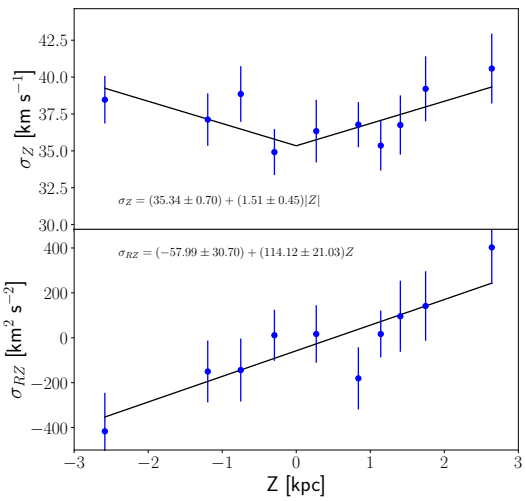

(g) $10 < R < 11$ kpc

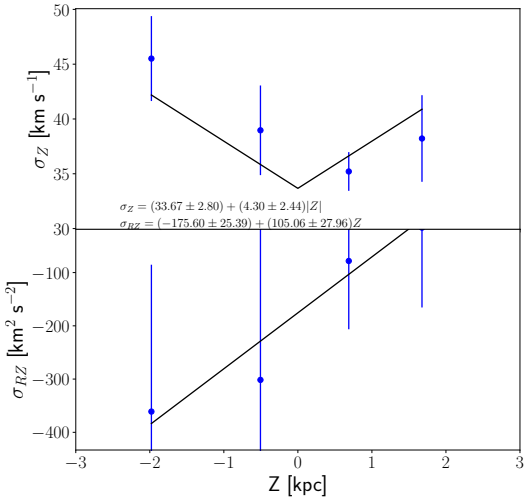

(h) $11 < R < 12$ kpc

Figure A.2: Vertical and cross-term velocity dispersion as a function of vertical height for different Galactocentric radius for the thick disk.

Appendix B

Midplane-Continuous Velocity Dispersion Profiles

Because linear fitting to the observed velocity dispersions introduces a discontinuity at $Z = 0$ (Section 3.5.2), at the suggestion of the anonymous referee to our submitted journal article we attempted several other functional forms. The quadratic function, $\sigma_Z^2(Z) = kZ^2 + \sigma_0^2$, is not a particularly good analytical form to describe the global trend of velocity dispersion (Figure B.1). Nevertheless, we calculated the surface density (adopting a sech^2 population density law), but once again find large discrepancies between the thin and thick disk results (Figure B.3), and with neither agreeing with the SHM, even at large radius, where convergence has been previously observed (Section 3.4.2).

We also tried the $\sigma_Z(Z) = kz \tanh(z/L) + \sigma_0$, which guarantees both contintuity at $Z = 0$ as well as a linear increase in dispersion at large vertical height. The global trend of velocity dispersion is well described by this function form (Figure B.2), but once again we find (Figure B.3) discrepancies between the thin and thick disk calculated surface densities, and disagreement with the well established and tested SHM model.

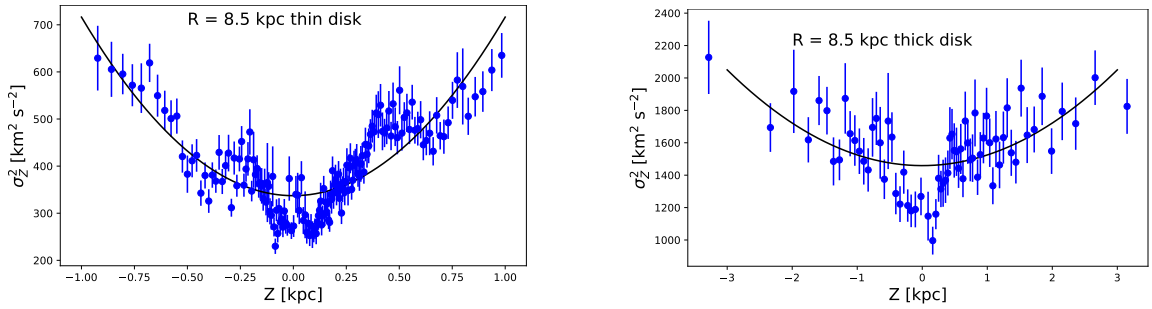

Figure B.1: Quadratic fitting of the velocity dispersion for the thin and thick disk populations for stars in the Galactocentric radius range of $8 < R < 9$ kpc.

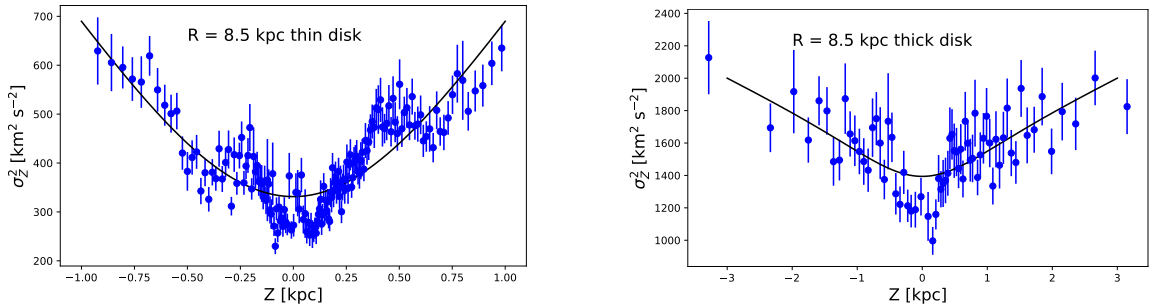

Figure B.2: The tanh fit to the velocity dispersions for the thin and thick disk populations for stars in the Galactocentric radius range of $8 < R < 9$ kpc.

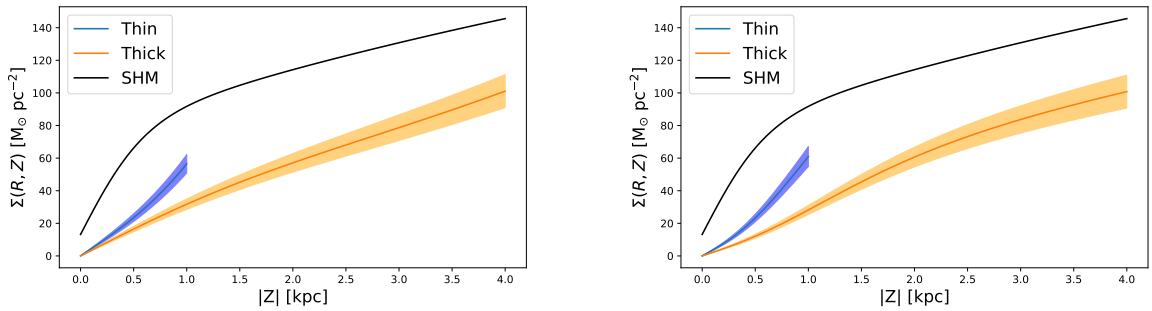

Figure B.3: Calculated surface densities obtained by using the (a) quadratic and (b) tanh velocity dispersion profiles (Figs. B.1 and B.2, respectively).